

Electronic Properties of Self-Organized Quantum Dots

von

Diplom-Physiker

Andrei Schliwa

aus Leipzig

der Fakultät II – Mathematik und Naturwissenschaften
der Technischen Universität Berlin
zur Erlangung des akademischen Grades
Doktor der Naturwissenschaften
– Dr. rer. nat. –

genehmigte Dissertation

Promotionsausschuss:

Vorsitzender:

Prof. Dr. E. Schöll, PhD

Berichter / Gutachter:

Prof. Dr. D. Bimberg

Berichter / Gutachter:

Prof. Dr. M. Grundmann

Tag der wissenschaftlichen Aussprache: 25.4.2007

Berlin 2007

D 83

Zusammenfassung

Die elektronischen und optischen Eigenschaften von verspannten und unverspannten Halbleiterquantenpunkten realistischer Geometrie und chemischer Zusammensetzung werden theoretisch untersucht, d. h. des um Verspannungseffekte erweiterten 8-band- $\mathbf{k} \cdot \mathbf{p}$ -Modells unter Einbeziehung piezoelektrischer Effekte erster und zweiter Ordnung berechnet. Basierend auf den so erhaltenen Einteilchenzuständen werden mittels der Konfigurations-Wechselwirkungs-Methode die Energien von Mehrteilchenzuständen, wie dem Exziton, Biexziton und positiv, wie negativ geladenen Trion ermittelt und mit experimentellen Ergebnissen verglichen.

Im Hauptteil der Arbeit wird eine breite Palette von verschiedenartigen InGaAs/GaAs Quantenpunkten untersucht, die sich in Geometrie und der Art ihrer chemischen Komposition unterscheiden. Die sich ergebenden spektroskopischen Signaturen können somit dazu dienen - ohne aufwändige strukturelle Untersuchungen anzustellen - aus optischen Daten, wie Übergangsenergien oder/und Mehrteilchenbindungsenergien, Schlüsse über die Struktur der involvierten Quantenpunkte zu ziehen. Besonderer Wert wurde bei den Untersuchungen darauf gelegt, wie sich die inhomogene Verspannung mittels der QP-Geometrie auf die elektronischen Zustände auswirkt. Eine Schlüsselrolle spielt dabei die Piezoelektrizität. Erstmals wurde im Detail untersucht, wie sich erste und zweite Ordnung in Abhängigkeit von QP-Form und Komposition verhalten und wie sich die Symmetrie des Einschlusspotentials ändert.

Piezoelektrische Effekte und Verspannung spielen ebenfalls eine große Rolle bei Stapeln von Quantenpunkten. In dieser Arbeit wurden Paare identischer und solche unterschiedlicher Größe in Hinsicht auf das Kopplungsverhalten von Elektron- und Lochzuständen untersucht. Im ersten Fall identischer Quantenpunkte führt die inhomogene Verspannung zur Einführung einer vertikalen *Confinement*-Asymmetrie. Diese führt dazu, dass der Lochgrundzustand immer im unteren QP gebunden ist, egal, ob es sich um einen Zweifach-, Dreifach-, oder Fünffachstapel handelt. Piezoelektrische Effekte können diesen Trend im Einzelfall noch verstärken. Im Fall von Paaren unterschiedlich großer QPte, ist erstmals das Kopplungsverhalten von Elektronenniveaus unterschiedlicher Schalen untersucht worden. Mittels vertikal angelegter elektrischer Felder wurde die Resonanzbedingung variiert: Nur solche Einzel-QP-Zustände bilden gekoppelte Hybridzustände, die zur selben Irreduziblen Darstellung der entsprechenden Symmetriegruppe gehören.

Das Stapeln von Quantenpunkten wird auch im Zusammenhang mit dem Design von Halbleiterverstärkern und speziell ihrer Polarisationsunabhängigkeit benutzt. Die dabei zum Tragen kommenden physikalischen Mechanismen wurden aufgeklärt, und die sich mit der Stapelung ändernde Biaxialverspannung als Schlüsselement identifiziert. Damit einher geht eine Änderung des Schwerloch/Leichtlochverhältnisses der Lochzustände, welche schlussendlich in eine Umkehrung der Absorption der TE -Mode im Verhältnis zur TM-Mode mündet.

InAs Quantenpunkte, gewachsen auf InP anstatt auf GaAs, zeigen bei gleicher Geometrie eine ins Rote verschobenen Lumineszenz. Ursache dieses Verhaltens ist der vergleichsweise kleinere Unterschied in der Gitterkonstante und die daraus resultierende vermindernde Verspannung. In dieser Arbeit wurden, angelehnt an experimentellen Arbeiten, flache kegelförmige Quantenpunkte in Abhängigkeit ihrer Höhe untersucht. Dabei wurde auch die Substratorientierung zwischen (100) und (311) variiert. Für den letzteren Fall führt das piezoelektrische Feld zur Aufhebung jeglicher Symmetrie des Einschlusspotentials und somit zur deutlichen Aktivierung vormals nahezu verbotener Übergänge.

Im Rahmen dieser Arbeit wurde der Hamiltonoperator um die Möglichkeit erweitert, Magnetfelder beliebiger Ausrichtung zu berücksichtigen. Anhand von invertierten GaAs/AlGaAs QPten, wurden ausgiebige Testrechnungen durchgeführt, in denen zudem auch die Interfacerauhigkeit variiert wurde. Die Ergebnisse wurden mit Hochfeldmagnetmessungen verglichen und exzellente Übereinstimmung festgestellt.

Parts of this work have been published in

- (1) *Control of fine-structure splitting and excitonic binding energies in selected individual InAs/GaAs quantum dots.*
R. Seguin, A. Schliwa, T.D. Germann, S. Rodt, K. Pötschke, A. Strittmatter, U.W. Pohl, M. Winkelkemper, T. Hammerschmidt, P. Kratzer, D. Bimberg.
Appl. Phys. Lett. **89**, 263109 (2006).
- (2) *Electronic and optical properties of InAs/InP quantum dots on InP(100) and InP(311)B substrates: Theory and experiment*
C. Cornet, A. Schliwa, J. Even, F. Dore, C. Celebi, A. Letoublon, E. Mace, C. Paranthoen, A. Simon, P.M. Koenraad, N. Bertru, D. Bimberg, S. Loualiche.
Phys. Rev. B **74**, 035312 (2006).
- (3) *Evolution of a multimodal distribution of self-organized InAs/GaAs quantum dots.*
U.W. Pohl, K. Pötschke, A. Schliwa, F. Guffarth, D. Bimberg, N.D. Zakharov, P. Werner, M.B. Lifshits, V.A. Shchukin, D.E. Jesson.
Phys. Rev. B **72**, 245332 (2005).
- (4) *Correlation of structural and few-particle properties of self-organized InAs/GaAs quantum dots.*
S. Rodt, A. Schliwa, K. Pötschke, F. Guffarth, D. Bimberg.
Phys. Rev. B **71**, 155325 (2005).
- (5) *Size-dependent fine-structure splitting in self-organized InAs/GaAs quantum dots.*
R. Seguin, A. Schliwa, S. Rodt, K. Pötschke, U.W. Pohl, D. Bimberg.
Phys. Rev. Lett. **95**, 257402 (2005).
- (6) *Correlation of structural and optical properties of self-organized quantum dots.*
A. Schliwa, S. Rodt, F. Guffarth, K. Pötschke, T. Warming, R. Seguin, D. Bimberg.
In Proceedings of the SPIE-Conference on Quantum Dots, Nanoparticles, and Nanoclusters (26.1.-27.1.2004, San Jose, CA, USA), published in
Proc. SPIE Int. Soc. Opt. Eng. **5361**, 35 (2004).
- (7) *Hierarchical self-assembly of GaAs/AlGaAs quantum dots.*
A. Rastelli, S. Stufler, A. Schliwa, R. Songmuang, C. Manzano, G. Costantini, K. Kern, A. Zrenner, D. Bimberg, O.G. Schmidt.
Phys. Rev. Lett. **92**, 166104 (2004).
- (8) *Many-particle effects in self-organized quantum dots.*
F. Guffarth, S. Rodt, A. Schliwa, K. Pötschke , D. Bimberg.
In Proceedings of the Thirteenth International Winterschool on New Developments in Solid State Physics: Low-Dimensional Systems (15.2.-20.2.2004, Mauterndorf, Austria), published in Physica E **25**, 261 (2004).
- (9) *Biexcitons in self-organized InAs/GaAs quantum dots: an optical probe for structural properties.*
S. Rodt, R. Heitz, R. L. Sellin, A. Schliwa, K. Pötschke, D. Bimberg.
In Proceedings of the 11th International Conference on Modulated Semiconductor Structures (14.7.-18.7.2003, Nara, Japan), published in Physica E **21**, 1065 (2004).
- (10) *Repulsive exciton-exciton interaction in quantum dots.*
S. Rodt, R. Heitz, A. Schliwa, R. L. Sellin, F. Guffarth, D. Bimberg.
Phys. Rev. B **68**, 35331 (2003).

- (11) *Shape-dependent properties of self-organized quantum dots: Few-particle states and exciton-phonon coupling.*
R. Heitz, S. Rodt, A. Schliwa, D. Bimberg.
In Proceedings of the 2nd International Conference on Semiconductor Quantum Dots
(30.9.-3.10.2002, Tokyo, Japan), published in *Physica Status Solidi B* **238**, 273 (2003).
- (12) *Shape and composition effects on excitons and biexcitons in quantum dots.*
O. Stier, R. Heitz, A. Schliwa, D. Bimberg.
Physica Status Solidi A **190**, 477 (2002).
- (13) *Antibinding biexcitons in self-organized InAs/GaAs quantum dots.*
S. Rodt, R. Heitz, V. Türck, R. L. Sellin, A. Schliwa, O. Stier, D. Bimberg.
In Proceedings of the 26th International Conference on the Physics of Semiconductors
(29.7.-2.8.2002, Edinburgh, UK), published in
Institute of Physics Conference Series **171**, C2.5 (2002).
- (14) *Few-particle effects in self-organized quantum dots.*
S. Rodt, A. Schliwa, R. Heitz, V. Türck, O. Stier, R. L. Sellin, M. Strassburg, U. W. Pohl,
D. Bimberg.
In Festschrift in honour of Roland Zimmermann, published in
Physica Status Solidi B **234**, 354 (2002).
- (15) *Exciton level crossing in coupled InAs/GaAs quantum dot pairs.*
A. Schliwa, O. Stier, R. Heitz, M. Grundmann, D. Bimberg.
Physica Status Solidi B **224**, 405 (2001).

Contents

Part 1. Electronic Structure Calculations	8
Chapter 1. Introduction	9
Chapter 2. Method of calculation	11
2.1. Calculation of strain	11
2.2. Piezoelectricity and the reduction of lateral symmetry	12
2.3. Single Particle States	14
2.4. Many-Particle States	20
2.5. Optical Properties	21
Part 2. InGaAs/GaAs Quantum Dots	23
Chapter 3. Impact of Size, Shape and Composition on Piezoelectric Effects and Single-Particle States	24
3.1. The Investigated structures: Variation of size, shape and composition	24
3.2. The Impact of the piezoelectric field	26
3.3. The vertical and lateral aspect ratio	34
3.4. Varying composition profiles	36
3.5. Conclusions	38
Chapter 4. Few-particle Energies versus Geometry and Composition	40
4.1. Interrelation of QD-structure, strain and piezoelectricity, and Coulomb interaction	40
4.2. The Impact of QD size (series A and H)	42
4.3. The aspect ratio	46
4.4. Different composition profiles	48
4.5. Correlation vs. QD size, shape and particle type	49
4.6. Conclusions	51
Chapter 5. Multimodal QD-size distribution: Theory and Experiment	52
5.1. Sample growth	53
5.2. Determination of QD-morphology and the spectrum of excited states	53
5.3. Predicted absorption spectra of truncated pyramidal InAs/GaAs QDs	56
5.4. Single-dot spectra obtained from cathodoluminescence spectroscopy	57
5.5. Results and Interpretation	58
5.6. Conclusion	60
Chapter 6. Stacked quantum dots	61
6.1. Energetics of QD stacks	61
6.2. Role of strain and piezoelectricity	62
6.3. Strength of electronic coupling in pairs of identical QDs	65
6.4. Small perturbations of the size homogeneity	70
6.5. Asymmetric QD molecules: Coupling of different electronic shells	71
6.6. Tailoring the TE-TM ratio in semiconductor optical amplifiers	73
6.7. Conclusions	81

Part 3. Other Material Systems	83
Chapter 7. Electronic and optical properties of InAs/InP quantum dots on InP(100) and InP(311)B substrates	84
7.1. Choice of model QDs	84
7.2. Absorption spectra for InAs/InP QDs	86
7.3. Impact of substrate orientation on the QDs optical properties	89
7.4. Conclusions	94
Chapter 8. Inverted GaAs/Al _x Ga _{1-x} As Quantum Dots	96
8.1. Choice of the model QDs	96
8.2. Influence of interface intermixing on the optical properties	97
8.3. External magnetic fields	102
8.4. Discussion	106
8.5. Summary and Conclusions	108
Summary and Outlook	109
Outlook	110
Acknowledgements	112
Bibliography	113

Part 1

Electronic Structure Calculations

CHAPTER 1

Introduction

Semiconductor quantum dots (QD) are fascinating physical subjects exhibiting electronic properties close to hydrogen in a dielectric cage, thus merging semiconductor with atomic physics. Their electronic properties,[1–3] exciton and biexciton binding energies, exciton fine-structure splitting [4] are strongly geometry dependent. Varying size, shape and composition are attractive and practical means to control the electronic and optical properties. Many applications are based on this discovery.[5–7]

Despite the tremendous advances in structural characterization techniques the real shape and composition of capped quantum dots (QD), which present the decisive input parameters for all modeling,[2, 3, 8] are often only poorly known. Even the most sophisticated STM techniques either provide only cross sections of capped [9] or surface images of uncapped [10] QDs despite their atomic resolution. Therefore the purpose of this work is to identify those spectroscopic quantities that serve as a fingerprint for a specific QD structure, thus, addressing the inverse problem of fitting the spectroscopic data to the model and deriving the size, shape and composition as adjustable parameters. Eight band $\mathbf{k} \cdot \mathbf{p}$ theory enables us to obtain the electronic structure thus taking into account arbitrary QD-shapes, as well as strain, piezoelectricity, and band mixing effects.[3] The model provides, at reasonable computational cost, a fast and transparent relation between the electronic structure of QDs and bulk properties of the constituent materials.

We present here systematic calculations of the single- and few-particle properties of many types of QDs, varying size, shape (square/circular/rhomboïd base, different vertical/lateral aspect ratios) and composition (homogeneous/peaked and isotropic interdiffusion). Despite strain, first *and* second order piezoelectric effects are taken into account.[11]

Most of the recent work has been focused on single QDs. However, QD structures for applications are usually prepared as multi-layer, vertically stacked systems, since they have some advantageous properties such as a better homogeneity [6] and higher active volume. Therefore, one chapter of this work is dedicated to the study of vertically stacked QDs. Their actual and potential applications are numerous, ranging from the mere increase of active media volume, [12] over the creation of entangled photon pairs,[13] for quantum information processing,[14] the tailoring of the TE/TM mode intensity ratio [15] of QD based semiconductur optical amplifiers,[16–18] to the quantum dot cascade laser.[19, 20] The stacking of QDs can lead to the coupling of electronic states with the formation of binding and anti-binding states. The main parameters, that determine the onset of electronic coupling, are the inter-QD distance, the relative QD size, the symmetry of the overlapping single QD wavefunctions, and strain and piezoelectricity. To quantify the impact of these parameters, pairs of structurally *identical* and *nonidentical* QDs with varying spacer thickness and QD-shape are considered. Furthermore, external electric fields are applied to tune the resonance energies of the adjacent QDs.

One of the biggest challenges for QD-laser-devices is to reach the $1.55\text{ }\mu\text{m}$ (0.8 eV) wavelength used for long-haul telecommunications. In the past the large efforts to push the InGaAs/GaAs system to this wavelength have been hampered by the large strain that accumulates in- and outside the QD-structure during the Stranski-Krastanow growth leading to a large increase of the local InAs band gap. Therefore, the most recent developments aimed at the reduction of strain in the system which can be achieved by introducing metamorphic buffers [21] and thus replacing GaAs by InGaAs as matrix material close to the QD, or by turning to InP as a completely different host material which is employed in this case. Both approaches reduce the lattice mismatch and limit the strain in the QD-system.[22] The smaller lattice mismatch, however, carries the danger of creating too large QDs during the epitaxy resulting in a small QD density and insufficient gain.

This can be circumvented by using the (311)*B* substrate orientation,[23–25] resulting in high QDs densities and low size dispersion permitting the development of low-thresholds QD lasers.[26]

In this work we theoretically investigate the impact of substrate orientation on the QDs optical properties, using the eight-band $\mathbf{k}\cdot\mathbf{p}$ model including strain and piezoelectric effects, and demonstrate that the use of the (311)*B* substrate breaks the initial symmetry of the (100) system, thus modifying the optical properties of the QDs.

Recently, unstrained GaAs/Al_{*x*}Ga_{1-*x*}As QDs were fabricated through an ingenious multistep approach based on a combination of hierarchical self-assembly and *in situ* etching.[27] Photoluminescence (PL) of an ensemble of such QDs revealed an appreciably smaller inhomogeneous broadening, in the range between 8 to 15 meV depending on the growth conditions, indicating a good size homogeneity. The QDs have a typical lateral size of \sim 35nm and a thickness of \sim 6nm.

Due to the nonexistence of strain and reduced uncertainties in the size and shape, such QDs represent an ideal test case for electronic structure models. In Ref. [27] an eight-band $\mathbf{k}\cdot\mathbf{p}$ model was successfully applied to describe the zero-field PL and single dot spectra.

We extend the previous theoretical studies based on eight-band $\mathbf{k}\cdot\mathbf{p}$ theory [3] taking into account the Zeeman effect.[28] Single particle states, exciton binding energies and its diamagnetic shift are calculated for magnetic fields applied in growth direction as well as in the direction perpendicular to the growth direction. The calculations are based on a realistic confinement potential which is derived from high resolution STM data taken from Ref. [27]. Furthermore, recent cross section scanning tunneling microscopy (X-STM) experiments demonstrate, that the interfaces between GaAs and AlGaAs layers are not abrupt [29] as previously observed for quantum wells.[30] Since the size and shape of the dots are known, the previously not discussed effect [31, 32] of this roughness on the electronic properties of the dots is investigated in detail.

The overall intention of this work is to link the structural properties of QDs to their electronic and optical properties. Thus, as will be demonstrated in various examples, it becomes possible to derive the true 3D QD-morphology by their spectroscopic signature alone.

CHAPTER 2

Method of calculation

The electronic and optical properties are calculated for self-organized QDs based on a three dimensional implementation of the eight-band $\mathbf{k} \cdot \mathbf{p}$ model for the single-particle states and a configuration interaction scheme for the multi-particle states.[2, 3, 33] The calculations account for the inhomogeneous strain distribution, the first and second order piezoelectric effects,[2, 11] interband mixing and Coulomb interactions. A schematic presentation of the six steps involved is shown in figure 2.1 and works in the following way: (a) The modelling process starts with an assumption on shape, size and composition guided either by structural investigations of a QD-sample or - as in this work - suggested only by peculiarities of the optical spectra. Next, the strain distribution (b) and the piezoelectric potential (first and second order) (c) are calculated, which enter (d) the strain dependent eight-band $\mathbf{k} \cdot \mathbf{p}$ Hamiltonian. By solving the Schrödinger equation we obtain single-particle wave functions. The parameters entering this Hamiltonian are based on experimental values for the required bulk material Γ -point band structure parameters. Free, adjustable parameters are *not* present in this model. (e) The single-particle states provide a basis for the configuration interaction model which is applied to calculate excitonic properties, including correlation and exchange. (f) Finally the optical absorption spectra are computed. In the next sections, the steps (a)-(f) are explained in more detail.

2.1. Calculation of strain

Since the impact of strain on the confinement is comparable to that of the band offsets at the heterojunctions, the wavefunctions and energies are very sensitive to the underlying strain distribution. The impact of the model used for calculating the strain distribution has been analysed in a number of publications.[3, 34]

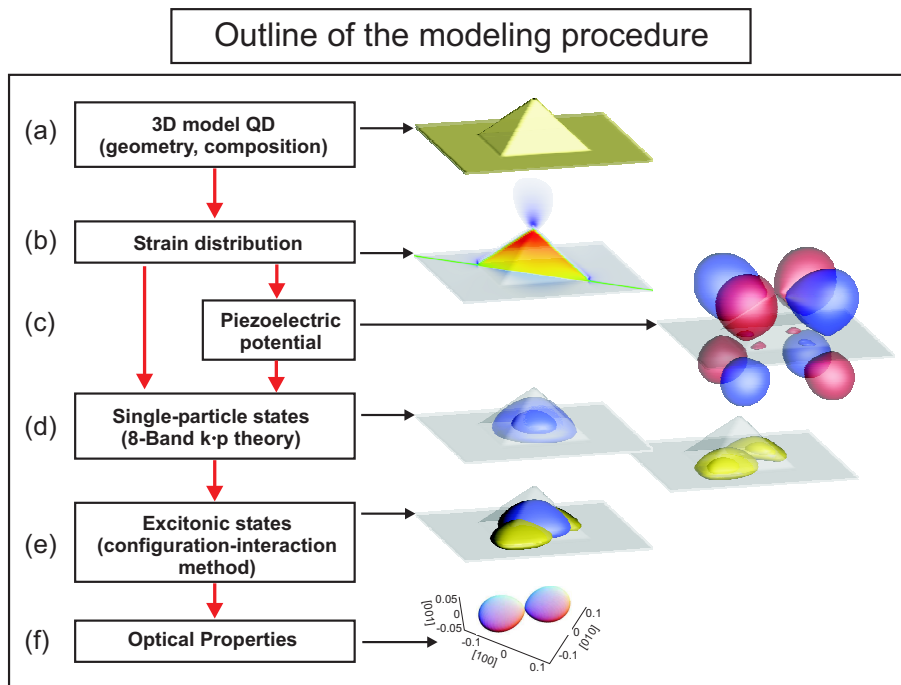


FIGURE 2.1. The steps involved in modelling the electronic and optical QD-properties (see text), shown for a pyramidal InAs/GaAs QD as an example.

Stier *et al.* [3] argue that the continuum elasticity model (CM) gives better results for QDs than the valence force field (VFF) model (Keating) in its linearized version (Kane). The major part of the differences in the strain distribution are attributed to the incorrect value of the elastic constant C_{44} in the VFF model and not to its atomistic character. Later, Zunger *et al.* [35] introduced a generalized version of the VFF model - the G-VFF model - where C_{44} is reproduced correctly. Although the potential of the Keating model in its original version is not harmonic, it has been remarked by Kane,[36] that anharmonic effects due to higher order terms are not satisfactorily treated. Therefore, Klimeck and coworkers extended this model to include anharmonic effects correctly.[37] The same issue was addressed by Hammerschmidt *et al.*[38] and Migliorato *et al.*,[39] who employed the Tersoff-potential method [40].

The choice of the most appropriate strain model depends on the choice of the model for the electronic structure calculations. Since we use - with the eight-band $\mathbf{k} \cdot \mathbf{p}$ model - a continuum approach, an atomistic strain model cannot unfold its full potential for two reasons:

First, the mapping of the atomic positions onto a strain tensor field is associated with a loss of information. To describe the positions of four tetrahedrally coordinated In atoms around an As atom five times the three spatial dimensions = 15 parameters are required. The strain tensor field, on the other hand, is described by only six independent components at each local position.

Second, the $\mathbf{k} \cdot \mathbf{p}$ model provides only a limited number of parameters to account for strain, hence, the model is not sensitive to the complete information an atomistic model provides. For example, the strain tensor, derived from the CM model, for a QD having a fourfold rotational C_{4v} symmetry has C_{4v} symmetry too, in contrast to atomistic models: The tetrahedral configuration of the atoms [34] leads to C_{2v} symmetry, i.e. the strain components are different along the $[110]$ and $[1\bar{1}0]$ directions. The resulting electron p -splitting, obtained by putting the atomistic model derived strain tensor field into our $\mathbf{k} \cdot \mathbf{p}$ model, is underestimated. The structural $C_{\infty v}$ or C_{4v} symmetry is noticeably broken only in the second step by the inclusion of the piezoelectric field.

For all these reasons the continuum elastic model is the optimal choice for the current implementation of the eight-band $\mathbf{k} \cdot \mathbf{p}$ model. The total strain energy of the CM model is given by [3]:

$$U_{cm} = \frac{1}{2} \sum_{i,j,k,l} C_{ijkl} \epsilon_{ij} \epsilon_{kl} \quad .$$

U is minimized for a given structure, using finite differences for the strains $\epsilon_{ij} = \partial u_i / \partial x_j$, where \mathbf{u} is the displacement vector field. The compliances C_{ijkl} are represented by the parameters C_{11} , C_{12} and C_{44} for cubic crystals. Results for the strain distribution in capped InAs pyramids are shown by Grundmann *et al.* in Ref. [2] and depicted in Fig. 2.2.

2.2. Piezoelectricity and the reduction of lateral symmetry

Piezoelectricity is defined as the generation of electric polarization by application of stress to a crystal lacking a center of symmetry.[41] The zinc-blende structure is one of the simplest examples of such a lattice and the strength of the resulting polarization is described by one parameter alone, e_{14} , for the linear case, resulting in a polarization \mathbf{P}_1 , and three parameters, B_{114} , B_{124} , and B_{156} for the quadratic case,[11]

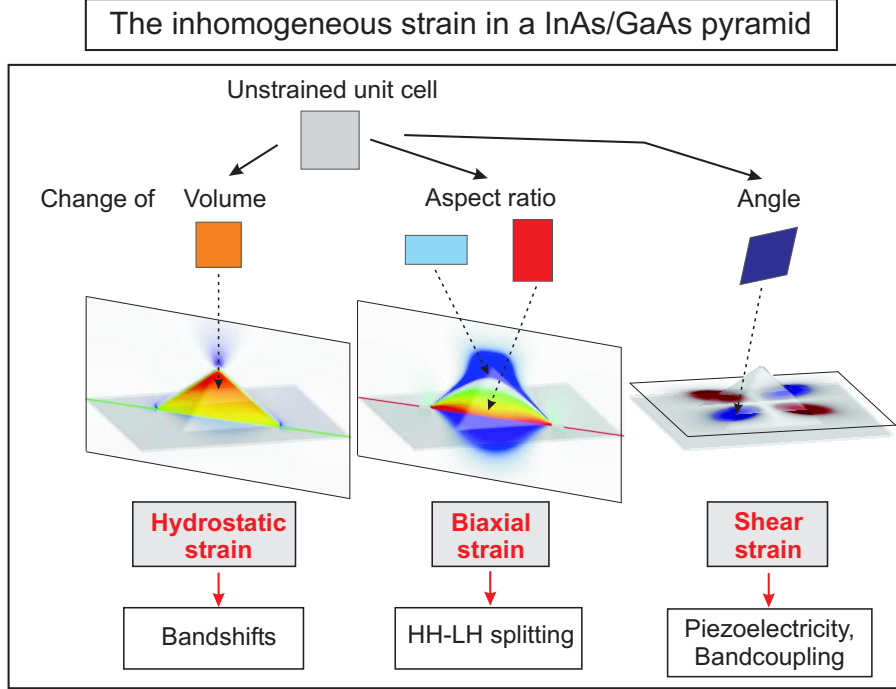


FIGURE 2.2. Different types of strain shown as vertical or horizontal scans through a pyramidal InAs/GaAs quantum dot. The hydrostatic strain, $\epsilon_H = \epsilon_{xx} + \epsilon_{yy} + \epsilon_{zz}$, shifts the local conduction and valence bands. The biaxial strain, $\epsilon_B = \epsilon_{xx} + \epsilon_{yy} - 2\epsilon_{zz}$, splits the local HH and LH band edges. The shear strain components are responsible for piezoelectricity and band coupling.

resulting in a polarization \mathbf{P}_2 . Their relation to the strain tensor field is given by:

$$\begin{aligned}
 \mathbf{P}_1 &= 2e_{14} \begin{pmatrix} \epsilon_{yz} \\ \epsilon_{xz} \\ \epsilon_{xy} \end{pmatrix}, \\
 \mathbf{P}_2 &= 2B_{114} \begin{pmatrix} \epsilon_{xx}\epsilon_{yz} \\ \epsilon_{yy}\epsilon_{xz} \\ \epsilon_{zz}\epsilon_{xy} \end{pmatrix} + \\
 &+ 2B_{124} \begin{pmatrix} \epsilon_{yz}(\epsilon_{yy} + \epsilon_{zz}) \\ \epsilon_{xz}(\epsilon_{zz} + \epsilon_{xx}) \\ \epsilon_{xy}(\epsilon_{xx} + \epsilon_{yy}) \end{pmatrix} + \\
 &+ 4B_{156} \begin{pmatrix} \epsilon_{xz}\epsilon_{xy} \\ \epsilon_{yz}\epsilon_{xy} \\ \epsilon_{yz}\epsilon_{xz} \end{pmatrix}.
 \end{aligned} \tag{2.1}$$

Piezoelectric charges, ρ_{piezo} , arise from the polarizations:

$$\begin{aligned}
 \rho_{\text{piezo}}(\mathbf{r}) &= -\nabla \cdot \mathbf{P} , \\
 \mathbf{P} &= \mathbf{P}_1 + \mathbf{P}_2 .
 \end{aligned}$$

The resulting piezoelectric potential is obtained by solving Poisson's equation taking into account the material dependent static dielectric constants, $\epsilon_s(\mathbf{r})$

$$(2.2) \quad \rho_p(\mathbf{r}) = \epsilon_0 \nabla \cdot [\epsilon_s(\mathbf{r}) \nabla V_p(\mathbf{r})],$$

$$\Leftrightarrow$$

$$(2.3) \quad \Delta V_p(\mathbf{r}) = \frac{\rho_p(\mathbf{r})}{\epsilon_0 \epsilon_s(\mathbf{r})} - \frac{1}{\epsilon_s(\mathbf{r})} \nabla V_p(\mathbf{r}) \cdot \nabla \epsilon_s(\mathbf{r}).$$

The first term on the right hand side of Eq. 4.2 refers to the true three-dimensional charge density while the second is the contribution of polarization interface charge densities due to a discontinuous $\epsilon_s(\mathbf{r})$ across heterointerfaces. The way, the shear strain component ϵ_{xy} creates a charge dipol leading to \mathbf{P}_1 is schematically shown in Fig. 2.3.

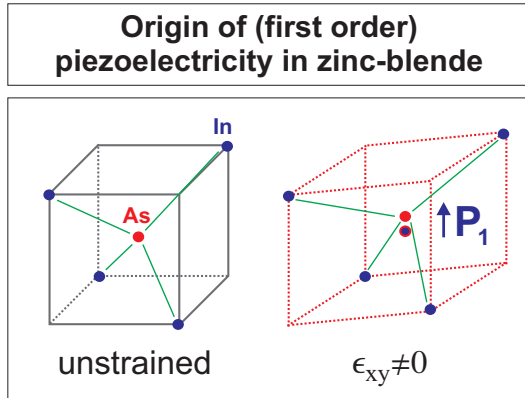


FIGURE 2.3. The deformation of a zinc-blende unit cell (here only one eighth of the full one is shown), is described by one non-zero shear strain component ϵ_{xy} only. The blue bullet in the right picture designates the barycenter of the In-atoms, the red bullet is the As-atom. Due to the deformation, they are not degenerate anymore, and create a (piezoelectric) dipol-charge. According to Eq.2.1, this leads to a polarization $\mathbf{P}_1 = 2 e_{14}(0, 0, \epsilon_{xy})$, which is aligned along the vertical z-direction.

The importance of the second order term, \mathbf{P}_2 , for InGaAs/GaAs(111) quantum wells (QWs) and QDs has been pointed out recently by Bester and coworkers.[11, 42] They found that in QWs the linear and quadratic contributions have opposite effects on the field, and for large strain the quadratic term even dominates. For InAs/GaAs QDs, however, the situation is more complex. In addition to the large strain their three-dimensional structure comes into play: The linear term generates a quadrupole-like potential, which reduces a structural C_{4v} - or $C_{\infty v}$ -symmetry of a QD to C_{2v} .[2, 43] The effect of the quadratic term has been evaluated recently by Bester *et al.*[42] for lens-shaped QDs. It was found to cancel the first order potential inside the QD, leading to a field free QD. This investigation will be extended to a variety of more realistic structures in chapter 3.1). For a pyramidal QD with a base length of 17 nm and $\{101\}$ side facets the strength and distribution of the piezoelectric potential resulting from the two orders of the piezoelectric tensor is shown in Fig. 2.4. Apart from the different orientation and sign of the two contributions, an important peculiarity of the second order potential is its restriction to the interior of the QD, which is in apparent contrast to the widespread first-order field. This difference is linked to the origin of the polarization \mathbf{P} : \mathbf{P}_1 is a function of the shear-strain components alone, whereas \mathbf{P}_2 results mainly from the product of the diagonal and the shear-strain. However, in contrast to the shear-strain components, the diagonal elements ϵ_{ii} are large only inside the QD and its close vicinity. Therefore, \mathbf{P}_2 -charges can only be created in this region.

2.3. Single Particle States

2.3.1. The eight-band $\mathbf{k} \cdot \mathbf{p}$ model. The energy levels and wavefunctions of bound electron and hole states are calculated using the eight-band $\mathbf{k} \cdot \mathbf{p}$ model. It was originally developed for the description of

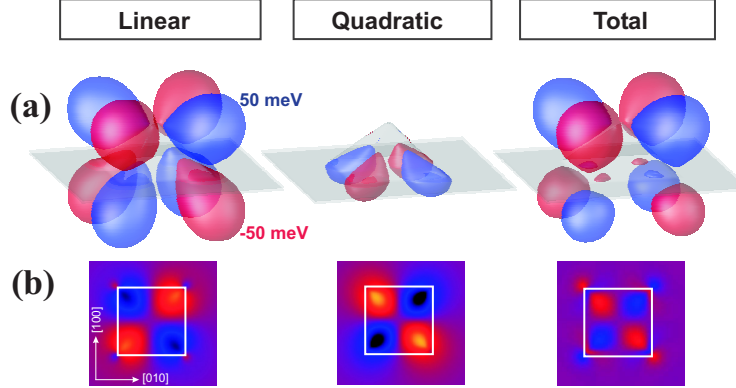


FIGURE 2.4. (a) The piezoelectric potential isosurfaces at ± 50 meV of a pyramidal InAs quantum dot with 17 nm base length shown for the linear, the quadratic part and for sum of both. (b) Contour plots of the piezoelectric potential 2 nm above the wetting layer.

TABLE 1. Linear and quadratic piezoelectric coefficients (C/m^2) taken from Bester *et al.*[11] Symmetry considerations for the zincblende crystal structure imply that there are only 24 non-zero elements of the $B_{\mu j k}$ tensor, which can be reduced to three independent elements, B_{114} , B_{124} , and B_{156} .

	e_{14}	B_{114}	B_{124}	B_{156}	$e_{14}(\text{exp})$
InAs	-0.115	-0.531	-4.076	-0.120	-0.045
GaAs	-0.230	-0.439	-3.765	-0.492	-0.16

electronic states in bulk material.[44–47] For the use in heterostructures, the envelope function version of the model has been applied to quantum wells,[48] quantum wires, [8] and quantum dots.[3, 49–51] Details of the principles of our implementation are outlined in Ref.[8, 33].

Following Gershoni *et al.*, the Hamiltonian is expanded into the basis

$$(2.4) \quad (|S \uparrow\rangle, |X \uparrow\rangle, |Y \uparrow\rangle, |Z \uparrow\rangle, |S \downarrow\rangle, |X \downarrow\rangle, |Y \downarrow\rangle, |Z \downarrow\rangle)^T ,$$

and takes the block matrix form

$$(2.5) \quad \hat{H} = \begin{pmatrix} G(\mathbf{k}) & \Gamma \\ -\overline{\Gamma} & \overline{G}(\mathbf{k}) \end{pmatrix} .$$

$G(\mathbf{k})$ and Γ are both 4×4 -matrices and the overline denotes the complex conjugate. The matrix G is composed from a potential energy part G_1 , a kinetic energy part G_2 , a spin-orbit interaction part G_{SO} , and a strain dependent [44, 48, 52] part G_{st} :

$$(2.6) \quad G = G_1 + G_2 + G_{SO} + G_{st} .$$

with

$$(2.7) \quad G_1 = \begin{pmatrix} E_c & iPk_x & iPk_y & iPk_z \\ -iPk_x & E'_v & 0 & 0 \\ -iPk_y & 0 & E'_v & 0 \\ -iPk_z & 0 & 0 & E'_v \end{pmatrix} ,$$

$$(2.8) \quad G_2 = \begin{pmatrix} A'\mathbf{k}^2 & Bk_yk_z & Bk_xk_z & Bk_xk_y \\ Bk_yk_z & L'k_x^2 + M(k_y^2 + k_z^2) & N'k_xk_y & N'k_xk_z \\ Bk_xk_z & N'k_yk_x & L'k_y^2 + M(k_x^2 + k_z^2) & N'k_yk_z \\ Bk_xk_y & N'k_xk_z & N'k_yk_z & L'k_z^2 + M(k_x^2 + k_y^2) \end{pmatrix} .$$

$$(2.9) \quad G_{\text{st}} = \begin{pmatrix} a_c(\epsilon_{xx} + \epsilon_{yy} + \epsilon_{zz}) & b'\epsilon_{yz} - iP\epsilon_{xj}k^j & b'\epsilon_{zx} - iP\epsilon_{yj}k^j & b'\epsilon_{xy} - iP\epsilon_{zj}k^j \\ b'\epsilon_{yz} + iP\epsilon_{xj}k^j & \left\{ \begin{array}{l} l\epsilon_{xx} + \\ m(\epsilon_{yy} + \epsilon_{zz}) \end{array} \right\} & n\epsilon_{xy} & n\epsilon_{xz} \\ b'\epsilon_{zx} + iP\epsilon_{yj}k^j & n\epsilon_{xy} & \left\{ \begin{array}{l} l\epsilon_{yy} + \\ m(\epsilon_{xx} + \epsilon_{zz}) \end{array} \right\} & n\epsilon_{yz} & \\ b'\epsilon_{xy} + iP\epsilon_{zj}k^j & n\epsilon_{xz} & n\epsilon_{yz} & \left\{ \begin{array}{l} l\epsilon_{zz} + \\ m(\epsilon_{xx} + \epsilon_{yy}) \end{array} \right\} \end{pmatrix} .$$

In the case of a strained semiconductor the ϵ_{ij} are the components of the (symmetric) strain tensor for cubic materials [53]. The CB edge E_c and the average valence band energy absolute, average VB energy E'_v (defined from the model-solid theory [54]), as well as the Kane parameters A' , L' , M , N' , and P , and the strain coefficients l , m , and n are calculated by [45, 48]

$$\begin{aligned} E_c &= E_v + V_{\text{ext}} + E_0 \\ E'_v &= E_v + V_{\text{ext}} - \frac{\Delta_0}{3} \\ A' &= \frac{\hbar^2}{2m_0} \left(\frac{1}{m_e} - \frac{E_p}{E_0} \frac{E_0 + 2\Delta_0/3}{E_0 + \Delta_0} \right) \\ P &= \sqrt{\frac{\hbar^2}{2m_0} E_p} \\ L' &= \frac{P^2}{E_0} - \frac{\hbar^2}{2m_0} (\gamma_1 + 4\gamma_2) \\ M &= -\frac{\hbar^2}{2m_0} (\gamma_1 - 2\gamma_2) \\ N' &= \frac{P^2}{E_0} - \frac{3\hbar^2}{m_0} \gamma_3 \\ l &= 2b_v + a_c - a_g \\ m &= a_c - a_g - b_v \\ n &= \sqrt{3} d_v \end{aligned}$$

The matrices G_{SO} and Γ describe the spin-orbit splitting. They are given by

$$(2.10) \quad G_{SO} = \frac{\Delta_{SO}}{3} \begin{pmatrix} 0 & 0 & 0 & 0 \\ 0 & 0 & -i & 0 \\ 0 & i & 0 & 0 \\ 0 & 0 & 0 & 0 \end{pmatrix}$$

and

$$(2.11) \quad \Gamma = \frac{\Delta_{SO}}{3} \begin{pmatrix} 0 & 0 & 0 & 0 \\ 0 & 0 & 0 & 1 \\ 0 & 0 & 0 & -i \\ 0 & -1 & i & 0 \end{pmatrix} .$$

so that the eight-band $\mathbf{k} \cdot \mathbf{p}$ Hamiltonian for strained bulk is parametrized by

- the fundamental band gap E_0 ,
- the spin orbit energy SO energy Δ_0 ,
- the optical matrix parameter E_p ,
- the VB edge E_v ,
- the relative Γ -point CB mass m_e ,
- the three Luttinger parameters γ_1 , γ_2 , and γ_3 ,

- the Kane parameter B ,
- the hydrostatic CB deformation potential a_c ,
- the hydrostatic band gap deformation potential a_g ,
- the uniaxial ([100] direction) VB deformation potential b_v ,
- the uniaxial ([111] direction) VB deformation potential d_v ,
- the parameter b' coupling the CB edge to shear strain,
- and an optional scalar potential V_{ext} describing an electric field resulting, e. g., from a built-in voltage in a p-n-junction, an externally applied voltage, or a piezoelectric charging.

The hydrostatic gap deformation potential is related to the hydrostatic CB and VB deformation potentials by $a_g = a_c - a_v$. Using the relation

$$E_p = \frac{3E_0(E_0 + \Delta_0)}{\Delta_0} \left(\gamma_1 - \frac{1}{m_{\text{SO}}} \right) ,$$

the Kane parameters A' and P can alternatively be calculated using m_{SO} instead of E_p [48].

2.3.2. Heterostructures. In case of a heterostructure the above mentioned material parameters become spatially dependent. If the heterostructure, in addition, is inhomogeneously strained also the strain tensor is a function of the spatial position. The six Kane parameters A' , B , L' , M , N' , and P , and the six strain components appear in the matrix G in products together with the wave vector \mathbf{k} . Since the spatial position operator and the wave number operator do not commute, G – and thus the Hamiltonian – is not generically Hermitian for heterostructures.

In order to retain the Hermiticity of the Hamiltonian it is necessary to replace any such product of wave vector components k_i with a Kane parameter or a strain component (both called Q below) by symmetrization respective symmetrized products [33]:

$$\begin{aligned} Qk_i &\rightarrow (Qk_i + k_iQ)/2 & , \\ Qk_ik_j &\rightarrow (k_iQk_j + k_jQk_i)/2 & , \\ i, j &= x, y, z & . \end{aligned}$$

The $\mathbf{k}\cdot\mathbf{p}$ model, when applied to small quantum structures, has in principle a few well-known drawbacks which have been examined in detail in Ref.[55, 56]. They are basically related to the fixed number of Bloch functions used for the wavefunction expansion, the restriction to the close vicinity of the Brillouin zone center and to the limited ability to account for the symmetry of the underlying lattice. These problems do not arise in microscopic theories like the empirical pseudopotential method [55] (EPM) or the empirical tight-binding method (ETB),[57, 58] which a priori have greater potential accuracy. This potential, however, can only be exploited if the corresponding input parameter - the form factors in the EPM or the tight-binding parameter and their strain dependence in the ETB - are known with sufficient accuracy. Reliable generation of these parameters, however, is highly nontrivial and yet, at least, controversial. One of the most appealing features of the $\mathbf{k}\cdot\mathbf{p}$ model, in contrast, is the direct availability of all parameters entering the calculations and the corresponding transparency of the method. Additionally, the required computational expense of the method is comparatively small. The material parameters used in this work are taken from Ref. [3].

The impact of strain on the local band edges as a function of the QD geometry will be discussed in the next section.

2.3.3. Strain versus Confinement Profile. In this section we address the shape dependence of the strain field and the resulting confinement potential. For this purpose we consider a full (17.2 nm base length) and a truncated pyramid (aspect ratio = 0.21), both having the same volume. The local band edges (Fig. 2.5 (b) and (d)) are obtained by pointwise diagonalization of the Hamiltonian H at $\mathbf{k}=0$. For the sake of clarity we resort to a simpler approximation of the local band edges employing the following formulas for the conduction, the heavy hole (HH) and the light hole (LH) bands (thus ignoring shear strain induced

HH-LH coupling and split-off band contributions [59]):

$$(2.12) \quad \begin{aligned} V_{CB}(\mathbf{r}) &= E_{CB} + a_c \epsilon_H(\mathbf{r}) , \\ V_{HH}(\mathbf{r}) &= E_{VB} + a_v \epsilon_H(\mathbf{r}) + \frac{b}{2} \epsilon_B(\mathbf{r}) , \\ V_{LH}(\mathbf{r}) &= E_{VB} + a_v \epsilon_H(\mathbf{r}) - \frac{b}{2} \epsilon_B(\mathbf{r}) , \end{aligned}$$

where the hydrostatic strain ϵ_H and the biaxial strain ϵ_B are defined as

$$\begin{aligned} \epsilon_H(\mathbf{r}) &= \epsilon_{xx}(\mathbf{r}) + \epsilon_{yy}(\mathbf{r}) + \epsilon_{zz}(\mathbf{r}) , \\ \epsilon_B(\mathbf{r}) &= \epsilon_{xx}(\mathbf{r}) + \epsilon_{yy}(\mathbf{r}) - 2 \epsilon_{zz}(\mathbf{r}) . \end{aligned}$$

V_{HH} and V_{LH} are the heavy-hole and light-hole bands, a_c , a_v , b the deformation potentials, and $E_{CB/VB}$ the unstrained band edge energies. In this simplified picture the hydrostatic strain shifts the CB-edge as a whole and the biaxial strain introduces a splitting between the heavy and light-hole band edge. That means – provided the hydrostatic strain remains constant or a_v is very small – that an increasing biaxial strain reduces the energy gap. Figure 2.5 provides more insight on how the corresponding strain quantities affect the confinement potential. The larger hydrostatic strain inside the full pyramid increases the CB potential more than for the truncated pyramid. The smaller biaxial strain and its sign change at the QD-center on the other hand lead to a smaller splitting and a crossing of HH and LH band edges for the full pyramid. Both effects lead to a deeper confinement of both, electrons and holes, with decreasing aspect ratio.

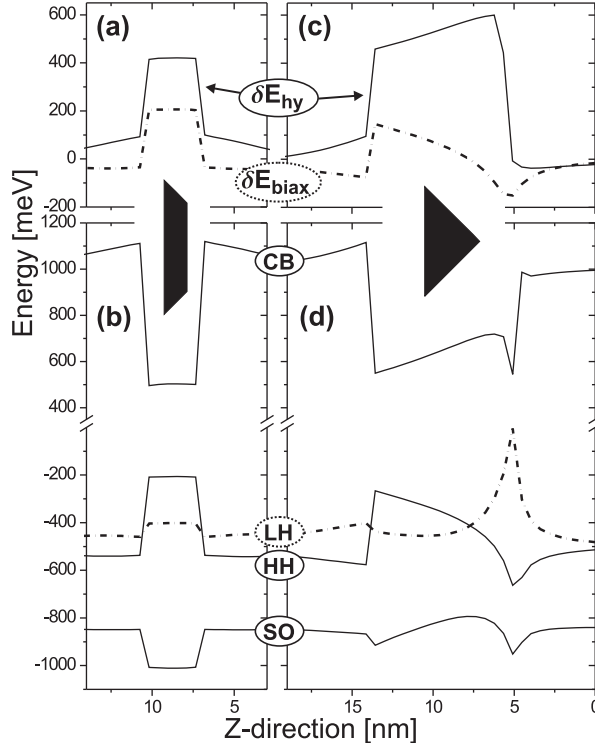


FIGURE 2.5. Impact of strain on local band edges for the case of a full and a truncated pyramid. (a) and (c): The dotted lines indicate the energy shift of the valence band imposed by biaxial strain: $\delta E_{hh/lh} = \frac{b}{2} \epsilon_B(\mathbf{r})$. The solid line marks the contribution of the hydrostatic strain $\delta E_c = a_c \epsilon_H(\mathbf{r})$. The resulting local band edge positions are shown in panels (b) and (d). While the HH-band inside the truncated QD is always above the LH-band, a crossing between HH- and LH-band edge occurs in the full pyramid (d).

Lets now have a look at the deformation of a lattice unit cell at different positions of the QD for different geometries:

Geometry	Piezoelectric potential	Symmetry group	Electron states						Irreducible Representations
			E1	E2	E3	E4	E5	E6	
		$C_{\infty v}$							
		C_{4v}							
		$C_{\infty v}$							
		C_{2v}							

FIGURE 2.6. Electronic states classified according to the irreducible representations of the symmetry groups $C_{\infty v}$, C_{4v} and C_{2v} . The symmetry lowering from $C_{\infty v}$ down to C_{4v} and C_{2v} can arise from a change of geometry, from a piezoelectric field or from the ASA effect.

(a) A unit cell in the center of a *cubic* InAs/GaAs-QD is a cube. Since the strain components ϵ_{xx} , ϵ_{yy} , and ϵ_{zz} have the same value, no biaxial strain is present. The hydrostatic strain is compressive, i.e., negative. (b) If the cubic QD gets flattened, the lateral pressure exceeds the vertical one and the unit cell extends in z-direction. Hence, the ϵ_{zz} component is larger than ϵ_{xx} and ϵ_{yy} , the biaxial strain is negative and the HH edge resides above the LH edge. (c) The pyramidal case is more complex: At the center of the QD-base a unit cell is elongated in z-direction leading to negative biaxial strain. Near the tip, however, the lateral forces become smaller than the vertical (directed towards the cell) forces. Consequently, the unit cell becomes flat with positive biaxial strain and the light-hole band edge moves on top. Thus, the QD aspect ratio determines the lateral and the vertical pressure proportion acting on a unit cell.

2.3.4. Symmetry properties of the single particle states. Let us first recapitulate some basic properties which apply to almost all QDs considered here. The confined electron states can be classified according to the number of nodal planes of the envelope function: 0 planes correspond to *s*-like, 1 plane to *p*-like, 2 planes to *d*-like states *etc*. An alternative description links their transformation behaviour under the QDs symmetry operations to the irreducible representations of the symmetry group. This is exemplified in Fig. 2.6 for the *s*, *p* and *d*-shell for three typical QDs: a flat lens ($C_{\infty v}$), a full pyramid in absence (C_{4v}) and presence of piezoelectricity (C_{2v}). Since only the last case – with C_{2v} confinement symmetry – is of practical interest, Stier *et al.* [3] introduced a labeling scheme $|abc\rangle$ where *a*, *b*, and *c* are the number of nodes in $[1\bar{1}0]$, $[110]$, and $[001]$ directions, respectively. The correspondence of this scheme to the irreducible representations of C_{2v} is shown in Fig. 2.6.

For the confined hole states such a classification is more complex due to the mixing of HH and LH parts, which can have different symmetry properties.[33]

2.3.5. Heavy hole - Light hole coupling. For the understanding of the polarization properties of the excitonic absorption spectra the HH-LH coupling and the resulting state mixing is of largest importance. There are three main mechanisms that finally determine the HH/LH ratio of the hole wavefunctions: First, the relative position of the local HH and LH band edge, second, their masses relative to each other, and third, the coupling strength among the VBs, which is mainly a function of the shear strain (see Bahder [52]):

Heavy-hole and light-hole states are decoupled, if $\epsilon_{xx} = \epsilon_{yy}$, and, if the shear strain components $\epsilon_{xy}, \epsilon_{xz}, \epsilon_{yz}$ are absent.

The first and the third mechanism are tightly linked to the QD geometry: In the first case, the inhomogeneity of the strain (especially the biaxial strain, see Eq. 2.12) leads to a splitting of the local HH-LH band edges [Fig. 2.5 (b)] and possibly to a crossover of the two bands, if the biaxial strain changes its sign as in the case a full pyramid [Fig. 2.5 (d)]. In this case (large aspect ratio), also the shear strain becomes large, leading to increased HH-LH coupling. For flat QDs, in contrast, the shear strain becomes small as does the HH-LH coupling. As a result, the LH percentage of the hole ground state – an indicator for the strength of the coupling – varies in square based QDs from 9.2 % for the full pyramid to 2.8 % for a flat truncated pyramid. For circular based QDs we observe a variation between 14.4 % (half sphere) and 2.8 % (flat lens). The dependence on the aspect ratio is similar to that of the (first order) piezoelectric field, since both, the HH-LH coupling and the (first order) piezoelectric field, originate from the presence of shear strain.

The magnitude of the light hole projection also depends heavily on the QD size, as can be seen in Fig. 2.7. In average, the LH percentage increases for higher excited hole states and – except for the hole ground state – it increases for decreasing QD size, when the hole energies approach the GaAs VB edge.

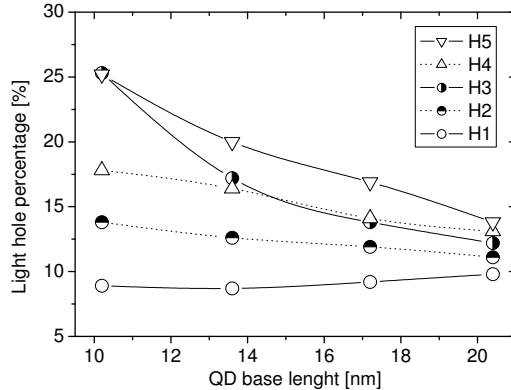


FIGURE 2.7. The light hole percentages of the first five hole states shown for the series A as a function of the QD base length.

2.4. Many-Particle States

As soon as more than one charge carrier is confined in the QD, the influence of direct Coulomb interaction, exchange effects, and correlation lead to the formation of distinct multi-particle states. These states are calculated here utilizing the configuration interaction method. This method rests on a basis expansion of the excitonic Hamiltonians into Slater determinants. These consist of antisymmetrized products of single-particle wavefunctions being obtained from eight band $k \cdot p$ theory in our case. The method is applicable in the strong confinement regime, since the obtained basis functions are already similar to the weakly correlated many-body states.

2.4.1. The Configuration Interaction Model. Configuration interaction (CI) is a linear variational method for solving the few-particle Schrödinger equation. Two meanings are connected to the term configuration interaction in this context. Mathematically, configuration simply describes the linear combination of Slater determinants used for the wavefunctions. In terms of a specification of orbital occupation, interaction means the mixing (interaction) of different electronic configurations (states).

In order to account for correlation, CI uses a variational wavefunction $|\Psi_N^\alpha\rangle$ (N is the number of particles, and α is an index to label the few-particle states), which is a linear combination of configuration state functions (CSFs) $|\Phi_{a,b,c..}\rangle$ built up from single particle orbitals:

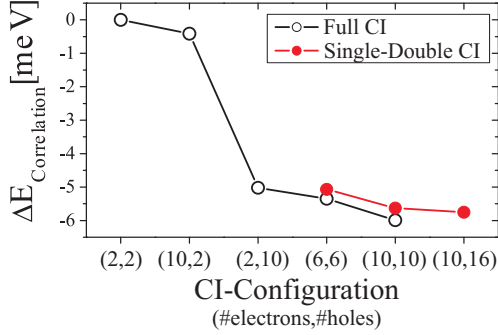


FIGURE 2.8. The biexciton correlation energy as a function of the used CI-configuration (i,j) , where i is the number of electron states and j the number of hole states being included to built up the CI-basis. Results for Full CI are compared to that of Single-Double CI. For the configurations $(2,2)$, $(10,2)$ and $(2,10)$, FCI and SDCI are identical and not depicted.

$$(2.13) \quad |\Psi_N^\alpha\rangle = \sum_{a,b,c\dots} C_{a,b,c\dots}^\alpha |\Phi_{a,b,c\dots}\rangle .$$

As an example, the exciton ground state configuration (cf) (i,j) consists of the four Slater determinants $|\Phi_{e_i,h_j}\rangle$ with i and j being the number of electron and hole ground states, $i, j \in 1, 2$.

If the expansion includes all possible CSFs, it is called a full configuration interaction (FCI) procedure which exactly solves the Schrödinger equation within the space spanned by the one-particle basis set. This is not feasible in our case. Therefore we restrict ourselves to the inclusion of all bound orbitals, where i runs over all confined electron and j over all confined hole states. The other CSFs can be characterized by the number of ground state orbitals that are interchanged with excited states orbitals from the ground-state determinant. If only one spin orbital differs, it is described as a single excitation determinant, (single CI). If one or two orbitals differ it is a single-double excitation determinant (single-double CI [SDCI]) and so on. This is used to limit the number of determinants in the expansion.

2.4.1.1. Role of the basis size. Since we restrict ourselves to a basis built up from bound orbitals only, part of the correlation energy is not included in our approach. Shumway and coworkers [60] estimated this defect by comparing their FCI results for similar QDs having the same restricted expansion basis to a quantum Monte Carlo treatment. They found that their CI calculations cover about 80 % of the total correlation energy.

As an example, we compare in Fig. 2.8 the biexciton correlation energies, $\delta_{\text{Corr}}(XX)$, for a FCI and a SDCI calculation for an InAs pyramid (17.2 nm base length) as a function of the number of configurations that are taken into account. For the biexciton-configurations $(2,2)$, $(2,10)$ and $(10,2)$, the FCI and SDCI are equivalent. Two prominent features are highlighted:

First, the correlation energy is much more sensitive to the number of hole states than to the number of electron states, as can be seen by comparing the $(2,2)$ to $(2,10)$ and the $(2,2)$ to $(10,2)$ configuration.

Second, the results for the FCI deviate very little, if at all, from SDCI. The appealing property of the SDCI in this context is the largely reduced number of required matrix elements: For the $(10,10)$ FCI, e.g., eight times more elements are to be evaluated than for the $(10,16)$ SDCI.

The evolution of the basis size with increasing number of carriers is shown in table 2 for the full CI method. It highlights the factorial growth in the number of matrix elements, which inhibits the usage of the FCI method for larger number of carriers in an excitonic complex.

2.5. Optical Properties

2.5.1. Interband spectra. The interband absorption spectra are calculated by Fermi's golden rule applied to excitonic states obtained from the configuration interaction method.[33]

TABLE 2. Relation between particle type, basis size, number of matrixelements (ME) and number of *nonzero* ME if 6 electron- and 10 hole states contribute to the full configuration.

particle type	basis size	No. of ME	No. of <i>nonzero</i> ME
X	60	3600	1830
X^-	150	22500	7275
X^+	270	72900	17685
XX	675	455625	63450

There exist no strict selection rules for the decay of excitons. As a rule of thumb one can say that those transitions have a large oscillator strength where electron and hole state share the same symmetry properties *and* have a sizable spatial overlap. However, since the hole states consist of HH and LH parts, each with its own symmetry, they have finite recombination probabilities with several different electron states of different symmetry character.

2.5.2. Intraband spectra. In contrast to the excitonic decay, the CB intraband transitions follow strict transition rules: for two electron states, $|a\rangle = |ijk\rangle$ and $|b\rangle = |i'j'k'\rangle$, it is a neccesary condition that at least one of the expressions $i-i'$, $j-j'$ or $k-k'$ is an odd number. For example the transition between the electron states $|100\rangle \rightarrow |000\rangle$ has a sizeable oscillator strength in contrast to $|200\rangle \rightarrow |000\rangle$, which is a forbidden transition. In general, the oscillator strength is smaller than for excitonic transitions, but the anisotropies between absorption in $[110]$ and $[1\bar{1}0]$ direction are much larger. The latter is an ideal fingerprint of the electronic spectrum of QDs and the associated symmetry properties of the wavefunctions.

Part 2

InGaAs/GaAs Quantum Dots

CHAPTER 3

Impact of Size, Shape and Composition on Piezoelectric Effects and Single-Particle States

The inhomogeneous strain in and around the QDs, the piezoelectric fields, and the atomistic symmetry anisotropy (ASA) are closely interrelated. The lack of inversion symmetry of the underlying zinc-blende lattice together with strain is conditional for the presence of a piezoelectric field, but moreover it has a separate impact on the electronic states, referred to as ASA.[43] Grundmann *et al.*[2] and Stier *et al.*[3] discovered the linear (first order) piezoelectric effect to cause symmetry lowering from C_{4v} to C_{2v} for pyramidal QDs. Later, Bester *et al.*[43] reported a similar behaviour for lens-shaped QDs, where the rotational symmetry, $C_{\infty v}$, is lowered to C_{2v} as well, with similar consequences as for the pyramidal QDs. Recently Bester *et al.*[11] investigated quadratic (second order) piezoelectric effects and again investigated flat lens-shaped QDs.[42] The authors reported that the linear and quadratic effects oppose and cancel each other leading to an almost field-free QD-interior, thus practically restablishing the $C_{\infty v}$ confinement symmetry. However, mutual cancellation of first and second order piezoelectric effects cannot be generalized to lower symmetry and more realistic QD structures, as will be shown in this chapter.

The electron p -state splitting presents a measure for the actual confinement anisotropy between the [110] and the [1 $\bar{1}$ 0] directions. Bras *et al.*[61, 62] performed intraband absorption measurements and suggested an electron p -state splitting in the order of 8 meV for capped InAs QDs. As we will see later in this chapter, their polarization anisotropy corresponds to a lower p -state aligned along [1 $\bar{1}$ 0] and a higher energy state, aligned along [110]. This finding is in accord with the results of Maltezopoulos *et al.*[63] They used *scanning tunneling spectroscopy* to probe *uncapped* QDs and found striking evidence for large p -state splitting, with identical p -state order to Bras *et al.* Moreover, they observed d -states below the second p -state in some cases.

The purpose of this chapter is twofold. (i) First, the electronic and optical properties of a large number of QDs of varying size, shape (square/circular/rhomboid base, different vertical/lateral aspect ratios) and composition (homogeneous/peaked and isotropic interdiffusion) will be calculated, highlighting the impact of the varying first and second order piezoelectric effects on the electronic properties.

(ii) Despite tremendous advances in structural characterization the real shape and composition of capped quantum dots, which are decisive for all applications,[1] are usually not or only poorly known. Therefore, the second purpose of our work is to predict spectroscopic quantities presenting fingerprints for specific QD structures, thus addressing the inverse problem of deriving information on size, shape and composition from spectroscopic data. The feasibility of this approach will be demonstrated in Chapter 5, employing the multimodal size distribution of InAs/GaAs QDs as test case.

3.1. The Investigated structures: Variation of size, shape and composition

Our selection of model QDs is guided by the reported broad variation of structures observed in experiment (see e.g. [64, 65] and references therein).

Figs. 3.1, and 3.2 give an overview on the investigated structure series and their classification according to their size, shape and composition. The following series are considered:

Series A: The pyramidal InAs/GaAs structures similar to Ref. [3] with base lengths 10.2 nm (A1), 13.6 nm (A2), 17.0 nm (A3), and 20.4 nm (A4)

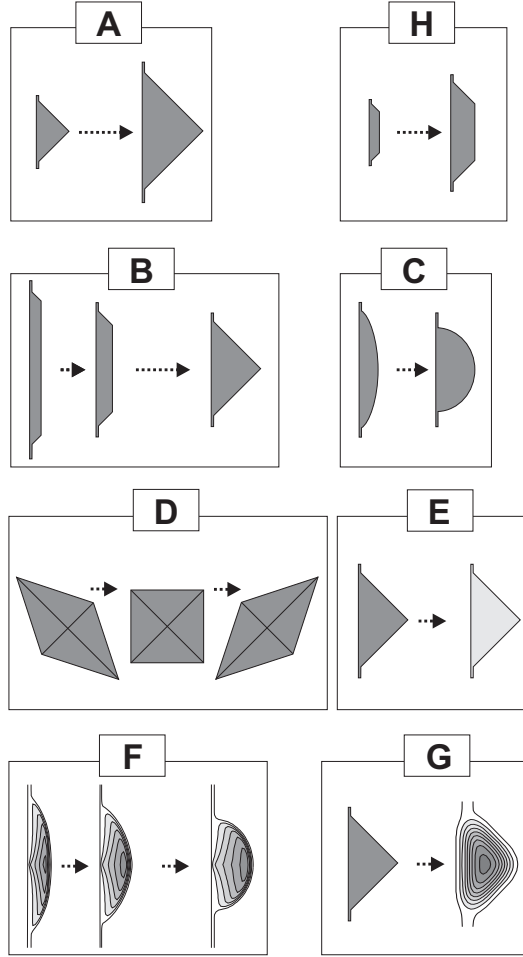


FIGURE 3.1. Model structures investigated throughout this work.

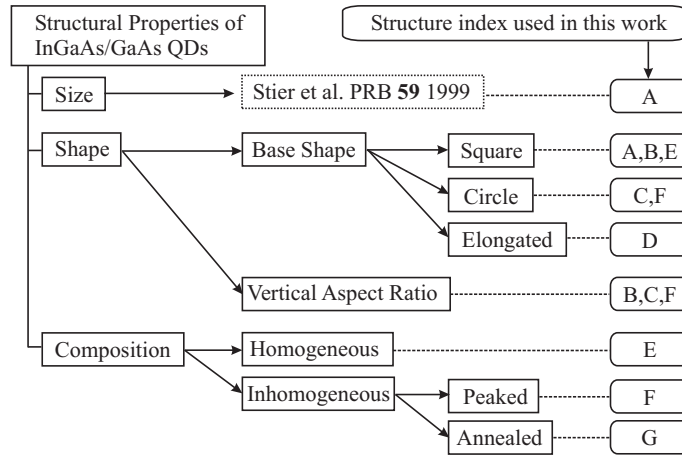


FIGURE 3.2. Overview over the structures used in this work and their classification according to their morphology.

Series B: Starting with the 17 nm base length pyramid of series A, the vertical aspect ratio, ary_V , is varied between 0.5 (full pyramid) and 0.04 (very flat QD).

Series C: The QDs have a circular base and their vertical aspect ratio varies between 0.5 (half-sphere) and 0.17.

Series D: Starting again with the 17 nm base length pyramid of series A an elongation in [110] and [1 $\bar{1}$ 0] direction is explored. The lateral aspect ratio, arL, (length in [110] direction divided by length in [1 $\bar{1}$ 0] direction) varies between 2 and 0.5 (a value of 1 corresponds to the square base).

It is important to note, that the QD volume has been kept constant for series B, C and D.

Series E: A homogeneous variation of the In-content for In_xGa_{1-x}As/GaAs is considered. The starting point again is the 17 nm base length pyramid of series A. The In content decreases in steps of 10% from 100% to 70%.

Series F: The QDs of this series have a circular base together with a trumpet-shaped like InGaAs composition profile. The integral In amount of the QDs is equal to QDA3.

Series G: By applying a smoothing algorithm on structure A3 with variable smoothing steps (N) the process of Fickian diffusion as a result of an annealing procedure is simulated.

Series H: In addition to the previous list of series we add a special series that is closely related to experiments carried out by Rodt *et al.*[66] Due to the multimodal distribution of the PL peaks of the investigated samples it was possible to derive the structure of the participating QDs to unprecedented detail. It was found that the QDs responsible for each of the nine well separated peaks differ by one monolayer in height and base length as can be seen in Fig. 3.1 (H). The smallest QD starts with a height of 3 monolayer and a base length of 9.1 nm and the largest one ends with 11 monolayer height and 13.6 nm base length, respectively. This series will be the base for the comparison to experiment in chapter 5.

3.2. The Impact of the piezoelectric field

3.2.1. First and second order piezoelectricity as function of size, shape and composition of the QD. In this section we explore the balance between linear and quadratic piezoelectric terms as a function of shape and composition of the QDs. In Fig. 3.3 the piezoelectric potentials of five different QDs are shown as a lateral 2D slice taken at the z-component of the QD barycenter. For all shown QDs, the first and second order term are quadrupole-like, but oriented in opposite directions. The appearance of the net potential at a larger distance from the QD is dominated by the first order term, an important issue for stacked QDs (see chapter 6). The prevailing term inside the QD is determined by the actual geometry and the composition profile as will be detailed now.

(a) *Flat, lens-shaped QDs.* The interior of flat lens shaped QDs is almost field-free [see Fig. 3.3 (a)], due to the cancelation of the first and second order piezoelectric contributions. These findings confirm the results of Bester *et al.*[42]

(b) *Pyramidal QDs.* In contrast to the lens-shaped QDs, for pyramidal InAs QDs with {101} - facets the quadratic term strongly dominates inside the QD [see Fig. 3.3 (b1) and Fig. 2.4]. A rotation by 45° [see Fig. 3.3 (b2)], however, leads to a balance of both contributions and results in a field-free QD as in case (a).

(c) *Homogeneous alloying.* Now we consider an In₇₀Ga₃₀As pyramidal QD. The linear piezoelectric potential remains unaffected and is almost as large as for the pure InAs QD in (b1). This seems surprising at first sight, since the shear strain components become smaller for rising Ga content. This decrease, however, is compensated by the larger first order piezoelectric constant e_{14} , which is linearly interpolated between the values of InAs and GaAs (see table 1). The second order field, in contrast, drops drastically for two reasons: First, the diagonal and the nondiagonal strain, entering the calculation as products in Eq. 2.1, both diminish. Second, the parameter B_{124} , which leads the largest contribution of \mathbf{P}_2 , becomes smaller. As a result, the interior piezoelectric field of the QD is dominated by the first order term.

(d) *Annealed pyramid.* The first order potential of an annealed structure shows only minor changes in the field distribution compared to the InAs pyramid (b1). The second order potential – similar to case (c) – is drastically reduced. This strong decrease has been observed already for the first annealing step. Thus, it appears that the second order term is very sensitive to the degree of interface abruptness. In the resulting overall potential only a very small portion of the QD interior is still dominated by the second-order field.

(e) *Trumped shaped composition profile.* Here we consider a different InAs distribution compared to case (d) but the field distribution is very similar to the case of the annealed pyramid.

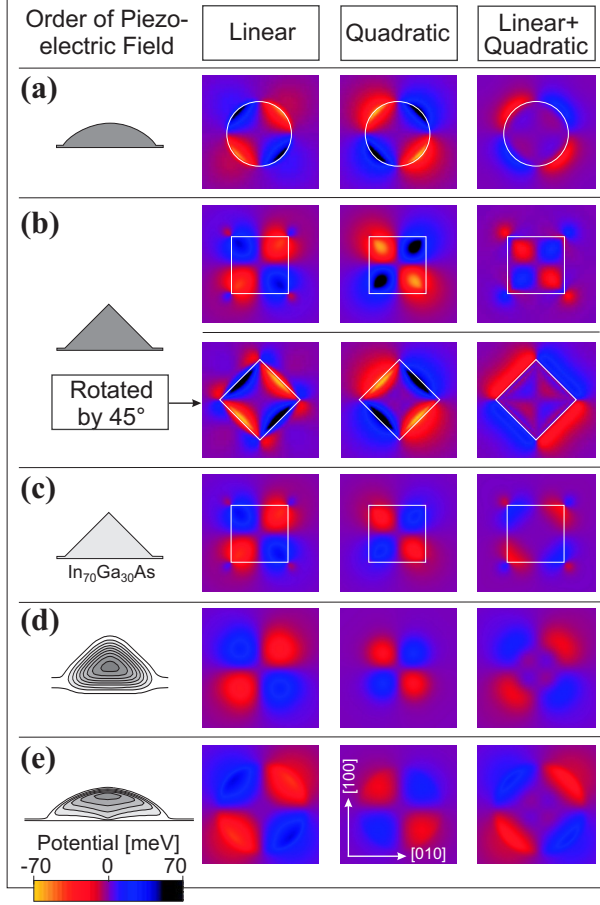


FIGURE 3.3. Lateral scans through the piezoelectric potential: linear part (left), the quadratic part (middle) and the sum of both (right) shown for different variations of the QD morphology. (a) a lens-shaped QD from series C (vertical aspect ratio, $\text{ary} = 0.21$), (b) a full InAs pyramid from series A with a base length of 17.2 nm. In the first case the base edges are oriented along [100] in the second the pyramid is rotated by 45°, hence, the edges are oriented along [110]. (c) The In fraction of the pyramid from (b) is decreased down to 70% (from series E). (d) An isotropic diffusion procedure is applied to QD (b) (from series G). (e) Here we show results for a nonisotropic internal InAs composition profile taken from series F.

To conclude this section, we find that the results of Bester *et al.*[42] are a special case applicable to lens-shaped QDs within a certain aspect ratio only. Their findings cannot be generalized to all QD geometries and composition profiles.

3.2.2. Impact on the single-particle states. Electron and hole states respond in different ways to the piezoelectric potential. For the electron states it is just a minor perturbation lifting possible degeneracies of p - and d -states. The shapes of the wavefunctions themselves are hardly affected. The hole states, in contrast, follow very closely almost any potential variation to minimize their potential energy. This behaviour is connected to the very different effective masses of both carrier types, which plays the role of a weighting factor in the trade-off between kinetic and potential energy.

For the electrons, their small effective mass translates into a steeply rising dispersion $E(\mathbf{k})$. As the kinetic energy in \mathbf{k} -space is defined as $E_{\text{kin}} \approx \int_{V_k} E(\mathbf{k}) \Psi(\mathbf{k}) d\mathbf{k}$, a steep $E(\mathbf{k})$ makes E_{kin} very sensitive to a \mathbf{k} -space wavefunction spread-out. As a result, the wavefunction in real-space is very stiff and reluctant to adapt to small potential fluctuations, because otherwise it would produce $\Psi(\mathbf{k})$ components remote from the Γ -point.

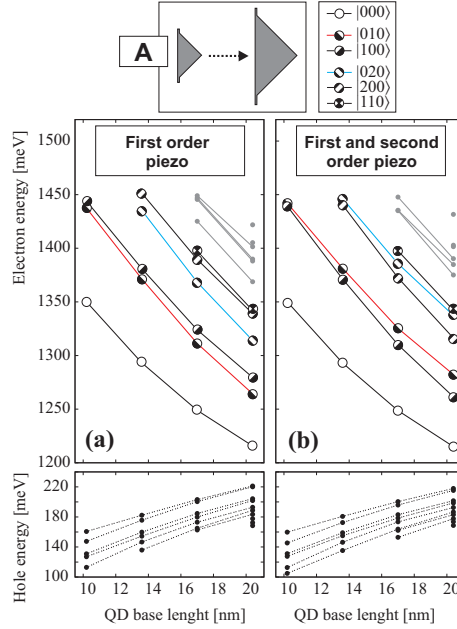


FIGURE 3.4. Single-particle electron and hole energies for pyramidal QDs with different size (series A). In the left panel (a) only the first order piezoelectric effect is accounted for, using the experimental value of ϵ_{14} . In the right hand panel also the second order is taken into account, using the piezoelectric constants from Ref. [11].

For the hole states, especially for those with a large HH-fraction, the situation is reversed. The $E(\mathbf{k})$ function is very flat and a larger $\Psi(\mathbf{k})$ spreadout does result only in a small gain of kinetic energy. Therefore, the hole states can adapt to tiny details of the potential landscape, thus, minimizing their potential energy.

Some principal features of the first and second order piezoelectric potential are already described in Sec. 2.2. Here we proceed by studying their impact on the single-particle states. For this purpose we have calculated the single-particle energies and wavefunctions for our structures employing two piezoelectric models: (1) the classical experimental value e_{14} was used and any quadratic effect omitted, and (2) the values of e_{14} and $B_{\mu j k}$ from Ref.[11] were taken, thus, accounting for linear and quadratic piezoelectric terms.

To probe the impact of the different orders of piezoelectricity, we monitor the p -states $|100\rangle$ and $|010\rangle$ and the d -states $|200\rangle$ and $|020\rangle$ as a function of the order of the piezoelectric tensor [case (1) or (2)]. These states are chosen since electron orbitals $|ijk\rangle$ with $i \neq j$ respond very sensitively to the piezoelectric field, whereas those with $i = j$ remain almost unaffected.

Pyramidal and truncated pyramidal QDs (Series A/B). The strength of the first order piezoelectric field [case (1)] and the resulting p - and d -state splitting is a function of the QD-height [3] [see also Fig. 3.4 (a)]. As can be seen from Fig. 3.4 (b), this applies even more if the second order is taken into account too [case (2)]; the p -state order, however, is reversed compared to case (1). The same applies to the $|200\rangle$ and $|020\rangle$ d -states.

Lens-shaped InAs QDs (Series C). Compared to the series A and B the second order piezoelectric potential exceeds the first order terms inside the QD only in the case of a halfsphere as can be seen from the reversed p -state splitting in Fig. 3.6 at $\text{ary} = 0.5$. For a smaller aspect ratio, $\text{ary} < 0.5$, the p -states and the $|200\rangle$ and $|020\rangle$ d -states are degenerate, indicating that first and second order effects compensate each other with respect to their impact on the electronic states. If we consider the first order piezoelectric field alone [case (1)], even for the structural $C_{\infty v}$ QDs a p - and d -state splitting is found.

For the hole orbitals no degeneracy is observed, neither for case (1) nor for case (2).

Comparison of wavefunction orientation between square and circular based InAs QDs (series B and C).

Figure 3.7 shows the order and orientation of the wavefunction for a truncated pyramid from series B and a lens-shaped QD from series C both sharing the same vertical aspect ratio, ary , of 0.21. As long as

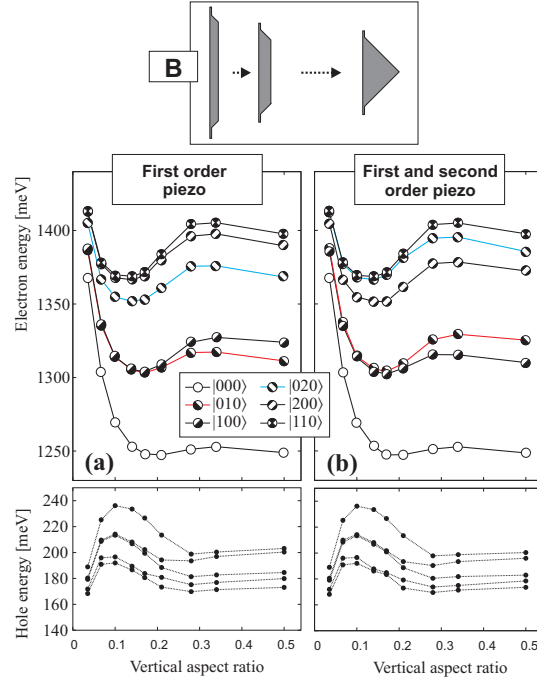


FIGURE 3.5. Single-particle electron and hole energies for truncated pyramids (series *B*) versus the vertical aspect ratio ary . In the left panel (a) only the first order piezoelectric effect is accounted for, using the experimental value of ϵ_{14} . In the right hand panel (b) also the second order is taken into account, using the piezoelectric constants from [11].

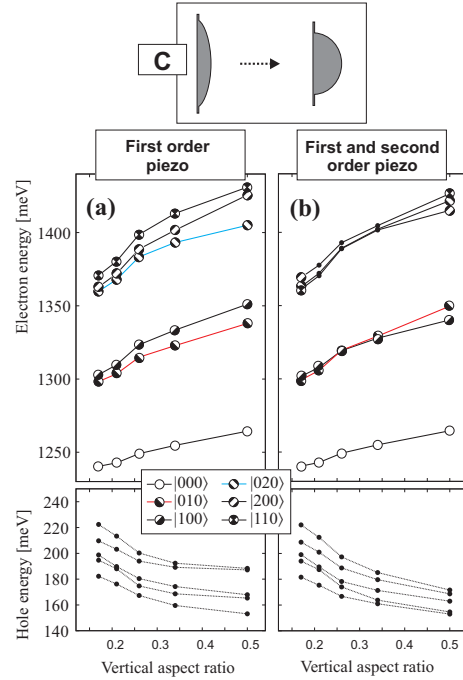


FIGURE 3.6. Single-particle electron and hole energies for lens-shaped QDs (series *C*) versus the vertical aspect ratio ary . In the left panel (a) only the first order piezoelectric effect is accounted for, using the experimental value of ϵ_{14} . In the right hand panel (b) also the second order is taken into account, using the piezoelectric constants from [11].

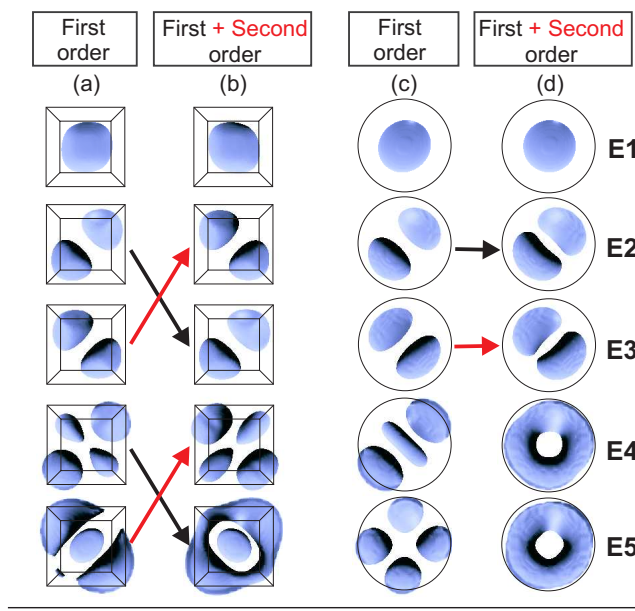


FIGURE 3.7. Comparison of the electron wavefunction shapes and order for different orders of the piezoelectric tensor as a function of the QD base shape. On the left hand side a truncated pyramid from series B and on the right hand side a flat lens-shaped QD from series C is considered.

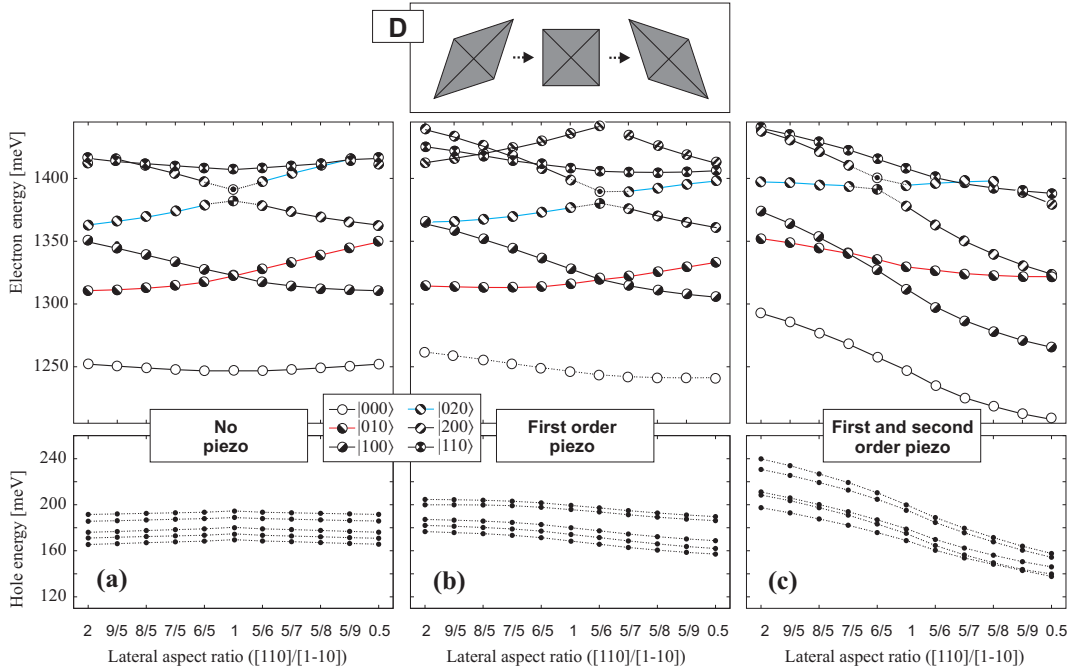


FIGURE 3.8. Single-particle electron and hole energies for elongated QDs (series D) versus the lateral aspect ratio ar_L . No piezoelectricity is included for the results in panel (a). In panel (b) only the first order piezoelectric effect is accounted for using the experimental value of ϵ_{14} . In the right hand panel (c) also the second order is taken into account, using the piezoelectric constants from [11].

the first order terms of the piezoelectric fields are considered only, all electron wavefunctions have the same orientation, except for the state $|e_5\rangle$. If the second order is also taken into account, the p - and d -orbitals of

the truncated pyramid change their orientation. For the lens-shaped QD the p -orbitals keep their orientation, although they are almost degenerate in energy as are the d -orbitals.

Elongated QDs (Series D). In this series two of the main lateral anisotropy sources are contrasted: The elongation in [110] and [1 $\bar{1}$ 0] direction and the piezoelectric effect. To separate their influence on the single-particles the electronic states are calculated in absence [Fig. 3.8(a)] and in presence of the piezoelectric field [Fig. 3.8(b,c)]. In the former case, the electronic states are insensitive to the orientation of the QD. The spectrum shown in Fig. 3.8(a) is symmetric and the electron p -states are degenerate at a lateral aspect ratio $ar_L = 1.0$. The electronic d -states and all hole states, in contrast, show no degeneracy at all. Moreover, the d -states show an anticrossing behaviour upon changing the lateral aspect ratio from values smaller to values larger than one.

Taking the piezoelectric field into account, complicates the picture a lot [Fig. 3.8(b,c)]. Again, the second order piezoelectric field dominates over the first order field which can be seen from the p -level crossing point, which is at $ar_L = 1.2$ for case (1) (first order only) and $ar_L = -1.4$ for case (2) (first and second order). The second remarkable observation is the large energy shift of all electron and hole states for case (2) [Fig. 3.8(c)], which is much more pronounced than for case (1). However, since the shift applies to both particle types in the same way, it is not expected to be visible in the transition energies, but rather in the activation energies.

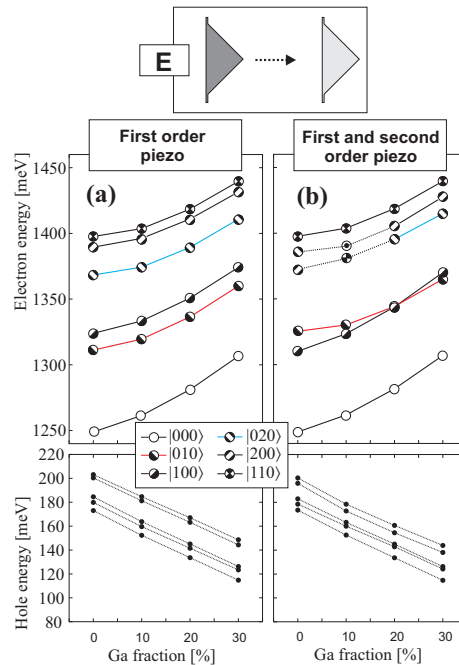


FIGURE 3.9. Single-particle electron and hole energies for series E versus the Ga fraction inside the InGaAs QD. In the left panel (a) the first order piezoelectric effect is accounted for using the experimental value of ϵ_{14} only, whereas for the right hand panel also the second order is taken into account, using the piezoelectric constants from [11].

Variation of InGaAs composition and its distribution (Series E/F/G). In this series, different manifestations of composition changes are investigated. First, the average composition determines the accumulated hydrostatic strain inside the structure. It is, in general, larger for larger In content. Since the second order piezoelectric tensor couples diagonal strain components with shear strain components, the quadratic part of the piezoelectric potential is expected to be very sensitive to composition changes.

In series E, the average In content in a pyramid is varied homogeneously. The p -state splitting resulting from the first order parts alone is not affected by the composition variation [Fig. 3.9 (a)], since the decreasing shear strain is compensated by an increasing piezoelectric constant e_{14} , resulting from the linear interpolation between the values of GaAs ($e_{14} = -0.16$) and InAs ($e_{14} = -0.045$). The second order contributions, in

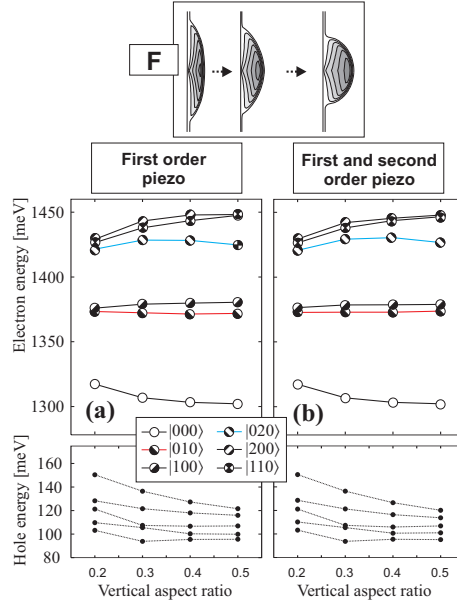


FIGURE 3.10. Single-particle electron and hole energies for series F versus the vertical aspect ratio ar_V . In the left panel (a) the first order piezoelectric effect is accounted for using the experimental value of ϵ_{14} only, whereas for the right hand panel also the second order is taken into account, using the piezoelectric constants from [11].

contrast, decrease rapidly for increasing Ga content, as can be seen in Fig. 3.9 (b), where the p -states cross at a Ga fraction of 20 %.

In series F, a trumpet-shaped composition profile is investigated for different vertical aspect ratios. Since the In atoms are spread over a wider range in a larger QD with only a small region of high In concentration, the local strain (especially the diagonal components) is smaller. This translates into a smaller first order and into a *much* smaller second order piezoelectric potential. The order of the electron states remains unchanged upon changes of the aspect ratio and introduction of second-order piezoelectricity (Fig. 3.10).

The most exciting series in this context, however, is series G. A couple of annealing steps to the QD interfaces is applied to simulate Fickian diffusion. We found that the strength of the second order piezoelectric potential is extremely sensitive to this procedure, resulting in a crossing of the p and d -states ($|200\rangle$ and $|020\rangle$) after two annealing steps [Fig. 3.11(lower panel)]. The first order potential, in contrast, is not affected at all. This behaviour might lead to the strong abrupt decrease of the exciton fine-structure splitting, which has been observed experimentally for a first very modest annealing step.[67] The fine-structure splitting in QDs is related to the same sort of anisotropy, which also causes the p -state splitting.[4]

3.2.3. Impact of the piezoelectric field on the inter- and intraband spectra. The optical spectra are determined by energy, shape and orientation of the electronic states. Especially the electron p -shell is sensitive to the various sources of lateral anisotropy: QD elongation and the ASA effect push the first electron and hole p -states into the same direction. A linear piezoelectric field, in contrast, results in an alignment in opposite directions (see Fig. 3.12).

3.2.3.1. Interband absorption spectra. In Fig. 3.13 (a1) and (b1) we compare the excitonic absorption spectra for a pyramidal QD (17.2 nm base length) and the two considered cases of the piezoelectric effect. The labels indicate the symmetry of the electron state (E_{ijk}) and the hole state Hl , which take part in the absorption process. At first sight, the spectra look very similar apart from small differences in the polarization. But some of the peaks have changed their origin, e.g., the $E010 - H1$ and the $E100 - H1$ absorption peak have reversed order in both plots.

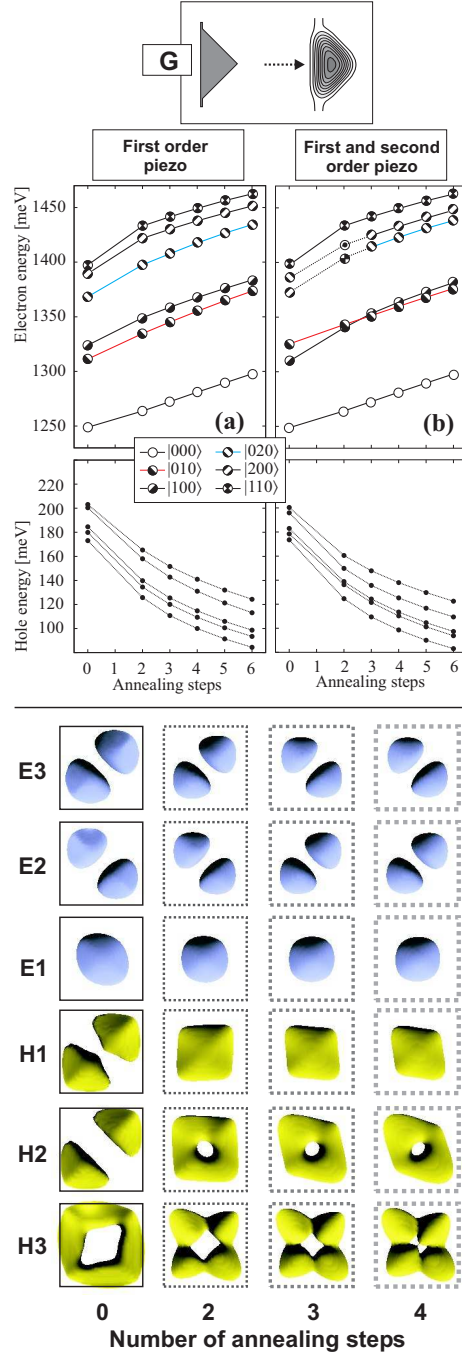


FIGURE 3.11. (upper panel) Single-particle electron and hole energies for series G versus the number of annealing steps. In the left panel (a) the first order piezoelectric effect is accounted for using the experimental value of ϵ_{14} only, whereas for the right hand panel also the second order is taken into account, using the piezoelectric constants from [11]. (lower panel) Probability density (isosurface at 65%) shown for the first three bound electron and hole orbitals as a function of annealing steps. An electron p-states reordering occurs between annealing step two. Only a small degree of annealing is necessary to significantly change the hole wavefunction shape.

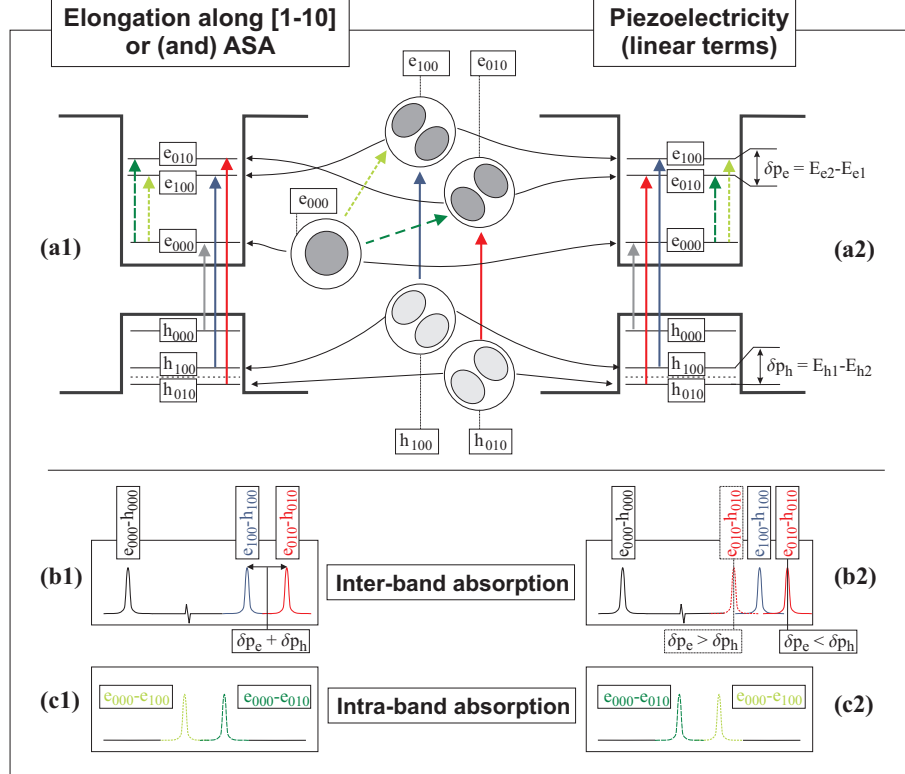


FIGURE 3.12. A possible QD elongation or the effect of the atomistic symmetry anisotropy (ASA) has a qualitatively different impact on the level ordering than a piezoelectric field (here schematically shown for first order terms only). In the latter case the first electron and hole p-states are oriented in orthogonal direction. Panel (b) schematically shows the resulting interband absorption spectra. In (b1) the p-channel splitting is the sum of the respective electron and hole p-state splitting ($\delta p_e + \delta p_h$), whereas in case (b2) the splitting is determined by the difference ($\delta p_e - \delta p_h$). Since the polarization (not shown here) of these peaks is rather weak, a distinction between the two p-channel peaks might be difficult in experiment. An additional hindsight can provide intraband transition spectra (c). These peaks are nearly 100 % polarized and allow a clear assignment of the transition type.

3.2.3.2. Intraband spectra. The situation is different for CB intraband transitions [Fig. 3.13(a2) and (b2)]. Here, the spectroscopic signature is completely different in terms of the peak energies and, in particular, with respect to the polarization. The transitions $E010 - E000$ and $E100 - E000$, being the acid test for the sequence of the p-states order, are reversed. In contrast to the interband peaks, the p-state transitions are clearly distinguishable by their polarizations: The transition $E010 - E000$ is polarized along [110] and $E010 - E000$ along [1 $\bar{1}$ 0].

3.3. The vertical and lateral aspect ratio

3.3.1. Vertical aspect ratio (series B and C). Since the relation between the vertical aspect ratio and piezoelectric field has already been discussed in Sec. 3.2.2, we continue with discussion of the influence of the vertical aspect ratio on the single-particle states, using series B (square base) and C (circular base) and highlighting the following results:

- (i) As long as the aspect ratio, ar_V , varies between 0.5 and 0.15, the localization of electron and hole states is either constant (electrons in series A) or is increasing (energy of electron states decrease and of hole states increase) with decreasing aspect ratio. This unusual finding is in contrast to what a simple particle-in-a-box model suggests and is related to the redistribution of strain inside the QD. In general

two competing processes determine the localization energies. The first one is the rising quantization in z-direction, resulting in a decreasing localization. This effect, however, becomes dominant only if the dot is very flat [$\text{ar}_v < 0.15$ (0.1) for electrons (holes), see Fig. 3.5]. The second is a redistribution of strain from being dominant hydrostatic to more biaxial [Fig. 2.5 (a) and (c)]. This process reduces the gap between the band edges [Fig. 2.5 (b) and (d)], and increases the localization energy, as discussed in section 2.3.3. As a result, the excitonic absorption spectrum of a flat QD, as shown in Fig. 3.13 (c1), is red-shifted by ca. 30 meV compared to the pyramid in panel (b1).

(ii) The increase of the localization energy with decreasing aspect ratio is much more pronounced for circular-based QDs than for square-based ones. This points at a larger degree of strain redistribution in lens-shaped QDs.

(iii) For very flat QDs, the z-quantization becomes dominant; the critical aspect ratio, however, is different for electron and hole in series *B*:

Electron shift: For $\text{ar}_v < 0.15$ the decreasing height causes an energy shift of 120 meV for the electron ground-state and 80 meV for the first excited electron state. First, for $0.1 \leq \text{ar}_v < 0.15$, the wavefunctions are compressed, thus, accumulating kinetic energy. Later, for $\text{ar}_v < 0.1$, when the z-confinement becomes too strong, they evade by spreading into the surrounding matrix, increasing the potential energy of the state. Both effects result in an increased electron energy.

Hole shift: Due to their larger mass, hole states, in general, prefer to adapt their wavefunction shape close to the details of the VB-confinement profile. Thus, the main part of the wavefunction remains inside the QD until the aspect ratio becomes smaller than 0.1. Below that value, the energy decreases by 50 meV for the ground- and 43 meV for the excited state. These shifts are attributed to the gain of kinetic energy, rather than to a barrier penetration. Even for the flattest QD, 65 % of the hole ground state wavefunction remains inside the dot, in contrast to only 47 % for the electron ground state.

3.3.1.1. *Excitonic absorption spectra.* A comparison of the excitonic absorption spectra of the full pyramidal and the truncated QD reveals significant differences, reflecting the different strain distributions and piezoelectric fields.

The magnitude of the shear strain components decreases with decreasing vertical aspect ratio, resulting in a smaller piezoelectric field and reduced HH-LH coupling. The former reduces the electron *p*-splitting leading to a degeneracy of the $E100-H1/E010-H1$ transitions, the latter reduces the LH-percentage of the hole states. Thus, the number of absorption channels is decreased from ten in the case of the full pyramid to seven in the case of the flat truncated pyramid. The $E000-H2$ peak of the pyramid in Fig. 3.13 (b1), for instance, is only visible because the sizeable LH-part of $H2$ has the same *s*-like symmetry as the $E000$ state. The HH-part of $H2$, in contrast, carries $|110\rangle$ -symmetry and can, therefore, not interact optically with the $E000$ state, as its overlap integral vanishes for symmetry reasons. For the flat truncated QD in Fig. 3.13 (c1) the LH-percentage of $H2$ is small. Consequently, the $E000-H2$ peak vanishes.

The overall appearance of the absorption spectra are quite different for different aspect ratios and should allow a discrimination in PLE experiments.

3.3.2. Lateral aspect ratio (series D). A QD elongation is often discussed as a possible source of the fine-structure splitting, since it introduces a symmetry reduction from C_{4v} to C_{2v} already on the level of the QD structure. However, as long as no piezoelectricity (or/and the ASA in the case of atomistic models) is included, there is no distinction possible between elongations along $[110]$ and $[1\bar{1}0]$ on the basis of the single particle energies or the peak energies of the excitonic spectra. In this case only the peak polarization delivers the information on the QD orientation.

In Fig. 3.14 interband and the CB intraband spectra are shown for two QDs, which have same shape but are aligned along different directions. Their lateral aspect ratios are $\text{ar}_L = 5/7$ and $\text{ar}_L = 7/5$, respectively. Linear and quadratic terms of the piezoelectric field are included in the calculation. The excitonic absorption spectra differ in their peak positions, their intensity, and, in particular, in their polarization degree. The polarization is even more pronounced in the intraband transition spectra: For a QD elongated along $[1\bar{1}0]$

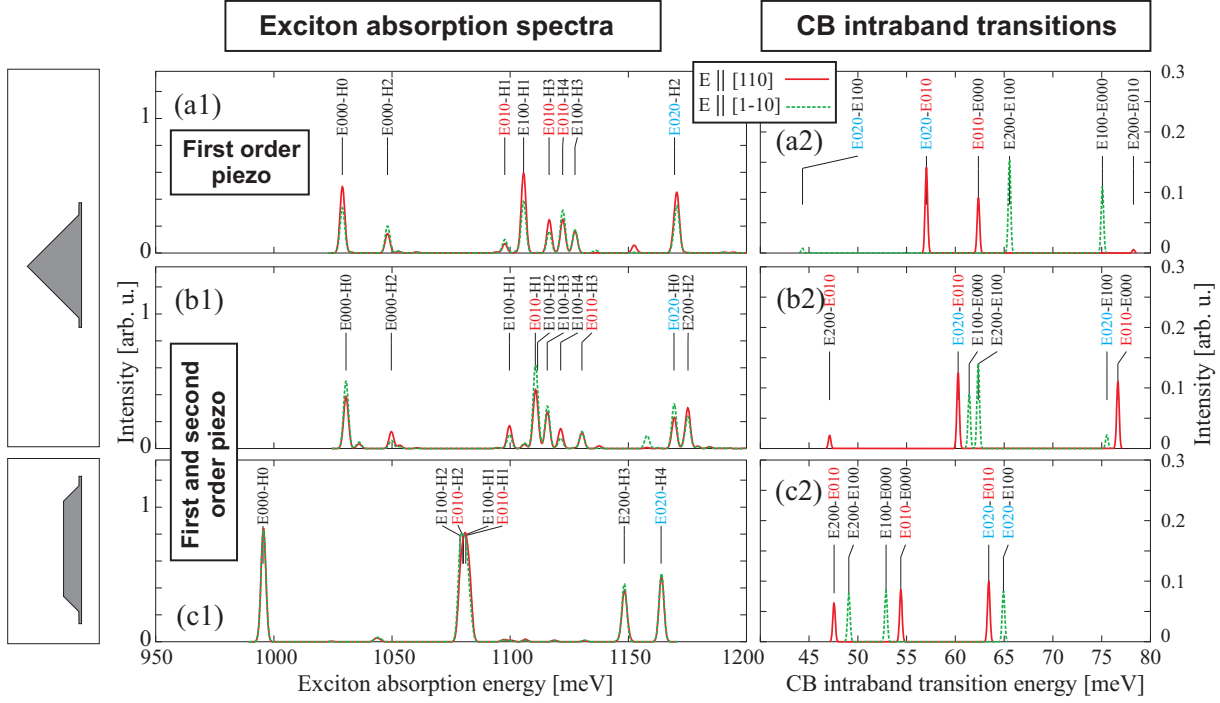


FIGURE 3.13. Excitonic absorption spectra (left panel) and CB intraband transition spectra (right panel) shown for a full InAs pyramid and a flat truncated pyramid both taken from series *B*. In (a) and (b) the results are contrasted for the two approaches for calculating the piezoelectric field.

($a_{RL}=5/7$) only those lines are visible in the considered energy range, that are polarized in $[1\bar{1}0]$ direction. The piezoelectric effect and the elongation sum up with respect to their impact on the p -state splitting. For the other case, a QD elongated along $[110]$, the piezoelectric effects and the elongation are compensating each other to a large degree and, as a result, the transitions $E100-E000$ and $E010-E000$ are very close in energy. Hence, the two orientations are clearly distinguishable by energy and polarization of their intraband spectra.

3.4. Varying composition profiles

3.4.1. Inverted cone like composition profile. The experiments of Fry *et al.*[68], employing Stark effect spectroscopy, have shown that, for certain QDs, the hole groundstate is localized towards the top of the dot, slightly above the electron. O'Reilly *et al.*[69] have conjectured that this observation can be attributed to an InAs gradient towards the upper part of the QD. Later on, Sabathil *et al.*[70] studied the impact of different composition profiles on the behavior of the electron-hole dipol in presence of a lateral electric field.

These investigations were accompanied by structural investigations using X-TEM[71] and X-STM[64, 72], guiding us to the choice of the composition profile of series *F*, which will be discussed in this paragraph.

In order to identify the consequences of the inhomogeneous composition profile like of series *F*, we compare the flattest QD of this series ($a_v = 0.2$) (further referred to as $QD_{F-inhom}^{0.2}$) to the pure InAs lens-shaped QD from series *C* with the same vertical aspect ratio (further referred to as $QD_{C-hom}^{0.2}$). Both QDs contain the same integral amount of In. Compared to the archetype pyramidal QD, the electron-hole alignment of $QD_{F-inhom}^{0.2}$ is indeed reversed and their barycenters are separated by 0.2 nm. We would like to point out that this separation is very sensitive to the choice of the VB-deformation potential parameter a_v . Literature values of a_v scatter remarkably between $a_v = 1\text{ eV}$ and $a_v = -1\text{ eV}$ (see Vurgaftman *et al.*[73]).

Comparison of single particle energies (Figs. 3.6 and 3.10) and absorption spectra (Fig. 3.16) of $QD_{C-hom}^{0.2}$ and $QD_{F-inhom}^{0.2}$ yields the following results:

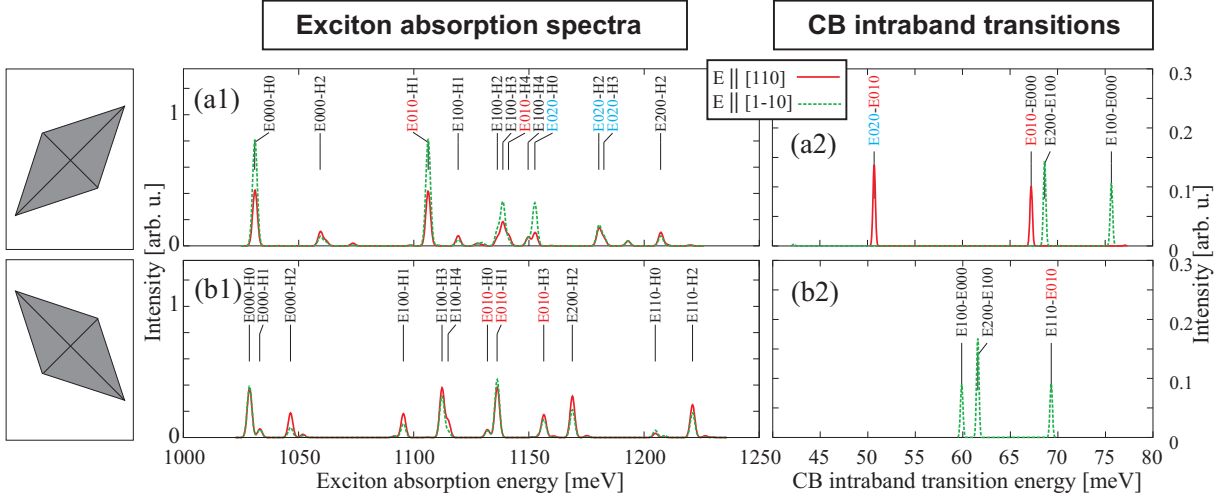


FIGURE 3.14. Excitonic absorption spectra (left panel) and CB intraband transition spectra (right panel) shown for parallelepipedal elongated QDs from series *D* having different lateral orientations with ($\text{ar}_L = 5/7$) and ($\text{ar}_L = 7/5$) respectively. First and second order piezoelectric effects are included.

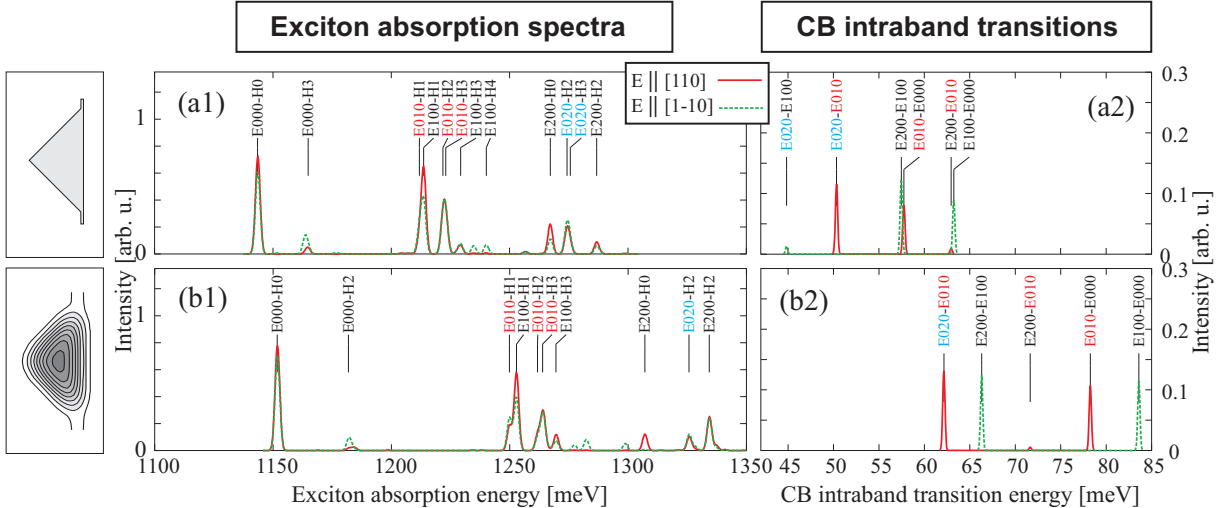


FIGURE 3.15. Excitonic absorption spectra (left panel) and CB intraband transition spectra (right panel) shown for the unannealed and the strongest annealed QD of series *G*. First and second order piezoelectric effects are included.

- (i) The electron and hole groundstate energies are shifted by 70 and 80 meV to higher energies for QD_{F-inhom}^{0.2}, resulting in a 150 meV larger groundstate exciton absorption energy.
- (ii) The peak order in the excitonic absorption spectra remains unchanged (Fig. 3.16 left panel).
- (iii) The electron *s-p* sublevel spacing remains the same, other than the *p-d* sublevel spacing. As a result, the $E_{010} - E_{000}$ intraband transition appears at almost the same energy, but the *d-p* transitions of QD_{F-inhom}^{0.2} are shifted to lower energies (Fig. 3.16 right panel).

3.4.2. Annealed QDs. In series *G* we simulate the effect of annealing on the electronic properties using a pyramidal QD, with a base length of 17.2 nm as model structure. We find the following peculiarities as result of the annealing procedure:

- (i) The electron and hole groundstate energies shift by 50 and 70 meV to higher energies, resulting in a blue-shift of the exciton groundstate absorption energy of ca. 120 meV [see Figs. 3.11 and 3.15 (b1)].

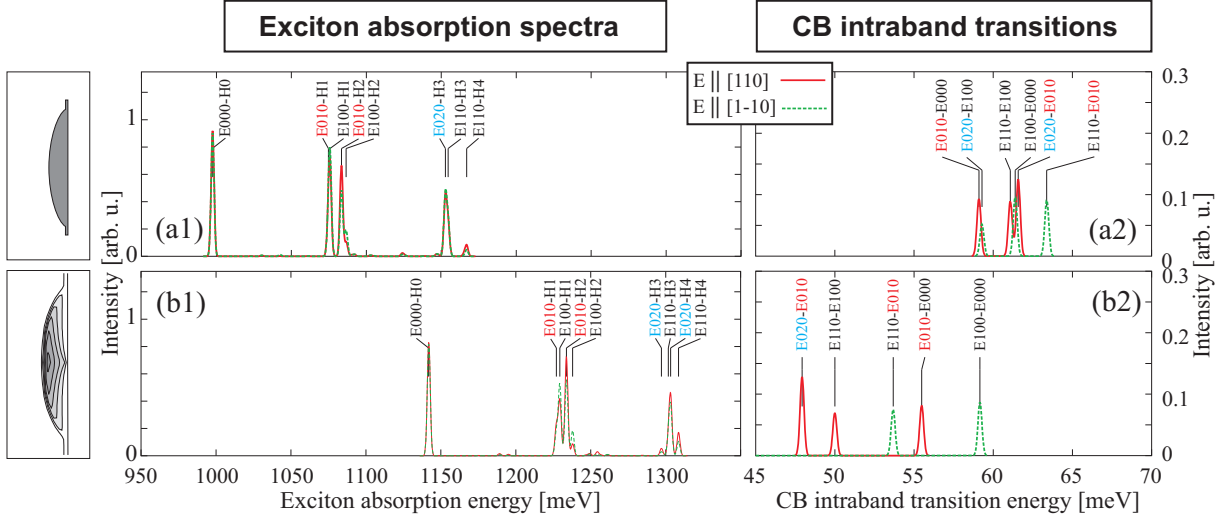


FIGURE 3.16. Excitonic absorption spectra (left panel) and CB intraband transition spectra (right panel) shown for two QDs having a circular base. The first one is taken from series *C* and the other from series *F*, both having the same total amount of InAs inside the QD structure and a similar vertical aspect ratio of $\text{ar}_V = 0.21$ (a) and $\text{ar}_V = 0.2$ (b) respectively. First and second order piezoelectric effects are taken into account.

(ii) The *s-p* level spacing and the hole sublevel spacing increases, resulting in a larger separation of the *s*-channel from the *p*-channel transitions. This finding is surprising at first sight, since high excitation PL results for annealed QD ensembles reveal a reduced *s-p* channel spacing.[74] These experiments, however, were performed in an energy range closer to the GaAs bandgap. In this energy range the excited states start to delocalize resulting in a decreasing electron *s-p* splitting.

(iii) Due to the increasing *s-p* level spacing, the intraband transition shift to higher energies [Fig. 3.15 (b2)].

3.4.3. InGaAs QDs with uniform composition. The choice of the average $\text{In}_x\text{Ga}_{1-x}\text{As}$ composition of QDs is often employed to taylor the emission wavelength. The impact of the Ga content ($1 - x$) on the electronic properties is investigated using series *E*. From Figs. 3.9 and 3.15 we can derive the following properties:

(i) An increase of the Ga content by 30 % shifts the electron and hole groundstate by 55 meV each to higher energies, resulting in a blue-shift of the exciton groundstate absorption energy of ca 110 meV [Fig. 3.15 (a1)].

(ii) In contrast to our findings for the annealing series *G*, the separation of the *s*- and *p*-shell electrons decreases. Hence, by comparing Figs. 3.15 (a1) and (b1), we find the *p*-channel transitions much closer to the *s*-channel transitions than in series *G*. The resulting intraband transitions are shifted to lower energies [Fig. 3.15 (a2)].

3.5. Conclusions

We investigated in a systematic way the correlation between structural QD properties like size, shape and composition and their electronic and optical properties.

(i) We compared the electronic properties of round and square based InAs/GaAs QDs with constant volume but varying aspect ratios. We found a large redistribution of strain from dominant hydrostatic, if the aspect ratio is 0.5 (full pyramid and half sphere, respectively), to pronounced biaxial for flat dots. The reduced average energy gap results in an increasing electron and hole localization, a finding that is more prominent for QDs having a circular base. When the QD height becomes smaller, the HH-LH coupling decreases, since the shear strain components tend to disappear. As a result, the LH-percentage of the hole ground-states drops from around 10 % down to 2.8 %.

(ii) The transition energies of pure InAs QDs (series *C*) are smaller than those with Ga incorporation (series *F*), even if the integral amount of In is the same in both cases. QDs with nonuniform composition profiles (like series *F*) have larger transition energies.

(iii) We simulated the effect of annealing on a pyramidal QD. The electron and hole groundstate energies are shifted by 50 and 70 meV to higher energies resulting in a blue-shift of the exciton groundstate absorption energy of ca. 120 meV. The *s-p* level spacing and the hole sublevel spacing increase, resulting in a larger separation of the *s*-channel from the *p*-channel transitions. The corresponding electron and hole wavefunctions are stronger localized.

(iv) We compared the classical approach of calculating the piezoelectric field in QDs [2] to the one recently developed by Bester *et al.*[11, 42], which takes into account the second order piezoelectric field, for a wide range of different QD structures. We found the piezoelectric potential arising from the quadratic terms to be very sensitive to the base shape, the vertical aspect ratio, and the composition. Its orientation inside the QD is reversed compared to the first order potential and can surpass it resulting into a reversal of the electron *p*- and *d*-state ordering and a reorientation of the hole wavefunctions, as observed for InAs pyramidal QDs. In this case the quadratic terms exceed the linear contributions inside the QD. Upon gradual annealing of this QD, thus, introducing an isotropic composition gradient, the second order field decreases dramatically, leaving the first order contribution as the dominant part. As a result, the electron *p*- and *d*-state order and the hole wavefunction orientations change. The same is observed for a pyramid with increasing, homogeneously inserted, Ga content.

(v) We calculated the excitonic absorption spectra and the CB-intraband transitions. The former are very sensitive to almost all applied structural changes and to the piezoelectric field, leading to strong modification of the *p*- and *d*-channel transitions. Upon changing the model for the piezoelectric field calculations, a peak reordering within these absorption channels can occur and the polarization anisotropy between $e \parallel [110]$ and $e \parallel [1\bar{1}0]$ can change. CB-intraband-transition spectra are strongly polarized either along [110] or [1 $\bar{1}$ 0] and very sensitive to changes of the piezoelectric field or any other anisotropy.

CHAPTER 4

Few-particle Energies versus Geometry and Composition

Large interest in quantum dots also persists due to their paradigm violating nature of many of the involved physical phenomena, such as the exciton fine-structure [4], the electron p -state splitting [3] or the shifts of the few-particle state recombinations of the biexciton (XX)[75–77], trions (X^\pm) [66, 78–80] or charged biexcitons (XX^\pm) relative to the exciton.[81–83] These physical quantities are sensitively affected by size, shape and composition of the QDs, via the inhomogeneous strain, the piezoelectric field and via the atomistic symmetry anisotropy (ASA).

In this chapter we present systematic calculations of the *many-particle* properties of several types of QDs, varying size, shape (square/circular/rhomboid base, different vertical/lateral aspect ratios) and composition (homogeneous/peaked and isotropic interdiffusion) (see Fig. 3.1). First and second order piezoelectric effects are taken into account.[11]

4.1. Interrelation of QD-structure, strain and piezoelectricity, and Coulomb interaction

4.1.1. The binding energies of the few particle complexes. The binding energies of excitons χ^q are defined as

$$\begin{aligned}
 \Delta(X^0) &= [\mathcal{E}_0^{(e)} - \mathcal{E}_0^{(h)}] - E^{(0)}(X^0) \\
 &= -J_{00}^{(eh)} - \delta_{\text{Corr}}(X^0), \\
 \Delta(X^+) &= [-\mathcal{E}_0^{(h)} + E^{(0)}(X^0)] - E^{(0)}(X^+) \\
 &= -J_{00}^{(eh)} - J_{00}^{(hh)} - \delta_{\text{Corr}}(X^0) - \delta_{\text{Corr}}(X^+), \\
 \Delta(X^-) &= [\mathcal{E}_0^{(e)} + E^{(0)}(X^0)] - E^{(0)}(X^-) \\
 &= -J_{00}^{(eh)} - J_{00}^{(ee)} - \delta_{\text{Corr}}(X^0) - \delta_{\text{Corr}}(X^-), \\
 \Delta(XX^0) &= 2E^{(0)}(X^0) - E^{(0)}(XX^0) \\
 &= -J_{00}^{(eh)} - J_{00}^{(ee)} - J_{00}^{(hh)} - 2\delta_{\text{Corr}}(X^0) - \delta_{\text{Corr}}(XX^0).
 \end{aligned} \tag{4.1}$$

$J_{00}^{(ij)}$ is the direct Coulomb integral between states Ψ_0^i and Ψ_0^j being either electron or hole ground state, $\mathcal{E}_0^{(e/h)}$ the respective single-particle energies, $\delta_{\text{Corr}}(\chi^q)$ the total energy correction due to correlation effects and $E^{(0)}(\chi^q)$ is the total energy of particle χ^q including all Coulomb effects. Fig. 4.1 depicts the relative importance of the direct Coulomb terms and correlation energies with respect to the binding energies $\Delta(\chi^q)$. Both contributions and their relation to the QD structure properties will be generally discussed now.

Direct Coulomb interaction. The direct Coulomb integrals $J_{00}^{(ij)}$ are calculated employing the Poisson approach:

$$\begin{aligned}
 J_{00}^{(ij)} &= q_i \int d\mathbf{r} |\Psi_0^i|^2 V_0^j, \\
 q_j |\Psi_0^j|^2 &= \epsilon_0 \nabla \cdot (\epsilon_s \nabla V_0^j).
 \end{aligned} \tag{4.2}$$

Image charge effects arising from the material dependent static dielectric constant are taken into account. The magnitude of J depends on the particle types, being either repulsive as for $J_{00}^{(ee)}$ and $J_{00}^{(hh)}$ or attractive like $J_{00}^{(eh)}$, on the spatial extent of the wavefunctions and, for $J_{00}^{(eh)}$, on the relative position of electron and hole orbitals. Four different cases with respect to size and position of electron and hole wavefunction can arise [Fig. 4.2 (a-d)].

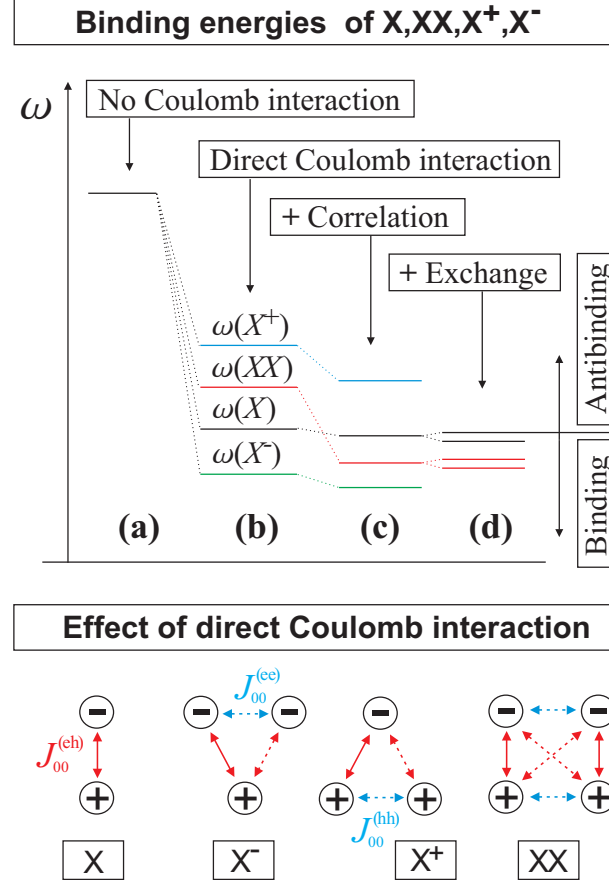


FIGURE 4.1. (Upper panel) The evolution of the multi-particle transition energies ω : (a) no Coulomb interaction is taken into account, the transition energies $\omega(\chi^q)$ are degenerate. (b) Coulomb interaction lifts the degeneracy of the transition energies. Four different combinations in the order of $\omega(\chi^q)$ can occur (see Fig. 4.2). (c) Adding correlation can produce a binding biexciton. In principle 24 different sequences of $\omega(\chi^q)$ are possible now. (d) Exchange splits the exciton ground state in two non-degenerate dark and two non-degenerate bright states. Since both bright states act as final states for the biexciton decay, $\omega(XX)$ is split as well. (Lower panel) Energetics of the direct Coulomb interaction of the four many-particle complexes. The appearance of the negative trion X^- -decay on the higher or lower energy side of the exciton line depends on the relative strength of the additional terms $J_{00}^{(ee)}$ and $J_{00}^{(hh)}$ (additional forces are marked as dashed arrows). If $J_{00}^{(ee)} > |J_{00}^{(hh)}|$ the X^- decay line appears on the high energy side of X , otherwise on the low energy side. The same rationale applies to the X^+ . For the biexciton XX decay the additional forces are not sufficient to create a binding biexciton, since always $J_{00}^{(ee)} + J_{00}^{(hh)} \geq 2|J_{00}^{(hh)}|$ holds.

(a) Electron and hole ground state wavefunction share the same barycenter, but the extent of the electron wavefunction is larger than that of the hole. This is generally considered the archetype situation for InAs/GaAs QDs, since the resulting order of our four excitonic complexes is thought to be the most typical case encountered in experiment, apart from the antibinding position of the biexciton XX , which results from the so far neglected correlation effect.

(b) A vertical electric field can pull electron and hole apart leading to the configuration displayed in Fig. 4.2 (b).

(c) Reversing the size of electron and hole wavefunction leads to the case considered in Fig. 4.2 (c). The resulting order $|J_{00}^{(eh)}| < J_{00}^{(hh)} < J_{00}^{(ee)}$ can also be a consequence of a large piezoelectric field inside the QD, as can be seen from Fig. 4.5 for large pyramidal QDs. The electron ground state wavefunction remains in the

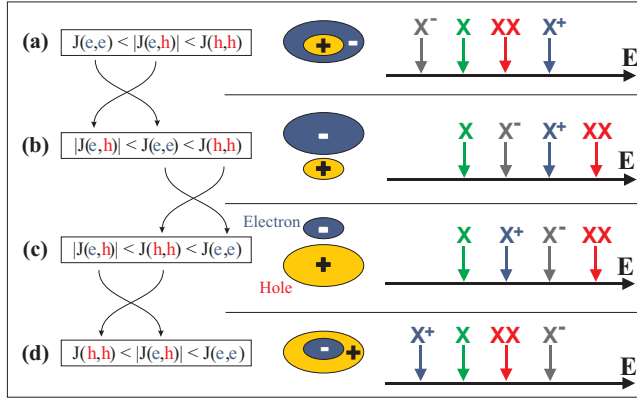


FIGURE 4.2. The recombination energy $\omega(\chi^q)$ of X , X^+ and X^- relative to the exciton X (spectroscopic shift), depends in first order on the Coulomb energies $J_{00}^{(eh)}$, $J_{00}^{(ee)}$ and $J_{00}^{(hh)}$. These quantities in turn depend on the electron and hole wavefunction size and their mutual position creating four different possibilities, labeled with (a) to (d).

QD-center whereas the hole wavefunction is driven into the two opposite QD-edges where the piezoelectric potential has its minimum. The resulting electron hole overlap decreases and, hence, $|J_{00}^{(eh)}|$ becomes smaller than $J_{00}^{(hh)}$ or $J_{00}^{(ee)}$.

(d) The last possible configuration is an electron and hole ground state sharing the same barycenter, but other than in case (a), the electron wavefunction extent is smaller than that of the hole state. Typically, QDs with a large vertical aspect ratio feature this type of configuration.

Neglecting correlation, these four cases lead to four different arrangements of the recombination energies $\omega(X)$, $\omega(XX)$, $\omega(X^+)$ and $\omega(X^-)$ as can be seen in Fig. 4.2 (right panel). $\omega(X)$ is defined as the recombination energy of the first exciton bright state and $\omega(XX)$ as the recombination into the first exciton bright state.

Correlation. The effect of correlation is more subtle. Within the Hartree-Fock approach, the antisymmetric wavefunction is approximated by a single Slater determinant. Exact wavefunctions, however, generally cannot be expressed as one single determinant. Hence, this approximation does not take into account Coulomb correlation, leading to an energy different from the exact solution of the few-particle Schrödinger equation. The difference between the Hartree-Fock limit and the exact energy is called the *correlation energy*.

As we will see in this work, the correlation energy is specific for each particle type and its magnitude can be very different for the various complexes χ^q . Hence, correlation may alter the order of the four transition energies, leading to 24 theoretically possible sequences (see Table 1). An important consequence is the appearance of binding biexcitons, which cannot be achieved by considering direct Coulomb effects alone. As we will see, the magnitude of the correlation is larger the more dissimilar electron and hole wavefunctions are, the larger their distance or the smaller their spatial overlap is. Further on, the correlation energies of the four complexes relative to each other depend on the spectral density of electron and hole states.

4.2. The Impact of QD size (series A and H)

To study the impact of the QD size we focus on series A and H (see Fig. 3.1). The pyramidal shape of the former series represents a model QD structure introduced by Grundmann *et al.*[2] The other series is closely modeled to reproduce the spectroscopic peculiarities observed by Heitz *et al.*[84] describing an onion-like size distribution. Both series together encompass an X^0 -energy range of 300 meV starting at 1.3 eV for the smallest QD of series H to as little as 1 eV for the largest full pyramid of series A.

Order of appearance				proximity to case (a),(b),(c),(d)	
1	2	3	4		Index
X^-	X	XX	X^+	(a)	0
X^-	XX	X	X^+	(a1)	1
X^-	X^+	XX	X	(a1)	2
XX	X	X^-	X^+	(a1)	3
X^-	X	X^+	XX	(a1) , (b1)	4
X	X^-	XX	X^+	(a1) , (b1)	5
X^-	XX	X^+	X	(a2) , (b2)	6
XX	X^-	X	X^+	(a2) , (b2)	7
X	XX	X^+	X^-	(b1)	8
XX	X^-	X^+	X	(b1)	9
X^+	X^-	X	XX	(b1)	10
X	X^-	X^+	XX	(b)	11
X	X^+	X^-	XX	(c)	12
X^-	X^+	X	XX	(c1)	13
X	XX	X^-	X^+	(c1)	14
XX	X^+	X^-	X	(c1)	15
X	X^+	XX	X^-	(c1) , (d1)	16
X^+	X	X^-	XX	(c1) , (d1)	17
XX	X^+	X	X^-	(c2) , (d2)	18
X^+	XX	X^-	X	(c2) , (d2)	19
XX	X	X^+	X^-	(d1)	20
X^+	X^-	XX	X	(d1)	21
X^+	XX	X	X^-	(d1)	22
X^+	X	XX	X^-	(d)	23

TABLE 1. The sequence of the X, XX, X^\pm peaks can be arranged in 24 different combinations. Four of them, denoted as (a, b, c, d), can form by taking the direct Coulomb interaction into account only. For the other 20 combinations it additionally requires correlation to establish. With proximity $\alpha i, \alpha \in \{a, b, c, d\}$, it is intended to describe how many transpositions i it requires to end up in one of the pure Coulomb cases a, b, c or d. The 24 cases are labeled with a unique index. The bold indices refer to the combinations we find in this work for our investigated structures.

Figure 4.3 shows the single particle energies of both series, Figs. 4.4 and 4.5 the shape of the ground state wavefunctions. Their position and spatial extent determine the direct Coulomb energies.

Series H: For the smallest QDs of series H we observe a larger spread of the electron orbital into the surrounding matrix as compared to that of the hole orbital, which is always strongly confined inside the QD. Consequently, the Coulomb repulsion between two electrons is much smaller than for two holes, occupying the ground state. Therefore, the negative trion is binding and the positive trion is antibinding (see Fig. 4.6). The biexciton is antibinding too, since

$$|J_{00}^{(eh)}| < (J_{00}^{(ee)} + J_{00}^{(hh)})/2$$

holds (in case of an equal sign, the biexciton transition would be degenerate with the exciton transition). The smaller the electron-hole size disparity is, the smaller are the binding energies. At a height of 11 ML, the correlation energy $\delta_{\text{Corr}}(XX)$ is large enough to create a binding biexciton, although $|\delta_{\text{Corr}}(XX)|$ is decreasing with increasing QD height. For the absolute values of the correlation energies we observe the

order

$$|\delta_{\text{Corr}}(X)| < |\delta_{\text{Corr}}(X^-)| < |\delta_{\text{Corr}}(XX)| < |\delta_{\text{Corr}}(X^+)| \quad .$$

The former two values are increasing and the latter two decreasing upon size increase, however, without changing their order.

Series A: The trend with respect of the relative electron-hole extent continues with series *A*. For the smallest pyramid of this series the direct Coulomb energies are equal with respect to their absolute value. Hence, the order of the recombination energies is determined by the correlation energies alone. Now we find a binding positive trion and an antibinding negative trion and the biexciton is also in a binding state.

The larger the pyramids of series *A* become, the larger becomes the hole wavefunction extent relative to the electron wavefunction, for two reasons. First, the biaxial strain and its sign change at the QD center enforces a hole position at the QD bottom. Second, since the lateral QD-extent is largest at the pyramid base the hole orbital can cover a comparatively large space, larger than the electron orbital can take. This results into a larger Coulomb energy between two electrons than for two holes occupying the ground state level. The absolute value of the electron hole Coulomb attraction $|J_{00}^{(eh)}|$ is even smaller than $J_{00}^{(ee)}$ and $J_{00}^{(hh)}$, which results from the piezoelectric field, as will be shown in the next section.

For the correlation energies we observe

$$|\delta_{\text{Corr}}(X)| < |\delta_{\text{Corr}}(X^-)| < |\delta_{\text{Corr}}(XX)| \approx |\delta_{\text{Corr}}(X^+)| \quad .$$

The last two quantities exhibit an enormous increase upon increasing pyramid size.

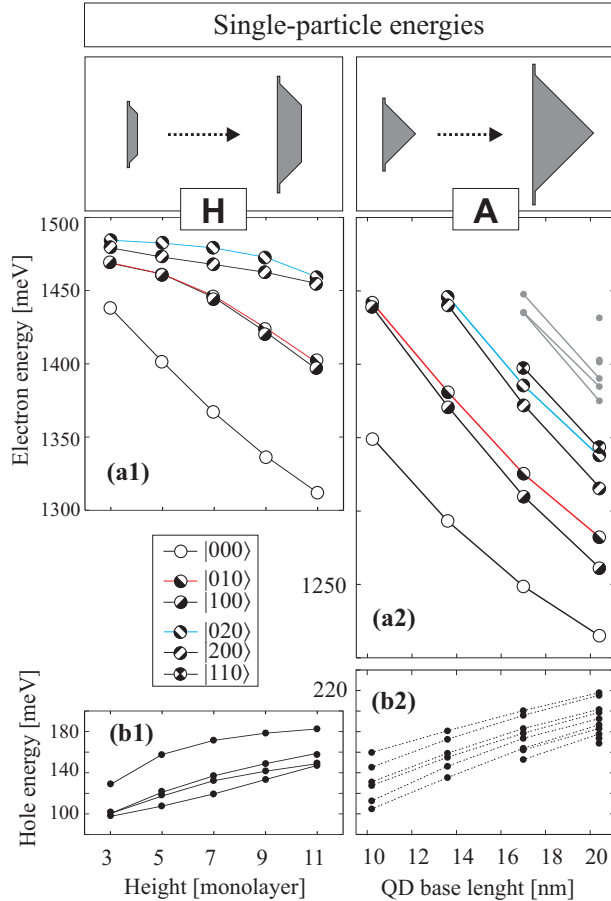


FIGURE 4.3. Single particle electron and hole energies shown for series *H* and *A*.

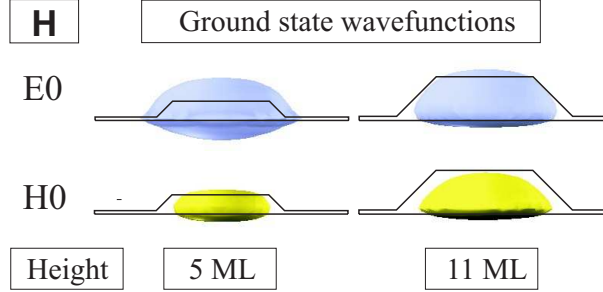


FIGURE 4.4. Probability density at 65% of electron and hole ground state wavefunctions for QDs of series *H* having a height of 5ML and 11ML respectively.

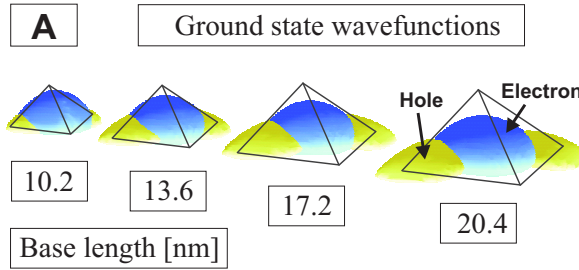


FIGURE 4.5. Probability density at 65 % of electron and hole ground state wavefunctions for pyramidal QDs of series *A*. Due to the increase of the piezoelectric field with larger QD size the hole wavefunction (yellow) tends to elongate along $[1\bar{1}0]$. As a result the electron hole overlap decreases and $|J_{00}^{(eh)}|$ becomes smaller than $J_{00}^{(hh)}$ and $J_{00}^{(ee)}$.

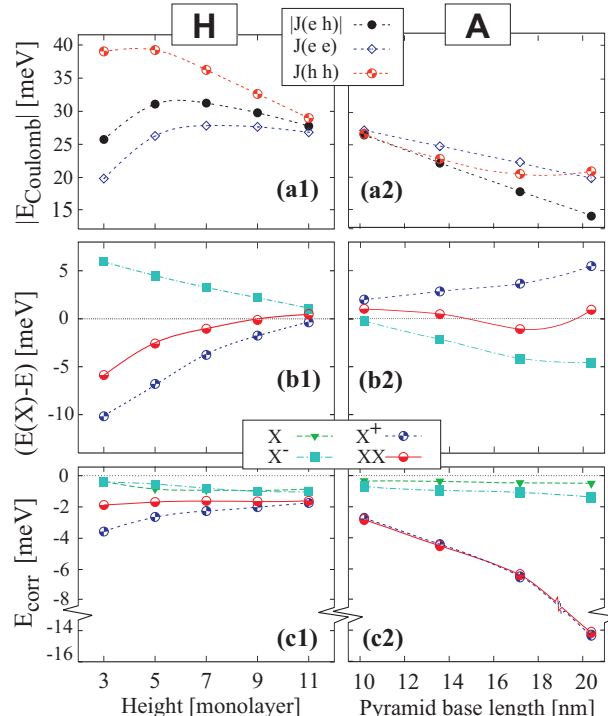


FIGURE 4.6. (a) The direct Coulomb energies $J_{00}^{(ee)}$, $J_{00}^{(hh)}$ and $J_{00}^{(eh)}$, (b) the difference of the binding energies with respect to the exciton energy, calculated for a configuration (10e,10h), and (c) the correlation energies $\delta_{\text{Corr}}(\chi^q)$ are shown for series *A* and *H*. First and second order piezoelectric effects are included.

	Coulomb energies [meV]			Correlation energies [meV]		Binding energies [meV]		
	$J_{00}^{(eh)}$	$J_{00}^{(ee)}$	$J_{00}^{(hh)}$	$\delta_{\text{Corr}}(XX)$	$\delta_{\text{Corr}}(X^+)$	ΔE_{XX}	ΔE_{X^+}	ΔE_{X^-}
(a) no piezo	-19.0	22.8	17.7	-3.4	-3.4	-1.3	4.0	-3.9
(b) with piezo	-17.5	22.5	20.5	-6.4	-6.6	-0.4	3.5	-3.1

TABLE 2. Direct Coulomb energies, Correlation and Binding energies for a (full) pyramidal QD (base length 17.2 nm) in absence (a) and presence (b) of the piezoelectric field. For the latter, first and second order components are taken into account.

4.2.1. The role of the piezoelectric field. In Sec. 4.1.1 it was demonstrated that the relative size and position of electron and hole wavefunctions is decisive for the XX , X^+ and X^- binding energies. From our previous work [2, 85] we know that the piezoelectric field strongly affects the order and the orientation of the single particle orbitals and it leads to a spatial separation of electron and hole wavefunction (see Fig. 4.5) for series A. As a result, the electron-hole overlap and, hence, their Coulomb attraction decreases and $|J_{00}^{(eh)}|$ can become smaller than $J_{00}^{(ee)}$ and $J_{00}^{(hh)}$ (see e.g. Table 2). Consequently, according to Fig. 4.2, the XX , X^+ and X^- recombination peaks are blue-shifted relative to the exciton line X , as a result of the piezoelectric effect. By taking into account correlation, the picture changes and in most cases we encounter at least a binding positive trion X^+ and sometimes also a binding biexciton XX .

A strong piezoelectric field has a large impact on the shape and orientation of the hole wavefunctions, especially for the ground state $|h_0\rangle$. In contrast to the electron ground state $|e_0\rangle$, $|h_0\rangle$ is strongly elongated and distorted in the direction of the piezoelectric potential minima. The maximum of the probability density of $|h_0\rangle$ resides not in the dot center anymore, but is shifted to the corners where the piezoelectric potential has its minimum. Since the probability density is rising thereby, the Coulomb repulsion between two holes $J_{00}^{(hh)}$ occupying the ground state is increased. This result is displayed in table 2, where we assess the change of Coulomb and correlation energies for the full pyramid with 17.2 nm base length upon introduction of a piezoelectric field: $|J_{00}^{(eh)}|$ decreases by 1.5 meV and $J_{00}^{(hh)}$ increases by 2.8 meV.

Still the repulsion between two holes remains smaller than for two electrons, $J_{00}^{(hh)} < J_{00}^{(ee)}$, which is a peculiarity of the pyramidal shape, where the special strain conditions force the hole ground state to be located at the QD bottom. Therefore the resulting sequence of Coulomb energies changes from case (d) in Fig. 4.2 to case (c), along with a crossing of the X^+ from binding to antibinding. However, if correlation is added to the calculations, X^+ becomes binding again, due to the comparatively large $\delta_{\text{Corr}}(X^+)$.

4.3. The aspect ratio

4.3.1. Vertical aspect ratio (series B, C and F).

Different types of charge separation effects: From Fig. 4.7 two regimes for series B can be identified in terms of the relative Coulomb binding energies binding energies [Fig. 4.7 (a)] and the resulting relative binding energies Fig. 4.7 (b): The first one holds for $\text{ary} < 0.2$ and can be described as the unequal vertical wavefunction spread-out of electron and hole ground state. Since both share the same barycenter and, apart from their size, have a similar shape, we encounter case (a) of Fig. 4.2 with the same order of X^+ , XX and X^- . The only difference to Fig. 4.2 (a) is their relative position compared to the exciton, which is changed due to correlation. In this range of ary , the very strong z-confinement leads to a wavefunction spill-over of electron and hole state, visible through the decreasing Coulomb energies upon smaller aspect ratio.

The other regime – Stier *et al.*[86] coined the term piezoelectric regime – holds for $\text{ary} > 0.2$. It is characterized by a larger hole wavefunction extent, due to the pyramidal shape (see Sec. 4.2), and a reduced electron hole overlap as a result of a larger piezoelectric field. Hence, the Coulomb attraction of electron and hole $|J_{00}^{(eh)}|$ becomes smaller than $J_{00}^{(ee)}$ or $J_{00}^{(hh)}$.

Series C and F exhibit a similar behavior in terms of the peak order, although the piezoelectricity plays only a minor role in these structures (see [42, 85]), which becomes visible through the relatively larger electron hole attraction, $|J_{00}^{(eh)}| > J_{00}^{(hh)}$ (except for the half-sphere in series C).

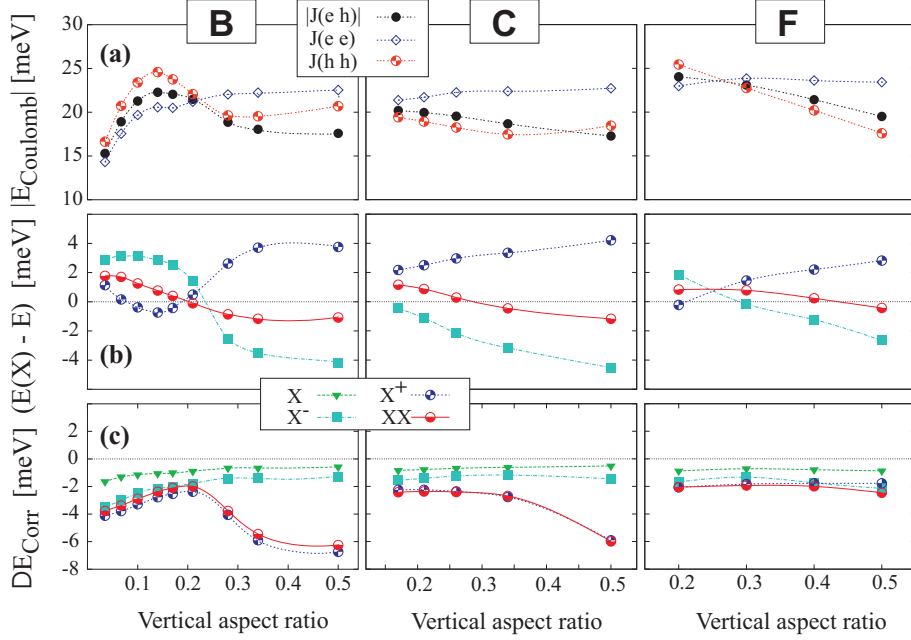


FIGURE 4.7. (a) the direct Coulomb energies $J_{00}^{(ee)}$, $J_{00}^{(hh)}$ and $J_{00}^{(eh)}$, (b) the spectroscopic shifts, calculated for a configuration (10e,10h), and (c) and the degree of correlation shown for series *B*, *C* and *F*. First and second order piezoelectric effects are included.

The charge separation in series *F* is induced by the trumpet-shape composition profile forcing the hole ground state to be located above the electron ground state. Since the In core extends towards the tip, the hole state can expand in lateral direction more efficiently than the electron. Hence, as in the case of the full pyramid, we find for $\text{ar}_V > 0.2$: $J_{00}^{(ee)} > J_{00}^{(hh)}$.

The biexciton binding energy : For all three series *B*, *C* and *F*, where the vertical aspect ratio is the variation parameter, the biexciton changes from antibinding ($\text{ar}_V = 0.5$) to binding for smaller aspect ratio. The cross-over point is different in each series, but the spectroscopic shift is monotonically decreasing with increasing ar_V in all three series.

Correlation: Within our three series *B*, *C* and *F* we again observe that the correlation energies of biexciton and positive trion increase drastically when the attractive Coulomb force $|J_{00}^{(eh)}|$ becomes smaller than the repulsive terms $J_{00}^{(ee)}$ and $J_{00}^{(hh)}$ respectively.

4.3.2. Lateral aspect ratio (series D). A QD elongation away from the square basis is often discussed as a possible source of the fine-structure splitting, since it introduces a symmetry reduction from C_{4v} to C_{2v} already on the level of the QD structure. However, as long as no piezoelectricity is included (or/and the ASA in the case of atomistic models), there is no distinction possible for the single particle energies or the peak energies of the excitonic spectra between the two possible elongations [110] and [1\$\overline{1}\$0]. In this case only the polarization delivers the information on the QD orientation. Even more, there is no change of the direct Coulomb energies J and the corresponding few-particle binding energies visible throughout series *D*, as can be seen in the left panels of Fig. 4.8.

The situation changes when piezoelectricity is taken into account. (i) First, the electron-hole attraction $J_{00}^{(eh)}$ becomes smaller than the repulsive terms $J_{00}^{(ee)}$ and $J_{00}^{(hh)}$. (ii) Second, the direct Coulomb energies and the resulting binding energies of XX , X^+ and X^- are different for both directions (see Fig. 4.8(a) and (b)). The order of the excitonic complexes, however, remains unchanged. (iii) The degree of correlation for the biexciton and the positive trion becomes largest for a large elongation along [110], where the attractive electron-hole Coulomb forces reach their minimum and the repulsive Coulomb forces their maximum.

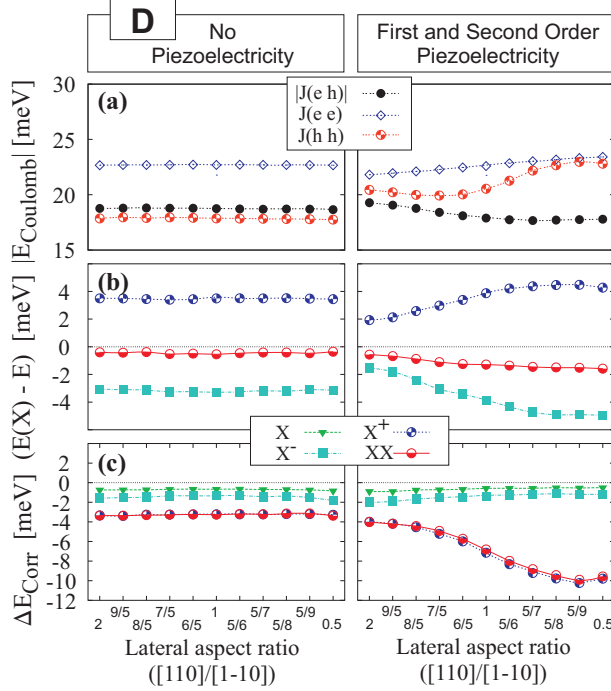


FIGURE 4.8. (a) The Coulomb energies $J_{00}^{(ee)}$, $J_{00}^{(hh)}$ and $J_{00}^{(eh)}$, (b) the spectroscopic shifts, calculated for a configuration (10e,10h), and (c) the degree of correlation shown for series of elongated QDs (*D*) in the cases of excluded piezoelectric field (left panel), and if first and second order effects are taken into account (right panel).

There is no experimental evidence from HRTEM etc. for such asymmetry. (iv) Without correlation we observe a complete different order of the excitonic complexes namely (X, X^+, X^-, XX) from lower to higher transition energies.

4.4. Different composition profiles

4.4.1. Inverted cone like composition profile. In order to identify the consequences of an inhomogeneous composition profile like in series *F*, we compare the flattest QD of this series ($\text{ary} = 0.2$) (further referred to as $\text{QD}_{\text{F-inhom}}^{0.2}$) to the pure InAs lens-shaped QD from series *C* having the same vertical aspect ratio (further referred to as $\text{QD}_{\text{C-hom}}^{0.2}$). Both QDs are designed to contain the same integral amount of InAs. Compared to the archetype pyramidal QD the electron hole alignment of $\text{QD}_{\text{F-inhom}}^{0.2}$ is reversed and their barycenters are 0.2 nm apart.

Prominent differences and similarities between $\text{QD}_{\text{C-hom}}^{0.2}$ and $\text{QD}_{\text{F-inhom}}^{0.2}$ are:

- (i) Both ground state wavefunctions (not shown here) of $\text{QD}_{\text{F-inhom}}^{0.2}$ are stronger localized than their $\text{QD}_{\text{C-hom}}^{0.2}$ counterparts, resulting in significant larger Coulomb energies $J_{00}^{(eh)}, J_{00}^{(ee)}$ and $J_{00}^{(hh)}$.
- (ii) In contrast to $\text{QD}_{\text{C-hom}}^{0.2}$, $J_{00}^{(hh)}$ is larger than $J_{00}^{(ee)}$ for $\text{QD}_{\text{F-inhom}}^{0.2}$, since the hole ground state is stronger localized than the electron ground state. Consequently we find a different pattern for the binding energies of XX, X^+ and X^- as can be seen from Fig. 4.7.

4.4.2. Annealed QDs. In series *G* we simulate the effect of annealing on the electronic properties for a pyramidal QD, originally having a base length of 17.2 nm. Prominent features are:

- (ii) Both ground state wavefunctions increase their localization resulting in larger Coulomb energies $J_{00}^{(eh)}, J_{00}^{(ee)}$ and $J_{00}^{(hh)}$.
- (ii) Due to the decreasing piezoelectric field upon annealing, $|J_{00}^{(eh)}|$ becomes larger than $J_{00}^{(hh)}$ with the first annealing step. Therefore the biexciton can change its sign and become binding.

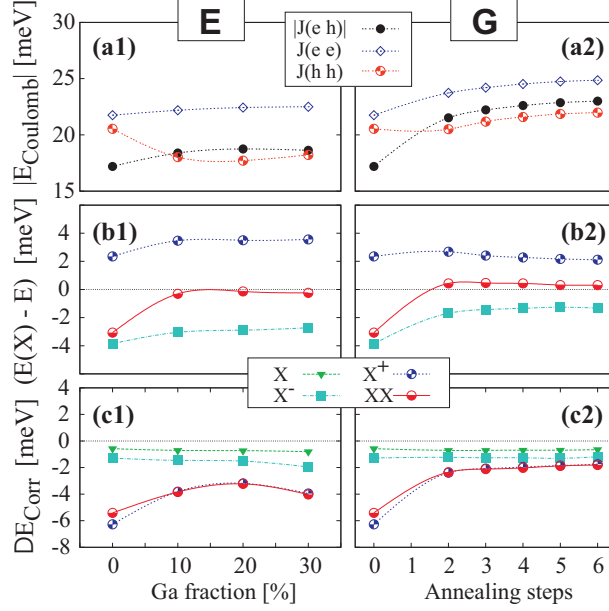


FIGURE 4.9. (a) the direct Coulomb energies $J_{00}^{(ee)}$, $J_{00}^{(hh)}$ and $J_{00}^{(eh)}$, (b) the spectroscopic shifts, calculated for a configuration (10e, 10h), and (c) and the degree of correlation shown for series E and G . First and second order piezoelectric effects are included.

(iii) We again observe a dramatic drop of the XX and X^+ correlation energies when $|J_{00}^{(eh)}|$ becomes larger than $|J_{00}^{(hh)}|$.

4.4.3. InGaAs QDs with uniform composition. A variation of the average $\text{In}_x\text{Ga}_{1-x}\text{As}$ composition of QDs is typically employed to tailor the emission wavelength. The impact of the Ga content ($1-x$) on the multi-particle electronic properties is investigated using series E . From our earlier work [85] we know that with increasing Ga content inside the QD the second order piezoelectric effect, which dominates for 100 % InAs, is reduced. Since the first order terms remains unaffected we encounter a sign change of the total piezoelectric field.

The presence of piezoelectricity constrains the wavefunction to a smaller volume leading to an increase of $|J_{00}^{(hh)}|$. Therefore, we find the smallest value of $|J_{00}^{(hh)}|$ for a Ga content of 15 % (see Fig. 4.9) where the QD interior is virtually piezoelectric field-free. As a result, a non-monotonic behavior of biexciton binding energy is observed.

The correlation energies of XX and X^+ exhibit this non-monotonic behavior too, which is related to the characteristics of $|J_{00}^{(eh)}| - |J_{00}^{(hh)}|$ turning from negative to positive values first and then to almost zero.

4.5. Correlation vs. QD size, shape and particle type

Correlation is an effect that seeks to minimize the total energy in the trade off between the kinetic energy of the involved single particle states and their mutual Coulomb attraction or repulsion. From the Figs. 4.6, 4.7, 4.8, and 4.9(c) it can be seen, that the magnitude of the energy correction due to correlation is specific for each particle type and foremost dependent on the QDs size and shape. This is especially obvious in series A (see Fig. 4.6), where $|\delta_{\text{Corr}}(XX)| \approx |\delta_{\text{Corr}}(X^+)| > |\delta_{\text{Corr}}(X^-)| > |\delta_{\text{Corr}}(X)|$ and all the correlation energies increase with increasing dot size.

In general, there are three main factors, which determine the degree of correlation:

(i) First, the absolute and relative size of electron and hole wavefunction and their mutual position, in other words, how much Coulomb energy can be gained (J_{eh}) or saved (J_{hh} , J_{ee}) by relocating to a more favorable place, changing shape or size. We observe, for instance, strong correlation effects for the positive trion and biexciton in the following cases:

(1) Electron and hole orbital size are very dissimilar like in series *H*, due to the asymmetric spread out of electron and hole wavefunction. (2) The barycenter of both carriers are at different vertical positions as in the case of the half sphere. We find a dipole of 1.5 nm resulting in a smaller Coulomb attraction between electron and hole $J_{00}^{(eh)}$ compared to $J_{00}^{(ee)}$ and $J_{00}^{(hh)}$ (Fig. 4.7(C)). (3) The largest correlation energies are observed for the largest full pyramid of series *A*. Electron and hole orbital are pulled into different direction due to strong piezoelectricity. Their spatial overlap reduces and $J_{00}^{(eh)}$ becomes smaller than $J_{00}^{(ee)}$ and $J_{00}^{(hh)}$. For this case we observe correlation energies of the order of 15 meV. This large value, however, is also related to the large wavefunction extent and the accompanying small kinetic energy. This will further detailed below in case (iii).

(ii) Second, the particle type. Here, the ratio of the number of Coulomb interactions within a particle type to the number of carriers within this complex is of importance. Since the CI method is a variational method, this ratio weights the importance of the Coulomb interaction relative to the kinetic energies of the single carriers. For the exciton this ratio is 1/2, one Coulomb integral compared to two carriers. For the biexciton we have the ratio 6/4, six Coulomb integrals and four particles. Therefore the relative importance of the Coulomb interaction is larger for the biexciton than for the exciton and, hence, more emphasis is put on minimizing the total Coulomb energy in the case of the biexciton, which is done by mixing higher excited state configurations into the CI ground state.

For both trions we encounter a ratio 3/3, three Coulomb integrals and three particles. Hence, this point cannot explain why the correlation energies are mostly very different for the positive and the negative trion, which will be explained by the next point.

(iii) Third, the sensitivity of the kinetic energy to small wavefunction size variations or equivalently the unequal density of the electron and hole spectrum. Both quantities are a function of the effective mass and the spatial wavefunction extent. A larger effective mass translates into a smaller kinetic energy and a smaller energetic separation of ground and excited states. A larger wavefunction extent in real space transforms in a smaller extent in k -space, hence, the kinetic-energy integral

$$E_{\text{kin}} \approx \int_{V_k} E(\mathbf{k}) \Psi(\mathbf{k}) d\mathbf{k},$$

becomes smaller too. Consequently, a variation δE_{kin} in response to a small wavefunction size variation $\delta\eta$ is larger, the steeper the dispersion $E(\mathbf{k})$ (as result of a smaller effective mass) and the smaller the wavefunction extent in real space is. In other words, δE_{kin} is large for small electrons and small for large hole orbitals. If δE_{kin} is small, the wavefunction can more easily reshape to save Coulomb energy. The 'reshaping' in our case is performed by mixing higher excited state configurations into the ground state configuration.

The importance of this point becomes visible by comparing $\delta_{\text{Corr}}(X^+)$ and $\delta_{\text{Corr}}(X^-)$: both complexes $X^+(h_0^2 e_0^1)$ and $X^-(h_0^1 e_0^2)$ share the same number of particles but in different configurations. Since the density of the hole spectrum is larger than that of the electron spectrum, the energy of those complexes, containing a larger number of positive carriers, is more affected by correlation. Therefore, $\delta_{\text{Corr}}(X^+) > \delta_{\text{Corr}}(X^-)$ holds. The more dense the spectrum becomes, the larger can be the correlation, as can be seen from the rising correlation energies of series *A* with increasing size in Fig. 4.6 (the corresponding spectral density can be derived from Fig. 4.3).

Another striking example is series *B*: here the absolute *and* the relative spectral densities change with the aspect ratio. For the pyramid ($\text{ary} = 0.5$) again we observe a large spectral hole density and small electron density. The electron density (see Ref. [85]) becomes larger with smaller aspect ratio resulting in a rising correlation energy of X and X^- . The hole density in contrast becomes smaller until $\text{ary} = 0.1$. Below that value the spectral hole density is rising again. This translates into a non-monotonic δ_{Corr} behavior of the particles containing 2 holes, the XX and the X^+ (see Fig. 4.7(c1)).

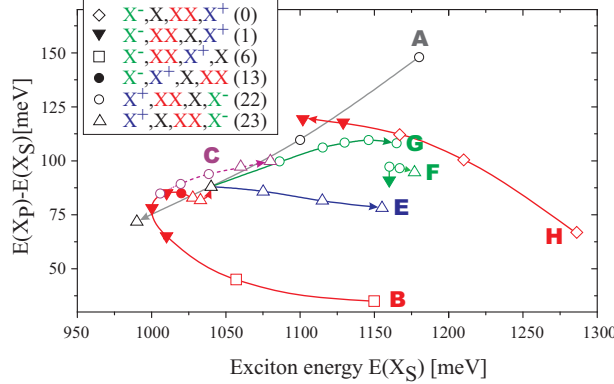


FIGURE 4.10. The difference ($E(X_P) - E(X_S)$) plotted versus $E(X_S)$. With $E(X_P)$ we denote the average value of the P -channel transitions, taken from the excitonic absorption spectra. The data are shown for the series A, B, C, E, F, G and H. The symbols are used to denote the order of the calculated few-particle energies X , XX and X^\pm . The small arrows indicate the order of structures within each series as shown in Fig. 3.1.

4.6. Conclusions

For a large number of QD structures, of varying size, shape and composition we investigated the relationship between the structural properties and the energies of a selected set of few-particle states (X , XX , X^\pm), which can be easily traced in experiment. The resulting binding energies turn out to be very sensitive to the various morphological peculiarities. We analyzed in detail the relationship between the QD geometry, the resulting shape and position of electron and hole wavefunctions, the direct Coulomb energies and changes introduced by correlation effects. The correlation effects are larger for biexciton and positive trion, which we attribute to the larger spectral density of the hole subsystem. This in turn is a result of the larger hole effective mass. In addition to that we found the correlation to be very sensitive to the relative size and position of the electron and hole ground state orbitals, which influences equally the direct Coulomb energies $J_{00}^{(e,h)}$, $J_{00}^{(e,e)}$ and $J_{00}^{(h,h)}$. Large correlation energies $\delta_{\text{Corr}}(XX)$ and $\delta_{\text{Corr}}(X^\pm)$ are observed in those cases, where the absolute value of the attractive Coulomb term $J_{00}^{(e,h)}$ falls below the values of the repulsive terms $J_{00}^{(e,e)}$ and $J_{00}^{(h,h)}$.

In Fig. 4.10 we compiled some of our data to visualize the wealth in the variation of the spectroscopic properties for different QD structures. We found the difference between the exciton s - and p -channel transitions as a function of the exciton energy (an easy observable quantity in experiment) an impressive fingerprint in order to distinguish between different types of InGaAs/GaAs QD structures. If, in addition, data on the spectroscopic shift of XX , X^\pm relative to X are available, we are quite confident that, by the spectroscopic signature alone, large parts of the QD morphology can be deduced. One example of this approach will be detailed in the next chapter.

CHAPTER 5

Multimodal QD-size distribution: Theory and Experiment

Comparing details of calculated and measured few-particle spectra of single quantum dots (QDs) is difficult due to the uncertainty about the actual structure and chemical composition of the probed QD [1]. Still the most advanced techniques able to yield information on an atomic scale on single QDs either provide a snapshot of the shape of an uncapped QD after cooling down the whole layer (STM [10, 87], AFM [88]) or just a cross section of the shape and arrangement of the QD of the various atoms at an unknown position (X-STM [9, 89]). Even if the complete three dimensional distribution of atoms in a QD could be assessed it could not be correlated in detail to its spectroscopic signature due to dot-to-dot shape, size and composition variations. This problem can be solved based on a radically different approach by exploiting the multimodal dot size distributions recently identified via photoluminescence spectroscopy (PL) of appropriately grown samples [84, 90]. Under special MOCVD growth conditions using Sb-surfactants the inhomogeneously broadened dot distribution decomposes into narrow multimodal distributions of dot sizes.

Low excitation PL leads to the identification of up to eight sub-ensembles each showing much reduced spectral width (~ 30 meV) as compared to the original ensemble. Detailed analysis of PL spectra and transmission electron microscopy (TEM) data demonstrate that (i) the QDs are relatively flat, (ii) the QDs have a well defined upper (001) interface and (iii) each peak represents a sub-ensemble of QDs sharing the same size and shape. With decreasing photon energy the size of each QD sub-ensemble increases by exactly one monolayer. Thus the QDs show an onion-like growth with an increasing height/base length aspect ratio with increasing QD size [84].

In this chapter it will be shown that, by using eight-band $\mathbf{k} \cdot \mathbf{p}$ calculations, excellent agreement to experimental results is obtained by assuming truncated pyramidal InAs/GaAs QDs. The calculations allow to identify in great detail the evolution of QD height and base length in monolayer steps from one sub-ensemble to the next [84].

Given this knowledge fundamental features of single and multiple excitons derived from single-dot spectra can be correlated to and derived from our detailed knowledge of the QD structure. These spectra, revealing essentials of few-particle effects, are obtained from cathodoluminescence measurements using near-field shadow masks [91].

It should be pointed out that due to fast deposition rate and the use of antimony as surfactant the structural and therefore optical properties of our MOCVD-grown samples are fairly different from typical MBE-grown In(Ga)As/GaAs-QDs. Hence it is of no surprise that the spectroscopic shifts observed in single-dot spectroscopy on MBE-grown QDs [92–98] are different from the values reported in this work.

TABLE 1. Available experimental results on the energy difference between exciton and the two different trions X^- , X^+ arranged according to the growth-method.

	QD-material	Growth-method	$X^0 - X^-$ [meV]	$X^0 - X^+$ [meV]
Refs. [92–98]	InGaAs	MBE	3.1 -5.8	-0.8 - -1.5
This work	InAs	MOCVD	8.0 -9.0	-2.0 --14.0

Typical data for negatively and positively charged trions are compiled in table 1 and compared to experimental data of Rodt *et. al.* [66]. The origin of the trion spectroscopic shifts are traced to an imbalance of the direct Coulomb terms $J_{00}^{(ee)}$, $J_{00}^{(eh)}$ and $J_{00}^{(hh)}$ [99] being related to a difference in the extension of the

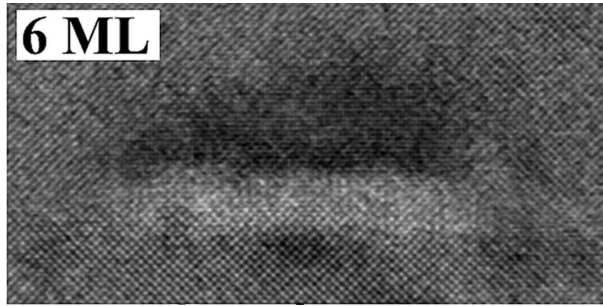


FIGURE 5.1. Typical cross section high resolution transmission electron micrograph of a InAs/GaAs quantum dot. Evaluation of the shape yields a truncated pyramid with a height of 6 monolayer.

ground state electron and hole wavefunctions. Hence, the much larger trion shifts in our case point at a larger difference of electron and hole localization in the MOCVD grown QDs.

Calculations using the configuration interaction method can account for exchange and correlation effects and are applied to yield detailed insight into the close interrelation between structural and few-particle properties.

5.1. Sample growth

The investigated samples were grown by metalorganic chemical vapor deposition (MOCVD) on GaAs(001) substrates. Trimethylindium, trimethylgallium, and tertiarybutylarsine were used as precursors. At 625°C a 300 nm thick GaAs buffer layer followed by a 60 nm Al_{0.6}Ga_{0.4}As diffusion barrier and 90 nm GaAs were grown. For the growth of the QD layers of type A the growth temperature was reduced to 485°C before depositing about 1.9 ML InAs followed by a 5 second growth interruption. Subsequently, the QDs were capped by 50 nm GaAs. The first 5 nm were grown at 485°C, then the temperature was ramped up to 600°C during growth. Finally, a 20 nm Al_{0.33}Ga_{0.67}As diffusion barrier and a 10 nm GaAs capping layer were deposited.

Triethylantimony was added for samples of type B during the deposition of the InAs layer and the growth interruption. Antimony is hardly incorporated due to its large size, but acts as surfactant modifying the evolution of the InAs QDs.[100, 101] Parts of a sample B were ex-situ annealed under an As-atmosphere.

Transmission electron microscopy investigations of such samples reveal a truncated pyramidal (see figure 5.1) shape of InAs/GaAs QDs with a density of about $\sim 4 * 10^{10} \text{ cm}^{-2}$.[101] A detailed study on structural properties dependent on varying growth conditions is performed in Ref. [102].

For photoluminescence (PL) and PL excitation (PLE) experiments the samples were mounted in a continuous-flow He cryostat, giving access to temperatures between 5 K and 315 K. A tungsten lamp dispersed by a 0.27 m double-grating monochromator served as low-density, tunable excitation source. The luminescence was spectrally dispersed by a 0.3 m double-grating monochromator and detected by a cooled Ge-diode using lock-in technique.

5.2. Determination of QD-morphology and the spectrum of excited states

The QD ensemble consists of up to eight sub-ensembles showing narrow spectral width of $\sim 30 \text{ meV}$ each (see Fig. 5.2). This splitting is attributed to a monolayer change of the QD-size from sub-ensemble to sub-ensemble [84] allowing to determine e.g. the QD-height of a given sub-ensemble just by counting the number of adjacent peaks.

Though both spectra show multimodal decomposition of the PL, the decomposition is particularly pronounced for sample B, showing eight peaks. The presence of antimony seems to have a large impact on the surface kinetics,[101] resulting in an enhanced PL modulation contrast and larger QDs, emitting at lower

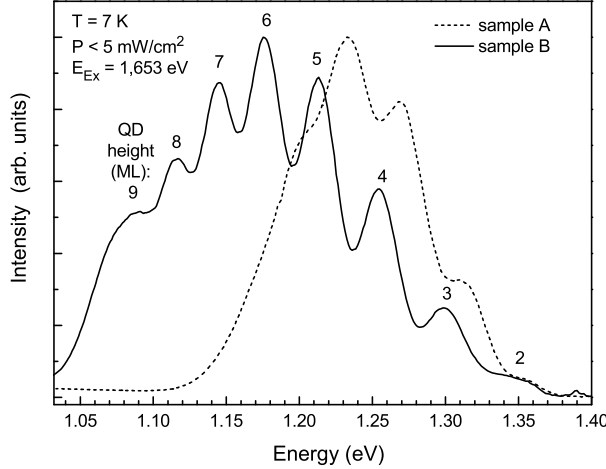


FIGURE 5.2. Photoluminescence spectra of samples A and B recorded at 7 K at an excitation density below 5 mWcm^{-2} .

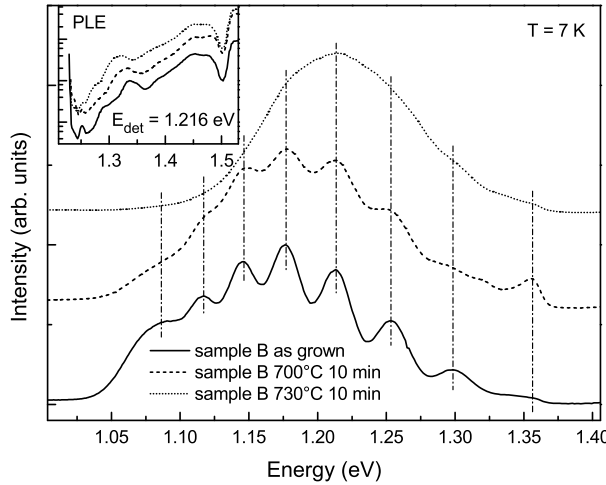


FIGURE 5.3. Normalized PL spectra of three pieces of sample B, which are as-grown or have been annealed for 10 min at 700°C and 730°C , respectively. The inset shows corresponding PLE spectra detected at 1.185 eV .

energies. Additionally, the individual sub-ensemble peaks are shifted by $\sim 15\text{ meV}$ to lower energies. In the following we will concentrate on B-type samples.

The explanation is related to a heterogeneous distribution of structural properties of the QDs. For the investigated InAs/GaAs QDs we resolve up to eight clearly distinguished peaks, which indicates that the very large overall inhomogeneous broadening ($> 200\text{ meV}$) is dominated by a discrete, step-like variation in the morphology of the QDs. We suggest that the discrete jumps are caused, in a first approximation, by a variation of the QD height in monolayer steps. It might be expected that ML-steps shift the whole eigenspectrum of the QDs and that the magnitude of the shift decreases with increasing height, being in qualitative agreement with the optical results (Fig. 5.2). Obviously, successive peaks correspond to the addition of a single ML to the height. The absolute thickness is not self-evident. We assume that the peak at 1.36 eV corresponds to a height of 2 ML. [103–105] The peaks in Fig. 5.2 are labeled according to the estimated height of the QDs.

From the fact that monolayer steps in the QD height cause a clearly resolved multimodal appearance of the inhomogeneously broadened PL some conclusions can be unambiguously drawn. The QDs must have a flat truncated shape with well-defined upper (001) interfaces. Indeed, QDs with such interfaces have been observed in XSTM of similarly grown QDs.[9] Spectral broadening caused by variations of the base length,

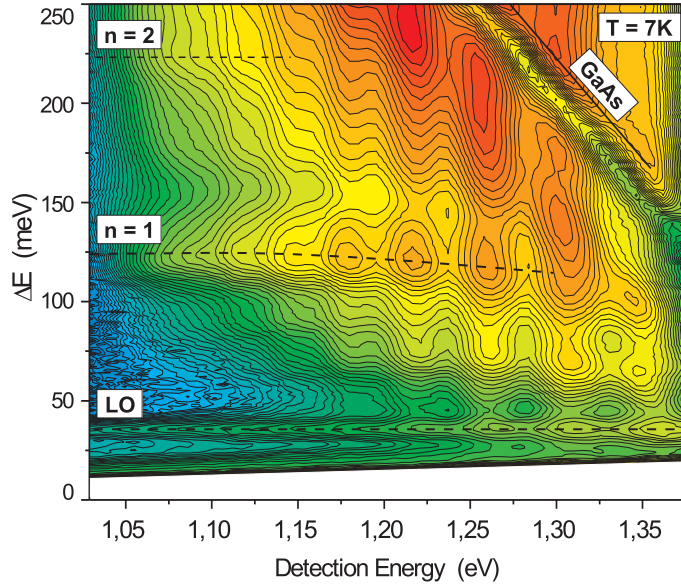


FIGURE 5.4. Contour plot of the PL intensity in dependence on the detection and excess excitation (i.e., relaxation) energies. The plot was generated from a series of PLE spectra and the intensity is given on a logarithmic scale.

the interface roughness, or composition fluctuations must be smaller than the energy shift caused by the addition of one monolayer to the height.

The existence of well-defined upper interfaces suggests In/Ga interdiffusion as negligible. Indeed, the observation of a large sub-state splitting of ~ 120 meV shown in Fig. 5.4 supports strongly the assumption of small InAs QDs. Ex-situ annealing experiments, degrading the definition of the interfaces by In/Ga interdiffusion, demonstrate the crucial role of the interfaces of the QDs. Figure 5.3 compares normalized PL spectra of as-grown and two annealed samples (10 min at 700°C and 730°C, respectively). The decreasing contrast of the modulation with increasing annealing temperature is due to the degradation of the interfaces by In/Ga interdiffusion. The PL shows no influence of the annealing on the PL peak positions. PLE spectra, however, recorded at a given ground state transition energy, see inset of Fig. 5.3, show a slight reduction of the sub-state splitting upon annealing, resulting either from an increasing effective size of the QDs or an increasing Ga concentration within the QDs.

Information on exciton localization and lateral confinement is obtained from PLE spectra.

Figure 5.4 depicts a contour plot of the PL intensity as a function of the detection and excess excitation energies. The intensity is given on a logarithmic scale. The plot was generated from a series of PLE spectra. The y-axis presents the energy difference between excitation and detection energy. Modulation upon resonant excitation is clearly resolved, e.g., in the $n=1$ state at ~ 120 meV, proving unambiguously a multimodal distribution of the QD ground state transition as origin of the observed modulation of the PL intensity. The spectra have a common excitation resonance at ~ 1.45 eV, which is attributed to absorption in the wetting layer. Thus, all QDs are surrounded by a one ML thick wetting layer, which limits exciton localization in the QDs. The exciton localization increases from ~ 100 meV for QDs with a height of 2 ML to ~ 360 meV for QDs with a height of 9 ML.

With increasing exciton localization energy the number of excited exciton states increases. Especially the large separation of the $n=1$ resonance, appearing ~ 120 meV above the ground state, provides additional guidance in view of internal QD-composition and QD-size. This peak originates from an excited exciton, composed of the first excited electron and hole state.[2, 106] The large splitting to the ground state transition, which mainly results from the large ground to first excited electron splitting, again is a result of pure InAs QDs with a rather small lateral extension. The apparent decrease of the quantization for the flattest QDs of 3 ML and 2 ML height is attributed to a delocalization of the excited state into the wetting layer.

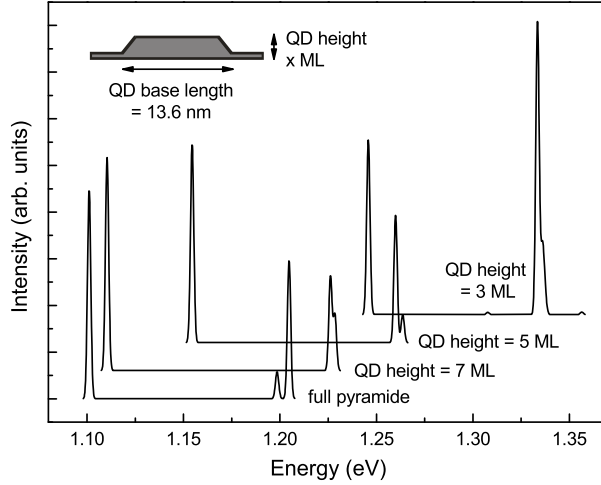


FIGURE 5.5. Absorption spectra calculated in an eight-band $\mathbf{k}\cdot\mathbf{p}$ model for InAs/GaAs QDs as a function of the height. A truncated pyramidal shape with (110)-side facets and base lengths of 13.6 nm was assumed.

5.3. Predicted absorption spectra of truncated pyramidal InAs/GaAs QDs

Excitonic properties are now calculated for self-organized QDs based on a three dimensional implementation of the eight-band $\mathbf{k}\cdot\mathbf{p}$ model and a configuration interaction scheme.[2, 3, 86] The model is applied to flat truncated InAs/GaAs QDs surrounded by a one ML thick InAs wetting layer, as implied by the structural data inferred from the optical results. The base length of the QDs up to this stage was not yet discussed, but will be now determined from comparison to the experimental results in the following.

Figure 5.5 displays calculated exciton absorption spectra for QDs of different height with a base length of 13.6 nm. The spectra show a blue shift of 145 meV for the ground state transition energy upon reducing the QD height from a pointed pyramid down to 3 ML truncated one. The dependence of the transition energies and first excited state splitting on the height of the QDs are summarized for constant base lengths of 10.2 nm and 13.6 nm (grey solid symbols) in Fig. 5.6 (a) and (b), respectively. Open symbols are experimental results obtained by multi-Gaussian fits to the PL spectrum and PLE spectra measured at the maximum of the respective PL peak. The impact of height variations on the inhomogeneous broadening decreases for larger QDs leading to smaller narrower FWHMs and peak separations.

The energetic positions of the ground and excited states (Fig. 5.6) show very good agreement between theory and experiment for a QD base length of 9.1 nm and a QD height of 3 ML or a base length of 13.6 nm and a QD height of 9 ML. This agreement suggests the base length to increase (in 2-3 ML steps) with increasing QD height (in monolayer steps). Qualitative correlations between width and height have been reported previously based on AFM [107, 108] and optical experiments.[109, 110] Variation of theoretical lateral confinement dramatically improves the agreement with the experimental results. The solid black symbols in Fig. 5.6(a) and (b) take into account stepwise increasing the QD lateral extension with increasing QD height, corresponding to an shell-like evolution of the QD volume (see inset of Fig. 5.6(a)). Based on this assumption experiment and theory show absolutely excellent agreement.

Therefore, the average base length and height of the QDs is correlated for the investigated samples. With increasing volume of the QDs the height-to-base length (aspect) ratio becomes larger. Calculations predicted such a correlation as a consequence of the size-dependent balance between surface/interface energies and the strain energy.[111] Note, that the reported results might be bound to the used growth conditions. However, we believe that similar effects take place in a larger range of growth conditions, though the interface quality and the overall height variation might be too small to observe the ML-splitting, being the basis of the current paper.

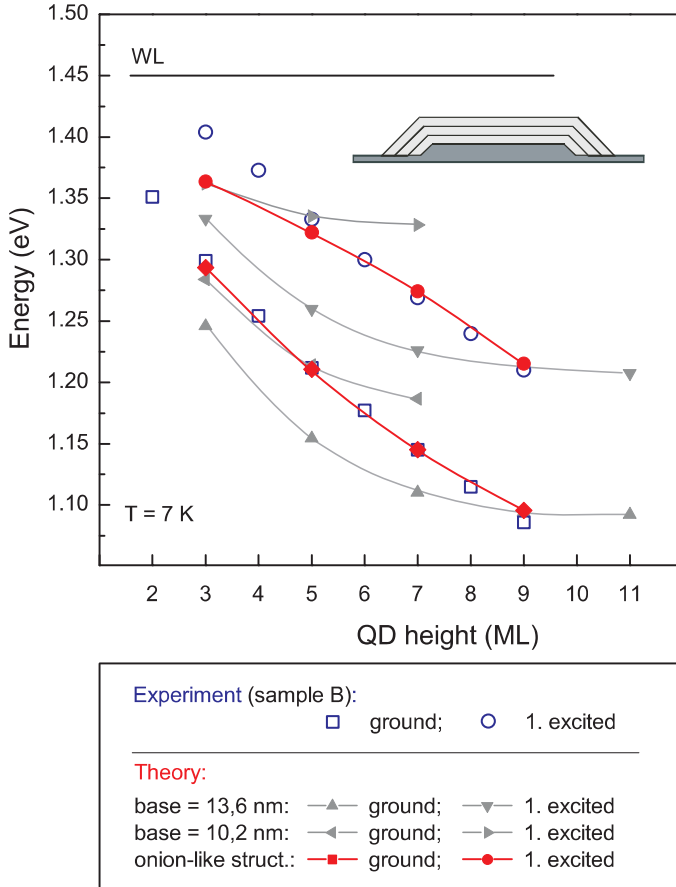


FIGURE 5.6. Predicted (solid symbols) and observed (open symbols) energies of the ground ($n=0$) and first excited ($n=1$) exciton transition in truncated pyramidal InAs/GaAs QDs as a function of height. The red symbols refer to a series of four QDs with a onion like size distribution. The smallest (largest) has a base length of 9.1 nm (13.2 nm) and a height of 3 ML (9 ML). The results are compared to truncated pyramidal QDs with base length 13.6 nm and 10.2 nm are shown. Only the height was varied in the latter two series.

5.4. Single-dot spectra obtained from cathodoluminescence spectroscopy

Single QDs were probed in a cathodoluminescence (CL) setup [76]. The samples were mounted on the cold finger of a He-flew cryostat in a JEOL JSM 840 scanning electron microscope. The acceleration voltage was 7 kV. The luminescence was dispersed by a 0.3 m spectrometer equipped with a 1200 grooves/mm grating and detected by a LN-cooled Si-CCD. At 1.28 eV the minimal full width at half maximum (FWHM) as given by the setup was $\sim 140 \mu\text{eV}$. Due to the spectral sensitivity of detector only luminescence with energies ≥ 1.2 eV can be detected. To reduce the number of simultaneously probed QDs an Au shadow mask was evaporated onto the sample surface, having apertures of ~ 100 nm diameter. For that size and a QD density of $4 \cdot 10^{10} \text{ cm}^{-2}$ about 4 QDs are probed in average.

A representative CL spectra, as shown in Fig. 5.7(a), consist of a rather large number of sharp lines, which originate from various few-particle complexes in different QDs. Therefore first of all the lines stemming from the same QD must be identified. After having done this the lines from one QD need to be attributed to the recombination of various few-particle states like exciton (X), positive or negative trion (X^+ or X^-), biexciton (XX) or charged biexciton (XX^{+-}).

The first step of identification, the discrimination of spectra from different dots, is based on the omnipresent spectral jitter [112] of the transition energies. Statistical variations of the local electric field cause

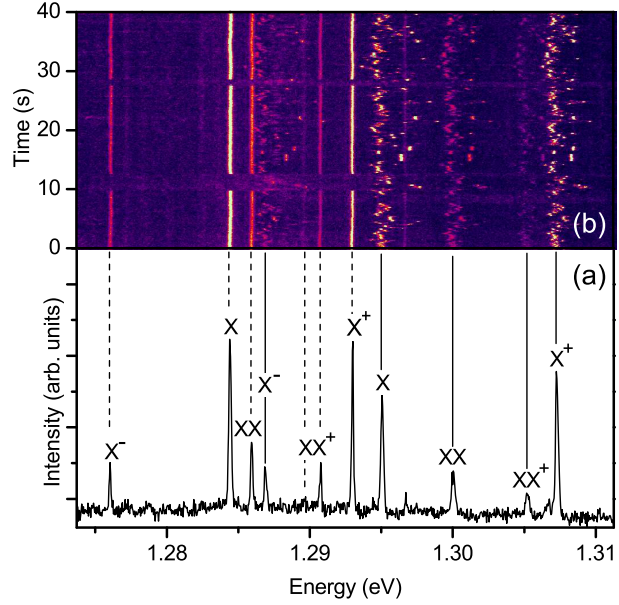


FIGURE 5.7. (a): A typical spectrum as measured through a 100 nm aperture. b: Temporal evolution of (a) consisting of 500 spectra, each being integrated for 80 ms. The spectral jitter allows to identify two overlapping single QD spectra marked by dashed (QD_1) and full (QD_2) lines in (a). The different recombinations are marked as follows. X : exciton, XX : biexciton, $X^{+/-}$: positively/negatively charged exciton (trion), XX^+ : positively charged biexciton.

variations of the quantum-confined Stark effect leading to spectral jitter which is different for each QD (Fig. 5.7(b)).

Next the spectral lines from one QD need to be identified. The *exciton/biexciton* emissions are cross-polarized doublets of identical splitting but reversed polarization with respect to [110] as outlined in [76]. The observed splittings between 60 μ eV and 134 μ eV are attributed to the fine structure splitting of the bright exciton state caused by the C_{2v} symmetry of the confinement potential resulting from the piezoelectric potential [3] and (or) a possible lateral QD-elongation [113]. Exciton and biexciton emissions are distinguished by their characteristic excitation density dependence's. The effective excitation density was varied scanning the electron beam across the aperture and using the integrated intensity as reference. The exciton appears first with a slope of ~ 1 whereas the biexciton intensity depends quadratically on the excitation density [114].

The complete lack of a measurable fine structure of the other emissions indicates the recombination of *trions* and larger charged exciton complexes, for which either the electron or hole spin is paired off, thus quenching the exchange interaction. Charged exciton complexes have been investigated in detail recently [92–98]. Identification of the trions as being positive or negative is not obvious or trivial. Their intensity is however, a function of the background doping: Increased p-type doping for instance results in a stronger emission from positive trions as is confirmed here by extra samples.

This identification procedure has been performed for more than 70 single-dot spectra and the resulting energy differences between the few particle states are plotted in Fig. 5.8 with respect to the single exciton recombination energy.

5.5. Results and Interpretation

Figure 5.8 shows (a) the negative trion is always red shifted compared to the exciton whereas the positive one is blue shifted. (b) The biexciton turns from binding (i.e. red shifted) to antibinding with increasing

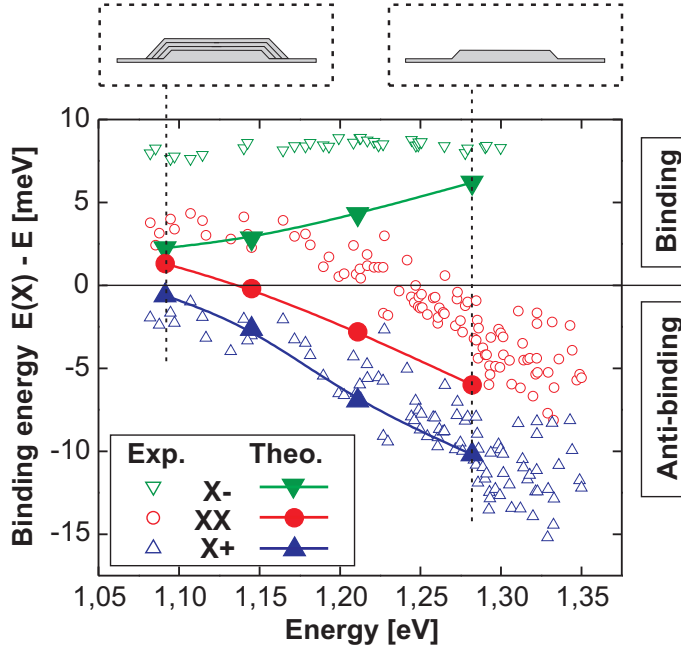


FIGURE 5.8. Energy distances between the recombination energy of the few-particle states as a function of and relative to the neutral exciton recombination energy. The straight lines are linear fits as guides for the eyes. The curved straight line gives the PL spectrum. The accessible energy range is given by the spectral sensitivity of the Si-CCD detector.

exciton energy [76]. (c) The negative trion and the exciton have a similar slope (containing each only one hole). The positive trion and biexciton slopes are parallel both having two occupied hole states.

To understand these findings configuration interaction (CI) calculations were carried out.

In Ref. [66] we have interpreted the results in terms of different degree of correlation for the differently sized QDs, by showing that a variation of the CI-basis size, thus, emulating a different number of confined states for smaller and larger QDs, can reproduce the observed behavior for the binding energies. This procedure, however, met the criticism of Combescot *et al.*[115], pointing out, that this is a mere mathematical effect, not describing the true physics. Therefore, we repeated the calculations with the following refinements: (a) The onion-like size series is slightly changed to even better match the exciton energies in Fig. 5.6. The series consists of four QDs, the smallest (largest) with a base length of 9.1 nm (13.2 nm) and a height of 3 ML (9 ML). The size parameters are very similar to series *H* in Sec. 3.1 (see also Fig. 3.1), but not identical.

The resulting energies for exciton, biexciton and the charged trions are shown in Fig. 5.8 along with the experimental data. The comparison reveals a very good agreement with the experimental findings (a-c). The relative order of the few-particle states is well reproduced. The negative trion is the most binding state and the positive one the most anti-binding state. The biexciton binding energy changes its sign and becomes anti-binding for smaller QDs. The quantitative agreement is very good for small QDs. For larger QDs, the binding energies of negative trion and biexciton are underestimated. For this region, however, a modest elongation, which is not accounted for here, can play a role. This, together with piezoelectricity can change the binding energies (see Fig. 4.8), possibly leading to an even better agreement with experiment.

The origin of the strong change of the binding energies is a combination of direct Coulomb interaction and correlation.

5.5.1. Direct Coulomb interaction and correlation. The smaller the QDs become, the larger is the electron wavefunction spread out. The hole wavefunction, in contrast remains strongly confined in the QD. As a result, the electron-electron Coulomb repulsion $J_{00}^{(ee)}$, being already smaller than $J_{00}^{(hh)}$ for 9 ML QD

height, decreases strongly, whereas the hole-hole repulsion increases. Therefore, according to Eqs. 4.1, the negative trion becomes even more binding with smaller QD size and the positive trion more anti-binding.

For the biexciton, the situation is more subtle. As long as $2|J_{00}^{(eh)}| = J_{00}^{(ee)} + J_{00}^{(hh)}$, the biexciton would be degenerate with the exciton energy, if correlation is neglected. In our case, however, we observe that the binding term $J_{00}^{(eh)}$ is smaller than the average of the anti-binding contributions. For the larger QDs this defect is small and outweighed by correlation. Since the latter is larger for the biexciton than for the exciton a positive binding energy arises in this case. For smaller QDs, in contrast, the binding term $J_{00}^{(eh)}$ is dropping drastically in comparison to the average of the anti-binding Coulomb contributions, $1/2(J_{00}^{(ee)} + J_{00}^{(hh)})$, and can not be outweighed by the rising biexciton correlation energy. Consequently, the biexciton binding energy changes its sign and becomes antibinding.

5.6. Conclusion

The observation of a pronounced modulation in the PL of InAs/GaAs QDs grown by MOCVD with antimony as surfactant enables direct optical access to structural properties of self-organized QDs. The modulations are attributed to variations of the QD-size in monolayer steps. We further deduce a flat shape with both a structurally and chemically well-defined upper InAs/GaAs (001) interface. PLE-experiments showing a large exciton level splitting of 120 meV support a practically ideal InAs composition of small QDs. The comparison to calculations based on eight-band $\mathbf{k}\cdot\mathbf{p}$ theory suggest a systematic correlation of the QD height, base length, and aspect ratio to the QD volume, resulting in an onion like QD size distribution.

These advances allow for a correlation of single-dot spectra obtained from cathodoluminescence measurements to the structure of the probed QD. Thus, we found the sign of the biexciton binding energy to depend on the QD-size. A detailed comparison to calculations using the CI-method shows very good agreement. The sign change of the biexciton binding energy is attributed to a subtle interplay of binding and anti-binding Coulomb terms. The former are decreasing drastically for flat QDs, due to the large electron wavefunction spread out, and the hole ground state orbital remaining strongly confined. Although the (binding) biexciton correlation energies are rising too, the repulsive Coulomb effects cannot be outweighed anymore and the biexciton becomes anti-binding.

CHAPTER 6

Stacked quantum dots

In this section we investigate the electronic properties of QD stacks. Their actual and potential applications are numerous, ranging from the mere increase of active media volume,[12] over the creation of entangled photon pairs,[13] for quantum information processing,[14] the tailoring of the TE/TM mode intensity ratio[15] of QD based semiconductur optical amplifiers,[16–18] to the quantum dot cascade laser.[19, 20]

QD molecules have been fabricated in a way, that the single individual species are as similar as possible.[116–120] Tunneling processes through pairs of QDs have been investigated experimentally [121] and theoretically.[122–125] Optical properties of single pairs of vertically stacked QDs have been studied [126], electric fields [127] and magnetic fields [128] have been applied. The effect of size fluctuations has been investigated in [129] and stacks of very differently sized QD have been studied in [109, 130].

The stacking of QDs can lead to the coupling of electronic states with the formation of binding and anti-binding states. The main parameters, that determine the onset of electronic coupling, are the inter-QD distance, the relative QD size, the symmetry of the overlapping single QD wavefunctions, and strain and piezoelectricity. To quantify the impact of these parameters we will consider pairs of structurally *identical* and *nonidentical* QDs with varying spacer thickness and QD-shape. Furthermore, external electric fields are applied to tune the resonance energies of the adjacent QDs.

6.1. Energetics of QD stacks

In the following section we will employ perturbation theory, originally developed for molecular chemistry, to identify the basic parameter that govern the electronic coupling in stacks of identical and nonidentical QDs.

Suppose, $|u_i\rangle$ are the single-particle Eigenstates of two *decoupled* QD systems A and B with Hamiltonian \mathcal{H}_A and \mathcal{H}_B . Now we consider the composite System $A \cup B$ with Hamiltonian $\mathcal{H}_{A \cup B}$ and ask for the new Eigenstates $|c_i\rangle$ and their corresponding properties.

The analysis, based on the RITZ-procedure, will proceed in the following steps:

(a) Choice of a single-particle Hamiltonian

$$\mathcal{H}_{A \cup B} = H_{\text{Kin}} + V_{A \cup B}$$

for the composite system. H_{Kin} is the kinetic energy operator and $V_{A \cup B}$ the confinement potential of $A \cup B$.

(b) Choice of an appropriate basis set, not necessarily orthogonal. In our case, we employ the single QD single particle Eigenstates $|u_i^A\rangle$ and $|u_j^B\rangle$, which are continued to $|u_k^{A \cup B}\rangle$. Note, that this basis set is in general non-orthogonal.

(c) Expansion of $\mathcal{H}_{A \cup B}$ into $|u_k^{A \cup B}\rangle$ and subsequent diagonalization. If the Ansatz $|c_i\rangle = \sum_j \alpha_j |u_j^{A \cup B}\rangle$ is put into the Eigenvalue equation

$$\mathcal{H}_{A \cup B} |c_i\rangle = E_i^{A \cup B} |c_i\rangle$$

and left hand multiplied by $\langle c_j |$ one arrives at the following set of linear equations:

$$\begin{pmatrix} H_{11} & H_{12} & \cdots & H_{1n} \\ H_{21} & \ddots & & \vdots \\ \vdots & & & \\ H_{n1} & \cdots & & H_{nn} \end{pmatrix} \begin{pmatrix} \alpha_1 \\ \alpha_2 \\ \vdots \\ \alpha_n \end{pmatrix} = E_i^{\text{AUB}} \begin{pmatrix} \Gamma_{11} & \Gamma_{12} & \cdots & \Gamma_{1n} \\ \Gamma_{21} & \ddots & & \vdots \\ \vdots & & & \\ \Gamma_{n1} & \cdots & & \Gamma_{nn} \end{pmatrix} \begin{pmatrix} \alpha_1 \\ \alpha_2 \\ \vdots \\ \alpha_n \end{pmatrix},$$

with

$$H_{ij} = \langle u_i^{\text{AUB}} | \mathcal{H}_{\text{AUB}} | u_j^{\text{AUB}} \rangle, \quad \Gamma_{ij} = \langle u_i^{\text{AUB}} | u_j^{\text{AUB}} \rangle.$$

Since the basis functions $|u_i^{\text{AUB}}\rangle$ are non-orthogonal, $\Gamma \neq \mathbf{1}$, the matrix $\Gamma^{-1}\mathbf{H}$ is to be diagonalized. If this procedure is applied to the simple case of a QD-pair with one bound single-QD-state as starting point, one arrives at

$$E_{1,2}^{\text{AUB}} \approx \frac{E_1^{\text{A}} + E_1^{\text{B}}}{2} \pm \sqrt{\frac{[(E_1^{\text{A}} - E_1^{\text{B}}) - (\Gamma_{11} - \Gamma_{22})]^2}{4} + (H_{12} - \Gamma_{12})(H_{21} - \Gamma_{21})}.$$

For $\Gamma \approx \mathbf{1}$ the equation simplifies to:

$$E_{1,2}^{\text{AUB}} \approx \frac{E_1^{\text{A}} + E_1^{\text{B}}}{2} \pm \sqrt{\frac{(E_1^{\text{A}} - E_1^{\text{B}})^2}{4} + H_{12}H_{21}}.$$

The quantity $|E_i^{\text{AUB}} - E_j^{\text{A,B}}|$, which describes the coupling strength, becomes larger the smaller $|E_1^{\text{A}} - E_1^{\text{B}}|$ (resonance term) and the larger $H_{12} = \langle u_1 | \mathcal{H} | u_2 \rangle$ (overlap term) is. Therefore we can formulate three basic conditions for electronic coupling:

(1) *The resonance condition:* The closer the single QD energies E_i^{A} and E_j^{B} are, the stronger can be the coupling.

(2) *The spacial overlap condition:* The continued states $|u_i^{\text{A}}\rangle$ and $|u_j^{\text{B}}\rangle$ need to overlap each other, otherwise the integral $H_{ij} = \langle u_i | \mathcal{H}^{\text{AUB}} | u_j \rangle$ vanishes.

(3) *The symmetry condition:* H_{ij} vanishes too, if the states $|u_i^{\text{A}}\rangle$ and $|u_j^{\text{B}}\rangle$ carry incompatible symmetry character, meaning that they belong to different irreducible representations of the QDs symmetry group.

Aside from the above mentioned conditions, the number of QDs inside a stack is of course another important quantity, which affects the character of electronic coupling.

The schematic, shown in Fig. 6.1, depicts the three principal set-ups for vertical stacks of QD and the resulting hybride orbitals: (a) A couple of identical QDs with two orbitals in resonance, both having the same quantum number, (b) a couple of non-identical QD with the two levels out of resonance, and (c) a couple of very different QDs with two levels in resonance that belong to different quantum numbers. These three cases are investigated in the following section. The impact of strain and piezoelectricity on the resonance condition, the role of the carrier type (electron or hole) is analyzed. Electric fields are applied to tune the energy levels of adjacent QDs relative to each other.

6.2. Role of strain and piezoelectricity

QD stacks consisting of structurally and chemically identical QDs feature an identical confinement potential in each dot – so far strain and piezoelectricity are not considered. The inclusion of the latter affects each QD in an individual way, depending on the number, position and size of the other members of the QD stack.

In this section we focus on the role of strain and how it affects the confinement potential, the electron states, the HH/LH ratio and the hole coupling. Further on, we turn to the impact of piezoelectricity, considering first and second order effects.

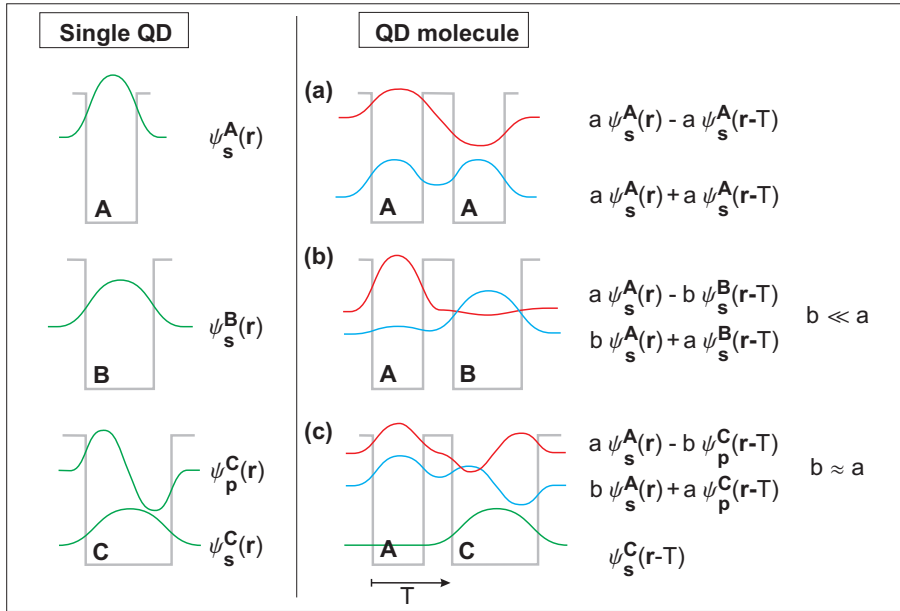


FIGURE 6.1. Idealized (no strain) principal scheme for the formation of hybrid electronic states out of single QD states for (a) A pair of identical QDs (A,A), (b) a pair of slightly different QDs (A,B), and (c) a pair of very different QDs. In the first case (a) the s -states are in resonance and the hybrid states form binding and anti-binding states. In case (b), only weak coupling is expected, since the s -orbitals are not in resonance anymore: The resulting ground state (blue) resides mainly in the larger QD, whereas the first excited state is basically localized in the smaller QD. In case (c), the s -orbital of the small QD is in resonance with the p_z -orbital of the large QD. The ground state (green) of the composite system consists of the s -orbital stemming from the large QD, showing no coupling to the small QD. The resonant s - and p_z -orbitals form binding (blue) and anti-binding states (red). In cases where the s -orbital is resonant to the $p_{x,y}$ -orbitals, no formation of hybrid states is expected since their overlap integral vanishes in many cases for symmetry reasons (see text).

6.2.1. Strain. The strain calculation for QD stacks can be performed in two alternative, but equivalent ways:

- (1) The individual QDs, forming the stack, are placed at the desired positions of the numerical grid and the strain $\epsilon_{ij}^{\text{stack}}(\mathbf{r})$ is calculated in one sweep.
- (2) If the strain distribution of the individual QDs is known, one can alternatively add up their strain fields according to:

$$(6.1) \quad \epsilon_{ij}^{\text{stack}}(\mathbf{r}) = \sum_{k=1}^{\# \text{QDs}} \epsilon_{ij}^k(\mathbf{r} - \mathbf{T}_k) ,$$

with \mathbf{T}_k being the translation vector of the k^{th} QD relative to the first one.

The second approach is especially useful for showing, how the strain field renders the confinement potential of the individual QDs in-equivalent. For this purpose we consider a triple stack of identical truncated pyramids, as shown in Fig. 6.2. The interior strain of the central QD (according to Eq. 6.1) is superposed by the exterior strain of the upper and lower QD. Their distance is the same and, hence, their impact on the central QD is of similar magnitude. The strain inside the lower dot, on the other hand, is superposed by the one of the adjacent central dot and by that of the more remotely situated uppermost QD. The impact of the latter on the lowest dot, however, is almost negligible. Hence, the strain inside the lowest dot is effectively superposed only by the inner dot. This becomes visible in Fig. 6.2(a), where the hydrostatic and biaxial

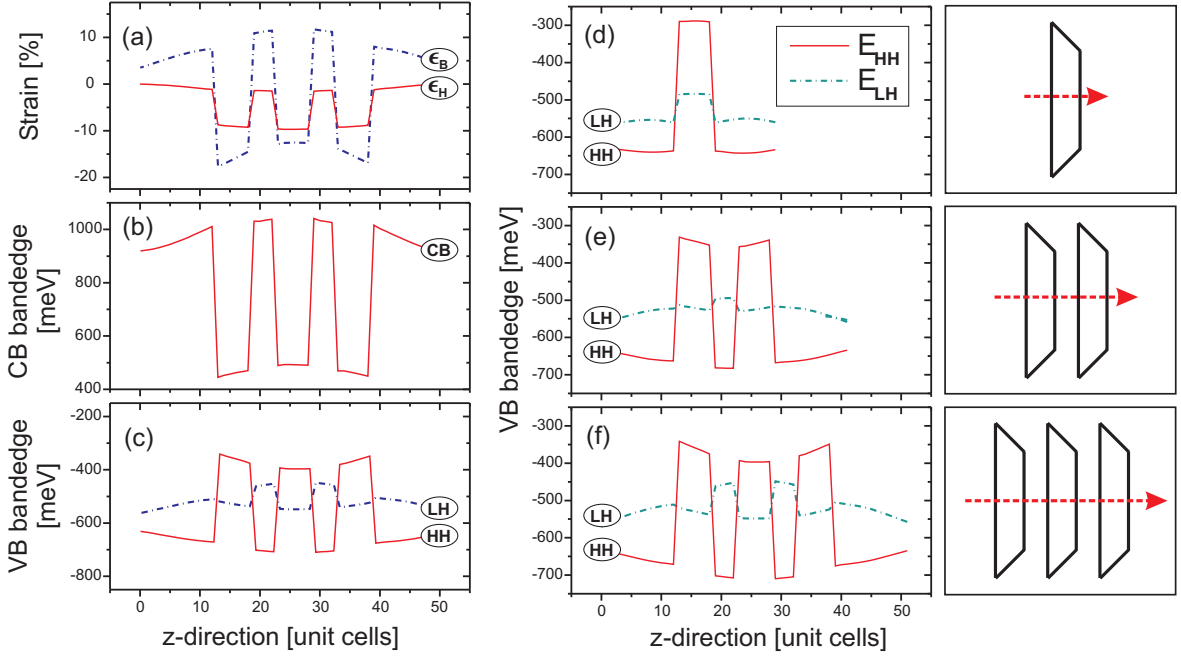


FIGURE 6.2. [Left (a)] Hydrostatic and biaxial strain for a triple stack of truncated QDs. (b,c) the resulting local conduction and valence bands. [Right (d-f)] Heavy and light hole valence bands for (d) a single QD, (e) a QD molecule, and (f) for a triple stack of QDs.

strain are shown. The hydrostatic strain is largest in the inner QD, whereas the biaxial strain peaks at the lowest QD. Their impact on the local confinement potential is shown in Fig. 6.2 (b-f) for a single dot, a QD molecule and a triple stack. The hydrostatic strain, ϵ_H , shifts the conduction band by $a_c \epsilon_H$, with a_c being the CB deformation potential, and the VB by $a_v \epsilon_H$, with the VB deformation potential a_v . The biaxial strain, ϵ_B , further splits the HH- and LH-band by $b \epsilon_B$, with the shear deformation potential b . Following the hydrostatic strain, the CB is largest for the inner QD. The larger biaxial strain at the position of the outermost QDs translates into a larger HH/LH-band splitting, creating the deepest (heavy) hole potential at the lower and the upper QD, respectively.

6.2.2. Piezoelectricity. From the single QDs it is known,[2] that piezoelectricity can break a structural $C_{\infty v}$ or C_{4v} symmetry down to a confinement symmetry of C_{2v} . In this paragraph, we extend this study to stacks of QDs, in order to understand the mechanism, how each individual QD is affected. In Fig. 6.3 the piezoelectric fields are compared for a single QD, a double and a triple stack of QDs. The first, second order fields and the resulting net-potentials are shown for each individual QD of the stacks.

First order piezoelectric field: In general, the potential has a quadrupole like character. In case of the single QD the polarity is changing from the interior to the QD exterior at each corner. The lateral field orientation above the QD is reversed compared to that below the QD, which will be important for its impact on the adjacent dots in case of a QD stack. In this case we observe (i) for the outer QDs a strong increase of the potential range, (ii) an orthogonal field orientation for the uppermost and lowest dot, and (iii) no changing polarity between inside and outside. This behavior can be ascribed to an intricate superposition of all single QD fields: The piezoelectric field of the lowest dot of the triple stack, for example, is superposed by the lower piezoelectric potential of the two upper dots. Their lateral field alignment has the opposite orientation compared to the upper field of the two lowest QDs superposing the piezoelectric field of the uppermost QD. As a consequence the lateral field orientation of the uppermost and lowest QD are orthogonal to each other. Inside the central QD the opposite fields originating from the upper and lower QD cancel each other leaving behind the case of a single QD as in the first case of Fig. 6.3.

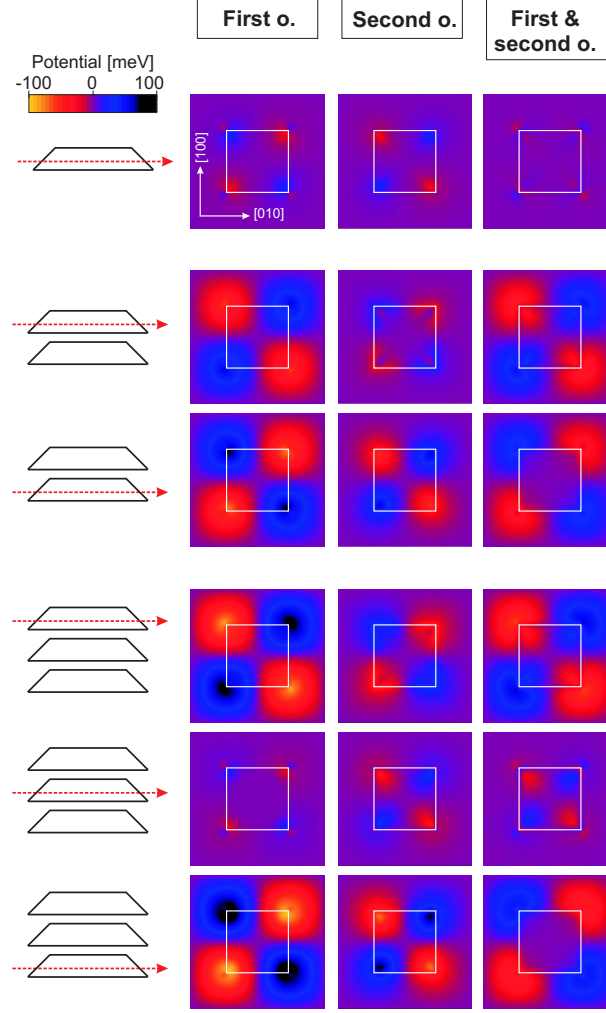


FIGURE 6.3. Lateral scans through the piezoelectric potential: linear part (left), the quadratic part (middle) and the sum of both (right) shown for a single QD, a QD molecule, and a triple stack of QD. The molecule and the stack are made up of truncated pyramids with 18.9 nm base length and 12 ML (3.4 nm) height.

Second order piezoelectric field: Compared to the first order field, the second order field is larger inside the QD and smaller outside (Sec. 3.2.1). Hence, in a QD stack the impact of the adjacent QDs is smaller compared that the one of the first order case. Still, their influence is strong enough to rotate the field inside the uppermost dot compared to the single QD.

Net piezoelectric field: By adding first and second order piezoelectric field one arrives at a practically field-free interior of a single QD, which however is valid only for this specific geometry. This remains true for the lowest QD in the stacks, but changes for the uppermost QD, where the first order field becomes dominant.

6.3. Strength of electronic coupling in pairs of identical QDs

In Fig. 6.4, the evolution of electron and hole orbitals is shown, starting from a single QD (truncated pyramid), via a QD molecule to a triple stack of identical QDs. The electronic structure calculations were carried out (i) in absence of any piezoelectricity, (ii) the presence of first order, and (iii) the presence of both, first and second order piezoelectric fields.

6.3.1. Electron versus hole coupling. The first striking observation is the always strong coupling of electron states and the absence of almost any coupling for hole states. The electron behavior originates

from the comparatively small effective mass resulting in a much larger barrier penetration and increased overlap of neighboring single QD electron states. According to the *spatial overlap condition*, this results in a formation of coupled states, even if the confinement potential is not symmetric and provides for a small energy detuning. This small detuning, on the other hand, is large enough to push the single QD hole wavefunction out of resonance and to prevent their coupling.

6.3.2. Electron coupling. The single-QD electron ground state is the parent state of the two electron states of the QD-pair and the three electron states in case of the triple stack. According to the number of vertical nodal planes the arising electron hybrid states are denoted as binding (0 node) and anti-binding (1 node) in case of a QD molecule. These notions are chosen in reference to molecular chemistry, without, however, being decisive for the binding character of the QD stack itself.

Although the strain affects the individual QDs inside a stack [see Fig. 6.2 (b) for a triple stack] in a different way – the uppermost and the lowest QD provide the deepest electron confinement –, electronic coupling is strong. No uncoupled electron state is observed in absence of piezoelectricity throughout Fig. 6.4, neither for the double, nor for the triple stack.

The inclusion of first order piezoelectricity does not change the picture in any significant way. The first order terms invoke a distortion of the coupled states: the upper lobe of E1 is oriented along [110] and the lower one along [1 $\bar{1}$ 0]. The lobe in the central dot of the triple stack retains the fourfold symmetry. The coupling of the excited electron states is reduced, but not turned off.

Taking into account second order piezoelectric effects as well, increases the coupling strength of the excited states again and leads to their energetic reordering.

6.3.3. Suppression of hole coupling and the role of strain and piezoelectricity. In contrast to the electron states, no coupling of hole ground states is observed. This behavior is related to their strong effective mass, which prevents them from penetrating the surrounding barrier, resulting in an absence of any spatial wavefunction overlap with hole states of adjacent QDs. This situation can change, if the hole states carry significant light-hole character, as it can be the case for pyramidal QDs or any other QD with a large vertical aspect ratio (see Sec. 2.3.5). Then we start to encounter the same behavior as for electron states. This issue will be revisited in Sec. 6.4, where an electric field is applied to stacks of pyramidal QDs, thus switching on and off electronic coupling by tuning the resonance energy.

For stacks of identical QDs, the hole groundstate is always located in the lower QD, due to an intricate interplay of biaxial strain and QD geometry: The HH-band has opposite gradients inside the outermost QD individuals (see Fig. 6.2), which creates a potential sink at the dot bottom of the lowest and at the top of the uppermost QD. Since the lateral extent of this QD is larger at the bottom than at the top, a localized state is stronger confined in case of the uppermost QD. A bound state in the lowest QD, in contrast, can further extend in lateral direction, since it is preferably located at the QD bottom. Consequently we find its energy smaller than the energy of the state in the uppermost QD.

The *first order piezoelectric field* has its largest magnitude inside the lowest QD. Since the hole states with large HH-character have the ability to adapt their wavefunction shape close to the potential minimum, we find a further increase of the confinement-potential disparity between the two outermost QDs. As a result (see Fig. 6.4), the first two hole states of the double and the triple stack are confined in the lowest QD of the stack.

The inclusion of *second order piezoelectric effects* weakens the additional confinement disparity, imposed by the first order field, resulting into the recovery of the ground- and first excited state orbital order as known from the non-piezoelectric case.

The comparison between the single QD, the QD-pair, and the triple stack reveals (see Fig. 6.5), that the energy gap between electron and hole groundstates increases by about 45 meV for the QD pair and 50 meV for the triple stack. This finding qualitatively explains the, so far unresolved, experimental results of Heidemeier *et al.*[117], who found a blue-shift of 103 meV upon closely stacking of similar sized QDs.

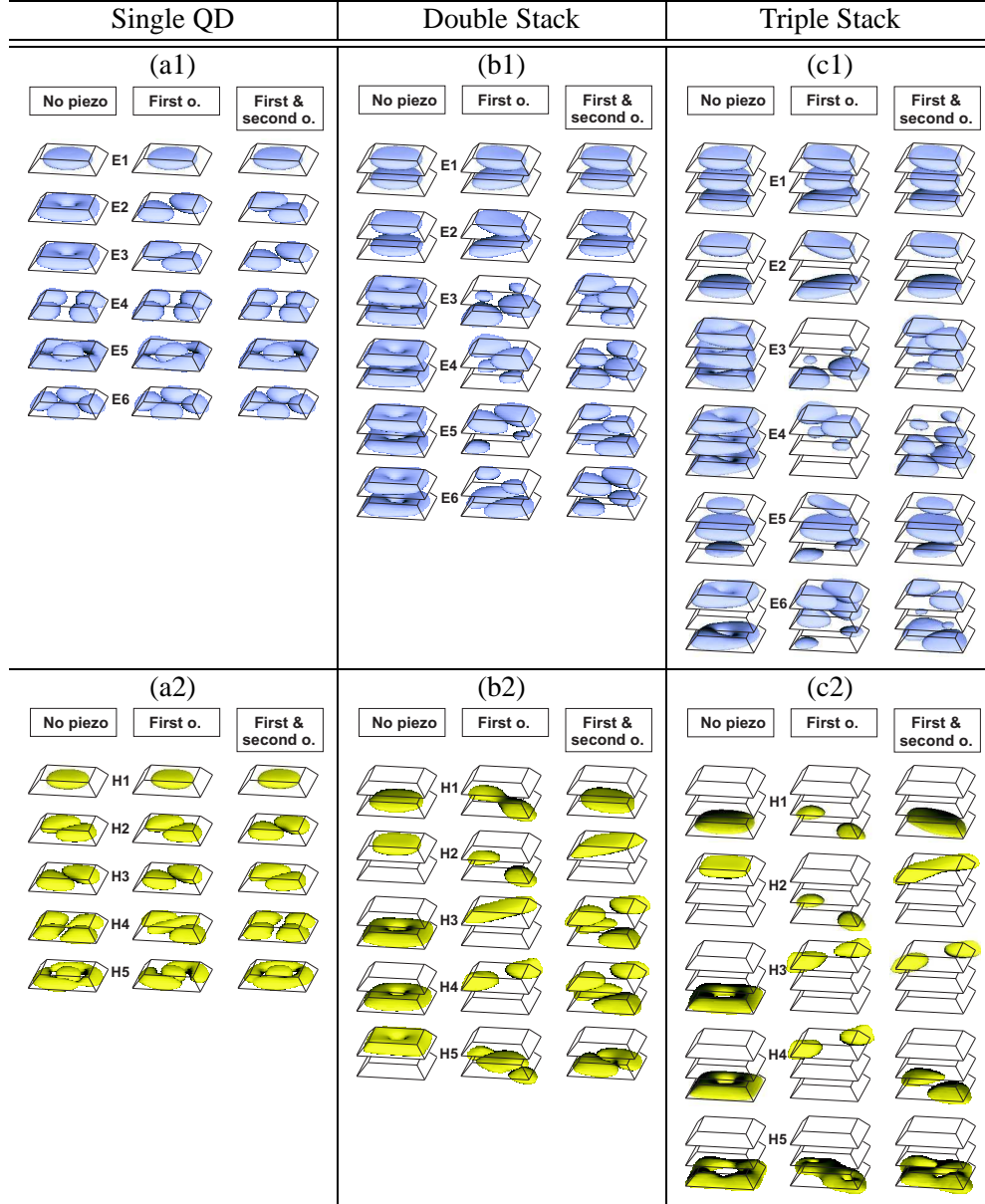


FIGURE 6.4. Electron and hole wavefunctions (isosurface at 65 % probability density) shown for a single QD (a1/2), a double stack (b1/2), and a triple stack (c1/2) made up of truncated pyramids for different orders of the piezoelectric field: linear part (left), the quadratic part (middle) and the sum of both (right in each column).

6.3.4. Varying inter-dot distance. In general, the anti-binding electron state has a larger single particle energy than the binding one. The origin of this behavior can be traced to the increasing number of nodal planes and the resulting larger kinetic energy. This is exactly the same mechanism that provides for the splitting of *s*- and *p*-orbitals in single QDs and it is dependent on the inter-dot distance as the *s-p*-splitting is QD size dependent.

The evolution of the electronic states as function of the inter-dot distance is investigated now for four different structures as depicted in Figs. 6.6, 6.7, and 6.8: (i) A molecule consisting of two truncated pyramids (18.9 nm base length and 12 ML (3.4 nm) height), (ii) a molecule of two QDs with trumpet-shaped like internal composition profile [each QD has the same integral amount of In, compared to the single QD of (i)], (iii) a molecule of two full pyramidal QDs having a base length of 10.2 nm, and (iv) a triple stack of the same pyramidal QDs. First, we focus on the electron sub-system.

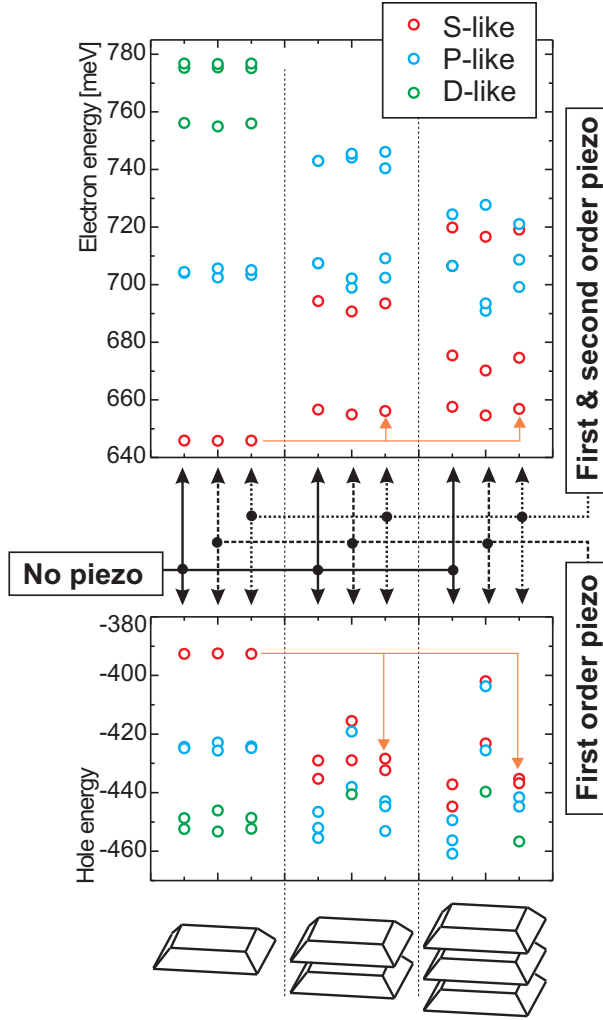


FIGURE 6.5. Electron and hole energies shown for a single QD (left), a double stack (middle), and a triple stack (right) made up of truncated pyramids for different orders of the piezoelectric field: linear part (left), the quadratic part (middle) and the sum of both (right in each column). For the latter, the impact of strain on the ground state energies is indicated by orange arrows. The electron and hole energies are given with respect to the unstrained InAs CB.

Electron states: The first most obvious observation is that the splitting between binding and anti-binding states increases the closer the QD barycenter become. For structure (i) the largest splitting becomes 110 meV at 4 nm distance (counted from QD bottom to bottom) and the anti-binding *s*-orbital crosses with the binding *p*-orbitals. In case of structure (ii), the adjacent QDs can not be placed as close as for structure (i), due to their larger vertical extension. At a distance of 6.4 nm we observe a splitting of 60 meV for both *s*-orbitals. This is larger at this distance compared to the first structure (i), since the larger vertical dot extension of (ii) leads to a thinner barrier between the dots, leading to an increase of the vertical wavefunction spread-out. The latter is also promoted by the closer energetic proximity to the wetting layer-states, which enables a more efficient tunneling into the barrier. For both structures, the single dot energies are marked with red points. Interestingly, we do not observe convergence to these energies within the considered inter-dot distance even for larger dot separations. This finding is related to the influence of strain and piezoelectricity, which are both longer range interactions.

For structure (iii), the pyramidal QDs, we observe a splitting of 50 meV at 5.5 nm distance. This magnitude is comparable to structure (i) for the same distance. In case of the triple stack of pyramidal QDs, (iv), there are three electron states derived from the *s*-orbital having zero, one or two vertical nodal planes. The

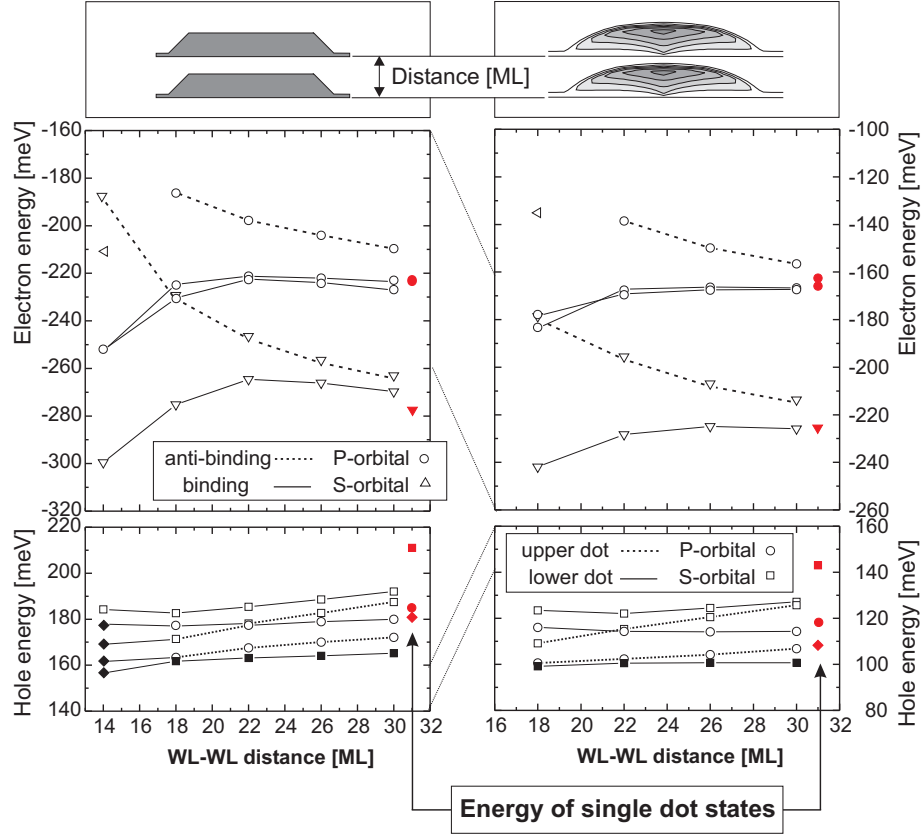


FIGURE 6.6. Single particle electron and hole energies versus inter-dot distance shown for a couple of truncated pyramids and a couple consisting of InGaAs QD containing a trumped shaped In composition profile. The red points are the reference energies of the corresponding single QDs. The electron energies are given with respect to the GaAs CB and the hole energies with respect to the GaAs VB.

energy splitting between the first and the third electron states reaches 70 meV for 5.5 nm inter-dot distance. The second electron state exhibits no energy change at all.

Hole states: The energy and location of the hole states is much more influenced by strain and piezoelectricity than the electrons are. Here we focus on some important peculiarities:

(a) For structure (iii) we have calculated the hole energies in presence and absence of (first order) piezoelectricity. For both cases, the first two energy levels are related to *s*-like wavefunctions, the first one located in the lower and the second one in the upper QD [see Fig. 6.7(a)]. Both energies are decreasing upon smaller dot separation and their splitting increases independent, whether piezoelectricity is included or not. Hence, it is a bare strain effect, related to the decreasing biaxial strain.

For the smallest distance, a hybrid of *s*- and *p*-orbital develops, when piezoelectricity is taken into account. The resulting *s-p*-level anti-crossing is due to the *increasing* energy of the first *p*-state upon smaller dot separation. The latter is related to the accompanied rising of the piezoelectric potential in the lower QD: The *p*-state moves into the resulting potential minima and, thus, overcompensates the strain effects. Switching off the piezoelectric effect in the calculations, in contrast, results in an energy decrease of *both* *p*-states.

The evolution of the hole energies and their wavefunction character in case of the triple stack of identical pyramids (iii) as function of their inter-dot distance is shown in Figs. 6.8, and 6.9. Different colors mark the different wavefunction character. For large inter-dot distance we again observe the same orbital order as for the triple stack of truncated pyramids: The first *s/p*-hole states reside in the lowest, the second in

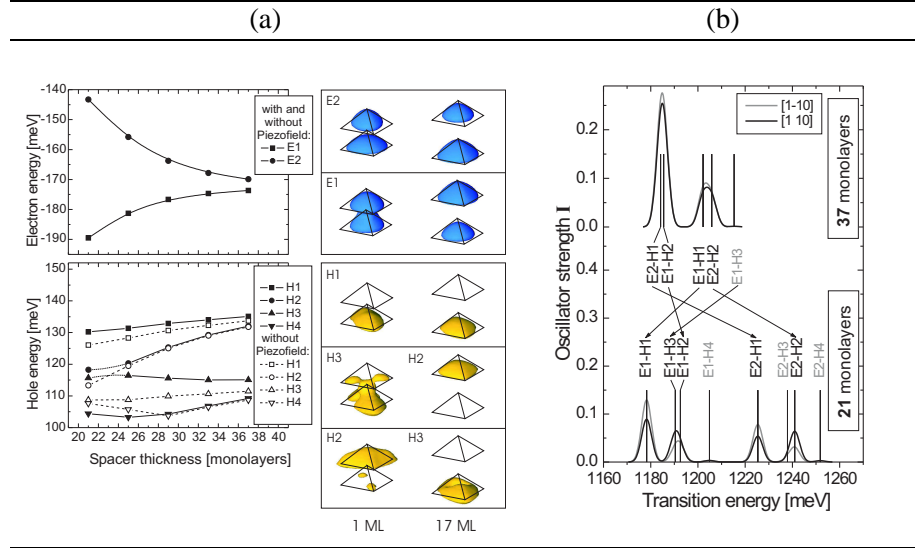


FIGURE 6.7. (a) Single particle electron and hole energies versus inter-dot distance shown for a couple of pyramidal InAs QDs (base length: 10.2 nm). The energies are calculated in absence (open symbols for hole system) and presence of (first order) piezoelectricity. The shown electron energies are unaffected by the piezoelectric field. On the right hand side of panel (a), the electron and hole wavefunction are shown in presence of piezoelectricity for the smallest (21 ML) and the largest (37 ML) distance. The electron energies are given with respect to the GaAs CB and the hole energies with respect to the GaAs VB. (b) Excitonic absorption spectra for the distances 21 ML and 37 ML. In the first case the allowed transitions E2-H1 and E1-H2 are almost degenerate since the E1-E2 splitting is as large as the H1-H2 splitting. Since the splitting of the electron states increases much larger with increasing distance than the first two hole states, a complete reordering of the absorption spectrum results.

the uppermost and the third ones inside the central QD. Upon shrinking inter-dot separation the following peculiarities are remarkable:

The energetic spread among the s-states increases and is ordered according to the strength of the biaxial strain inside the individual dots.

The LH-character increases for all orbitals: For the *s*-states by approximately 50 % and for the *p*-states by up to 100 %.

Upon increasing LH-percentage above 28 % we always observe the appearance of coupled hole states. This fits very well into the picture of the effective mass being one of the decisive quantities governing the strength of electronic coupling.

6.4. Small perturbations of the size homogeneity

If one desires to establish coupled electronic states by stacking identical individual QDs on top of each other the question about the stability of electronic coupling against small relative size variations arises. For this purpose we revisit the molecule of pyramidal QDs, shown in Fig. 6.7, and derive two additional stacks, where the size of either of the QDs is increased by 10 %, as shown in Fig. 6.10. Next, an electric field is applied to turn off-resonant states into resonance and vice versa. The resulting wavefunctions and single particle energies as function of the vertical electric field are shown in Figs. 6.10 ,and 6.11. At zero electric field, a strong suppression of electron coupling for both asymmetric structures is observed. Electron and hole groundstate are localized in the larger QD. The application of a small electric field of 22 and -22 kV/cm respectively, however, is sufficient to establish electron coupling in both molecules. Hole coupling, on the

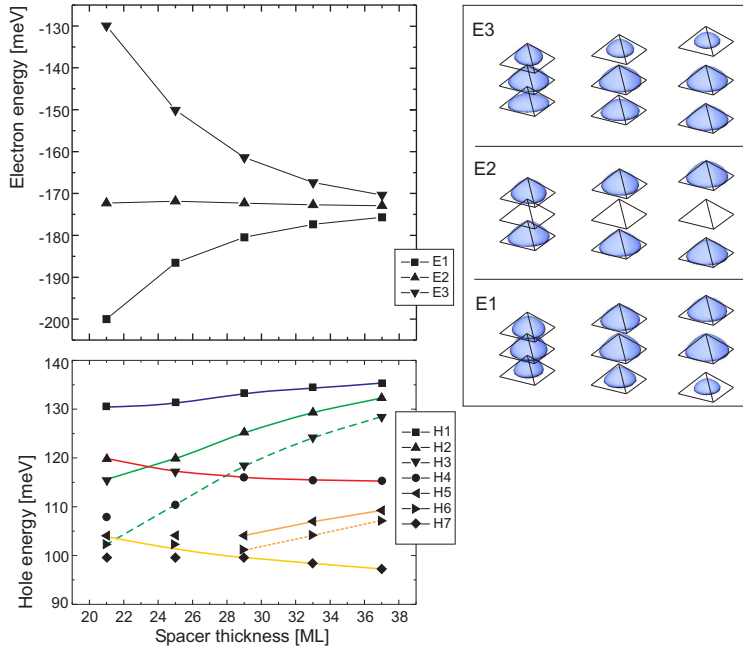


FIGURE 6.8. (Left) Single particle electron and hole energies versus inter-dot distance shown for a triple stack of pyramidal InAs QDs (base length: 10.2 nm). The energies are calculated in presence of (first order) piezoelectricity. The electron energies are given with respect to the GaAs CB and the hole energies with respect to the GaAs VB. (Right) The electron wavefunctions (isosurfaces at 65 % probability density), calculated in presence of presence of (first order) piezoelectricity, are shown in for three distances: 21, 29, and 37 ML. The corresponding hole wavefunction are shown in Fig. 6.9.

other hand, and, hence, state anti-crossing is observed only for higher excited states. The s-like and p-like hole states in the upper and lower QD do not interact with each other and their energy levels cross.

A remarkable peculiarity is the HH/LH ratio of the lower dot *p*-state in all three molecule structures as function of the electric field. For positive field direction it receives an additional force pulling the wavefunction to the pyramid bottom where the local HH-LH band-splitting is largest with the HH-band on top. If the electric field becomes smaller, turning to negative values, the direction of this force reverses and the wavefunction can partly overcompensate the bottom-wards directed inclination of the interior confinement potential and move to the pyramid tip. At this position, the local LH-band has crossed the HH-band and represents the energetically more favorable band. As a consequence of this, we observe an increasing LH-percentage from 13 % for $E_z = 44 \text{ kV/cm}$ to 27 % for $E_z = -44 \text{ kV/cm}$ for the *p*-state of the molecule with the larger dot at the bottom.

6.5. Asymmetric QD molecules: Coupling of different electronic shells

So far only stacks of equally and almost equally sized QDs have been considered. In these quantum structures only those electron states are in resonance that belong to the same quantum number: e.g. the *s(p)*-state of the upper dot with *s(p)*-state of the lower dot. For the stack of closely spaced truncated pyramids, where the anti-binding *s*-state crosses the binding *p*-states, we could not find any interaction.

This observation leads to the more general question of the role of the symmetry, or the wavefunction character, with respect to electronic coupling.

Associated with every QD or QD stack there exists a symmetry group along with their irreducible representations (IrRep). In our case, the latter is employed to classify the electron wavefunctions according to their behavior under the systems symmetry transformations. The way, the classification works, is shown in Fig. 6.12: It contains a reprint of the character table of the point group C_{4v} . This group, used as an

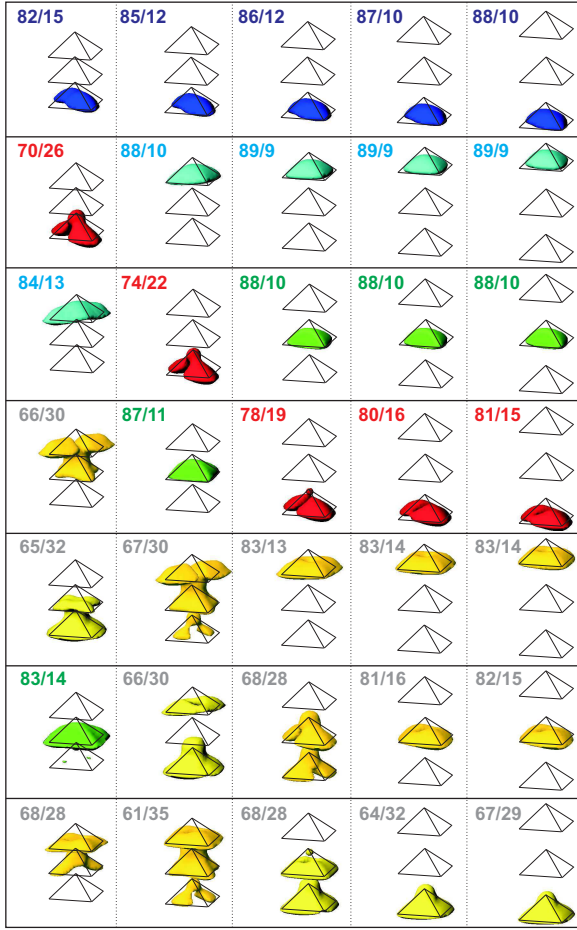


FIGURE 6.9. Hole wavefunctions in a triple stack of pyramidal QDs (base length 10.2 nm) colored according to their symmetry character. The associated numbers refer to the HH/LH hole ratio.

example, represents the symmetry group of a pyramidal QD, provided, its atomistic structure is neglected. Associated with each IrRep (here A_1, A_2, B_1, B_2 and E) there are basis functions, shown in the first row, that carry exactly the symmetry character of each IrRep. These basis functions are shown as grey contour plots in Fig. 6.12. The function $x^2 + y^2$ for A_1 , for instance, is always turned into its identity for every symmetry transformation. The function $x^2 - y^2$, in contrast, is put into its identity only for the 180° rotation and the reflection at the (110) and $(\bar{1}\bar{1}0)$ plane. For all other operations it is turned into minus the identity.

By comparing their transformation behavior to that of the wavefunctions, the electronic states are classified, as shown in Fig. 2.6 for wavefunctions obtained for QDs of different symmetry, and in Fig. 6.13 for those, arising from pyramidal QDs of different size.

This classification does not work for hole states, since the respective LH- and HH-parts can carry different symmetry character.

The key for the coupling behavior of electron states is that the integral $\langle \psi_i^A | \mathcal{H}^{A \cup B} | \psi_j^B \rangle$ of single dot wavefunctions ψ_i^A , bound in the upper dot A, and ψ_j^B , bound in the lower dot B, vanishes, if both wavefunctions belong to different IrReps. Then their overlap integral vanishes and they cannot form coupled states. For symmetric QDs, only those levels with the same IrRep are in resonance and can interact. For asymmetric stacks, in contrast, the s-states of the smaller dot can be in resonance with p- or d-states of a larger adjacent dot. Since s- and p-states carry different symmetry character, no coupling between both is expected. Therefore, we choose a system, where the s-state energy of the lower pyramid is close that of the d-states of the upper pyramid. These levels are highlighted with red boxes in Fig. 6.13. The lower dot s-state and the first two d-states of the upper dot belong to the same IrRep A_1 and the third d-state is part of

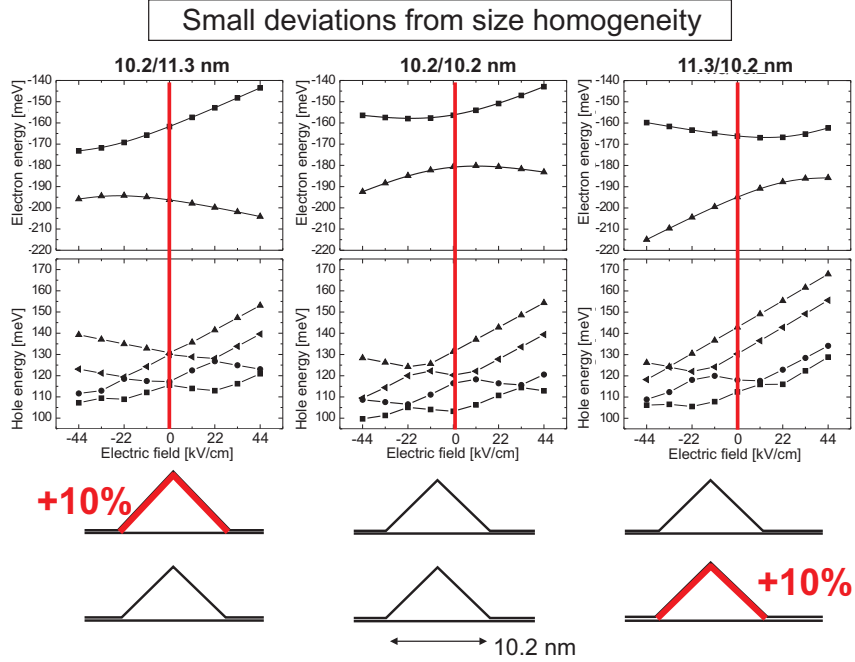


FIGURE 6.10. Electron and hole energies for as function of a vertical electric field shown for three pairs of pyramidal QDs: (middle) a couple of identical pyramids (10.2 nm base length), (left) a pair containing a larger upper pyramid (11.3 nm base length) than in the middle, and (right) a pair containing a larger lower pyramid. The electron energies are given with respect to the GaAs CB and the hole energies with respect to the GaAs VB.

the IrRep A_2 . Hence, we can expect coupling between the former, the s -state and the first two d -states, but not with the third d -state.

By applying a vertical electric field, the energy of the s -state is systematically shifted relative to the d -states, thus, switching on and off the *resonance condition* (see Fig. 6.13). The magnitude of the field, however, was not large enough to bring the s -state in resonance with the third d -state.

The results for the arising energies and wavefunctions for the hybrid system are shown in the lower panel of Fig. 6.13: Surprisingly, at first sight the second d -state (E5 at 0 kV/cm) does not interact with the lower s -state. The apparent hybridization at 22 kV/cm is not accompanied with any anti-crossing signature and it must be regarded as an accidental coupling. The reason for this behavior can be traced to the fact, that the piezoelectric field of the two dots almost compensate each other in the upper dot (the upper QD p -splitting is three times smaller than for the corresponding single QD), thus, restoring C_{4v} symmetry. In this group, however, the first d -state transforms into a different IrRep, B_1 , (see Fig. 2.6) than the lower dot s -state, A_1 . Still, we can observe a hybridization and anti-crossing between the lower dot s -state and the second d -state, since they belong to the same IrRep (A_1), even in the C_{4v} group.

The role of the piezoelectric field becomes even more clear, when the inter-dot separation is varied, as can be seen in Fig. 6.14: Upon changing distance between the two dots, a crossing of the larger QD p -states is observed, being a clear signature of a reorientation of the piezoelectric potential in the upper QD.

In addition, we find, that the electron states shift to higher energies, due to an increase of hydrostatic strain and the hole states shift to lower energies due to the smaller biaxial strain and the resulting reduced splitting of the local HH/LH bands.

6.6. Tailoring the TE-TM ratio in semiconductor optical amplifiers

The purpose of SOAs is the amplification of an incoming optical signal, which is provided by an optical fiber in most cases. Since the light passing through the latter is often unpolarized, the degree of amplification must be polarization independent. The schematic, shown in Fig. 6.15, depicts the two decisive device parts

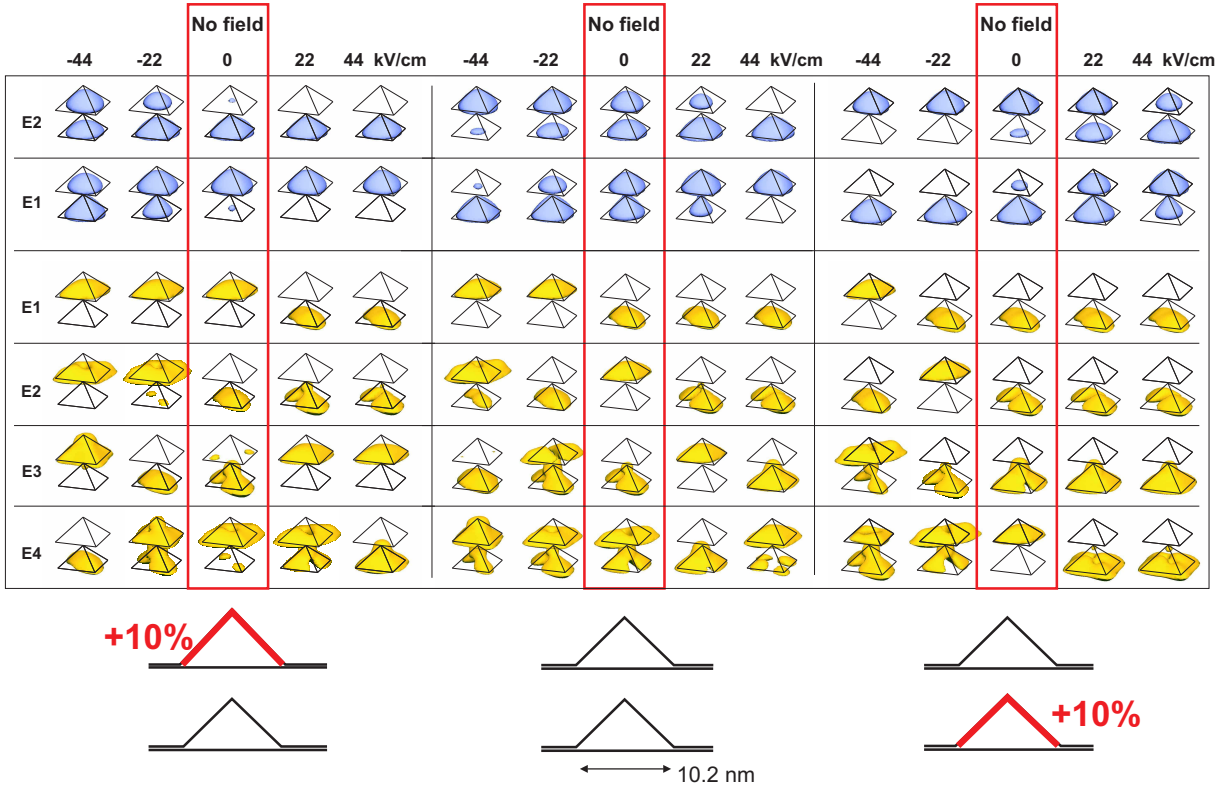


FIGURE 6.11. Electron and hole wavefunctions (isosurfaces at 65 % probability density) for as function of a vertical electric field shown for three pairs of pyramidal QDs: (middle) a couple of identical pyramids (10.2 nm base length), (left) a pair containing a larger upper pyramid (11.3 nm base length) than in the middle, and (right) a pair containing a larger lower pyramid.

governing the polarization: The cavity (white) and the active region (grey). The role of the cavity design was investigated in depth by S. Bognar [131] and out of scope of the present work. Here we focus on the active zone especially on the QD polarization properties. If the device is built, as shown in Fig. 6.15. An optical mode polarized parallel to the cavity is called the TE-mode ($E||e_x$) and perpendicular to the cavity the TM-mode ($E||e_z$).

From quantum wells, used as active medium, it is known, that a radiative transition from the electron system into a HH-band is TE-polarized and into a HH-band dominant TM-polarized. For a strain-free GaAs/AlGaAs quantum well one always finds a HH-band as the groundstate VB, hence, this system can only provide TE-mode amplification, when driven on the groundstate transition. The relative ratio of HH- and LH-bands can be tailored by resorting to strained quantum wells with an active medium having a smaller lattice constant than the surrounding matrix. In this case, the arising (positive) biaxial strain splits the HH-LH confinement potentials with the LH-confinement being above the HH-potential. Eventually, this leads to a compensation of the geometry caused HH-band preference, present in unstrained quantum wells. With the well width and the alloy composition and, hence, the relative lattice constant as design parameters, the device can be fabricated to amplify light *polarization-independent*.

For QDs we encounter an even more complex situation: The geometry and the composition are multi-dimensional parameters each and they are not deliberately adjustable during growth. As consequence of the complex QD geometry, the strain is strongly inhomogeneous.

Therefore, we start with three very simple 3D-structures and investigate their electronic and optical properties with special emphasis on strain, HH/LH ratio and TE/TM polarization:

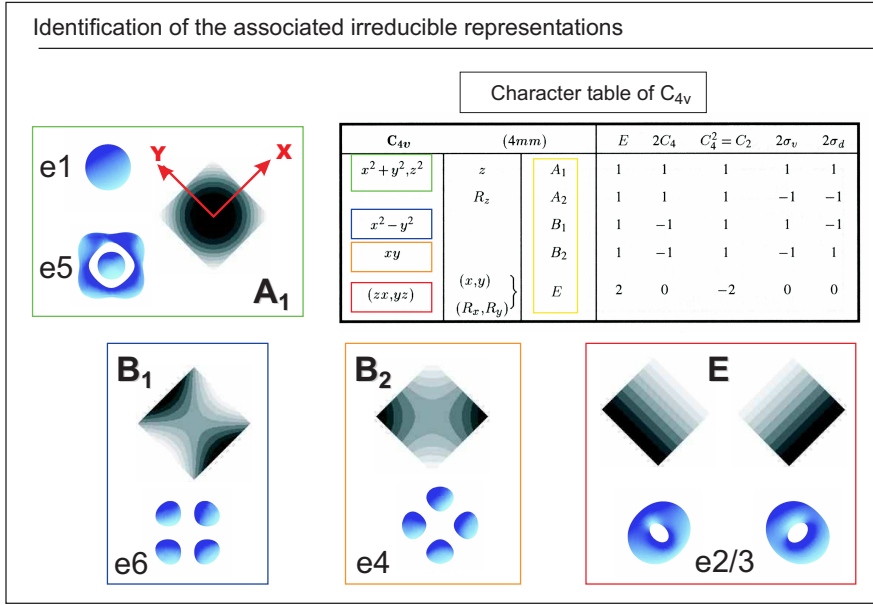


FIGURE 6.12. Following their transformation behavior, the electron states can be classified according to irreducible representation of the systems symmetry group. Here the point group C_{4v} is considered as example. The quadratic basis-functions shown in the first column of the character table serve as guide for the identification of the electron states (blue). These electron states, shown as an example, are Eigenstates of a pyramidal QD, where the piezoelectric field is not taken into account. Therefore, which is in contrast to the C_{2v} group, one also finds two-dimensional irr. representations like E in this case. An Eigenstate, being associated with the latter IrRep, is always (apart from spin) two-fold degenerate, as is e.g. the p-state in this example.

(a) A cube, with equal-length side-facets (10 nm wide), (b) a cube, elongated into the vertical (z)-direction (15 nm height), and (c) a cube, extended in lateral (x,y)-direction (5 nm height). All three structures share the same volume.

The single particle energies of these structures and their degeneracies (not shown) are calculated in absence and presence of strain and piezoelectricity. The latter distinction is necessary to separate pure confinement effects, having their origin in the QD geometry only, from strain related effects, that potentially could compensate for or enhance the geometry driven influences.

In absence of strain in our QDs, the results for the electron subsystem resemble those of a simple particle-in-a-box model with finite barrier height and the corresponding degeneracies: For QD (a), e.g., the p-state is threefold degenerate (apart from spin degeneracy). For QDs (b) and (c), this level is split into a twofold degenerate p-state having a vertical nodal plane each (p_x and p_y) and a non-degenerate p-state with a horizontal nodal plane (p_z). The energy of the latter is above the energy of the p_x - and p_y -orbitals in QD (c), since the vertical confinement is larger than the lateral one. For QD (b), the reverse situation holds, since the vertical confinement is smaller.

By taking strain and piezoelectricity into account, the electron states are shifted to higher energies and many degeneracies are removed. More important for our purpose, however, are the hole states and their HH/LH ratio. The latter is tightly connected with the QD geometry and the strain and it determines the polarization behavior: The recombination of electron and hole can be decomposed into a $e \rightarrow HH$, $e \rightarrow LH$, and a $e \rightarrow SO$ channel. The first one emits TE-polarized- and the second channel dominant TM-polarized light. The last channel is irrelevant due to the large spin-orbit splitting Δ_{SO} and the resulting small SO-percentage.

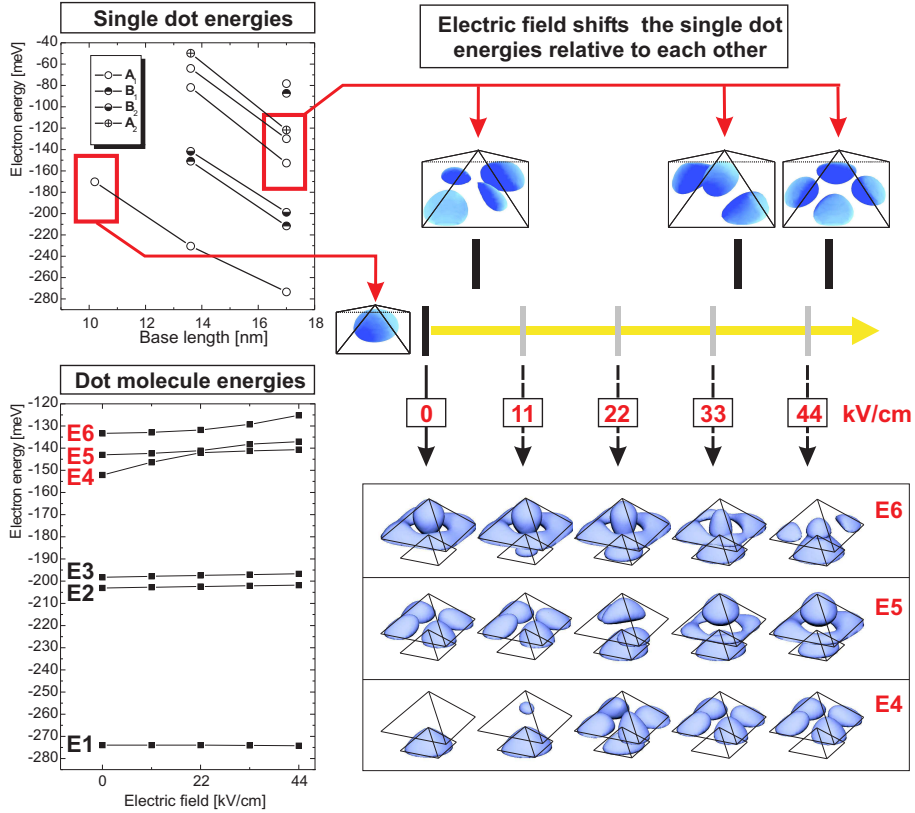


FIGURE 6.13. Pair of very differently sized QDs: the small lower pyramid has a base length of 10.2 nm, whereas the upper one has a width of 17.0 nm. Guided by the upper energy diagram, the QD stack is designed in a way that the *s*-state of the small QD is almost in resonance with the *d*-states of the larger QD. The single particle energies are labeled according to their irreducible representations. An additional vertical electric field tunes the energy of both states relative to each other, thus bringing them into resonance. The resulting energies and wavefunctions are shown in the lower panel. The electron energies are given with respect to the GaAs CB.

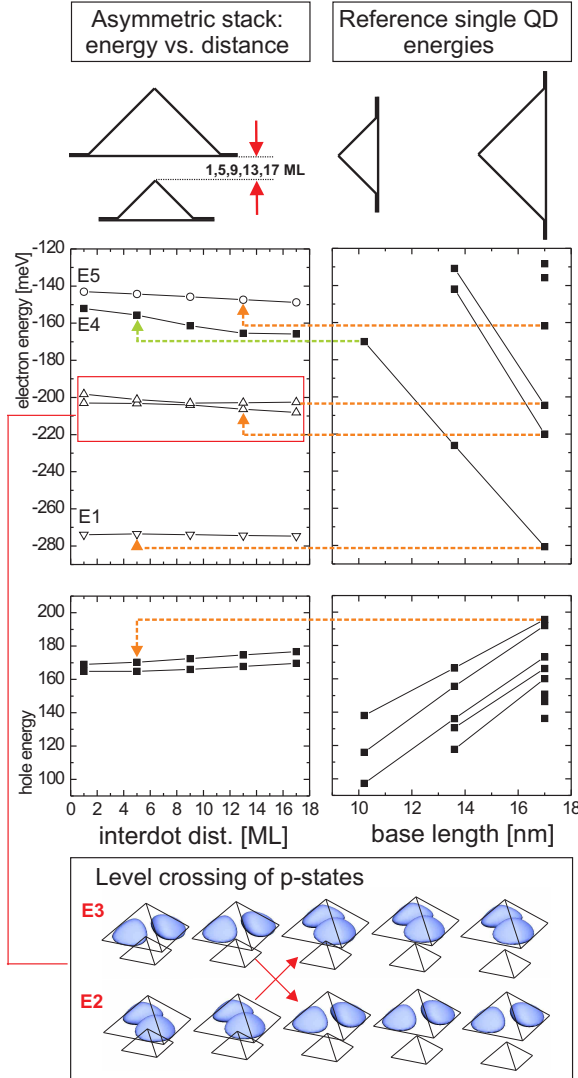


FIGURE 6.14. Energy vs. inter-dot distance for a pair of very differently sized QDs: the base length of the small lower pyramid is 10.2 nm, whereas the upper one has a width of 17.0 nm. Guided by the right hand energy diagram, the QD stack is designed in a way that the *s*-state of the small QD is almost in resonance with the *d*-states of the larger QD. The single dot energies on the right hand side serve as reference. The resulting energies and *p*-state wavefunctions are shown in the lower panel: The former are all shifted to higher (electron states) or lower energies (hole states) resulting from the larger hydrostatic and smaller bi-axial strain in the stack. The superposition of the (first order) piezoelectric fields lead to a field-cancellation inside the upper QD at 9 ML (tip-bottom) distance. As a result, the *p*-states, located in the upper dot, become degenerate and change their order subsequently .

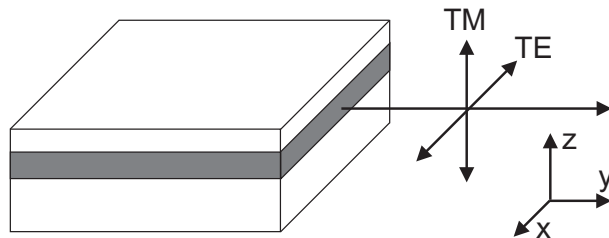


FIGURE 6.15. Typical photoluminescence measurement configuration setup used in experiment.

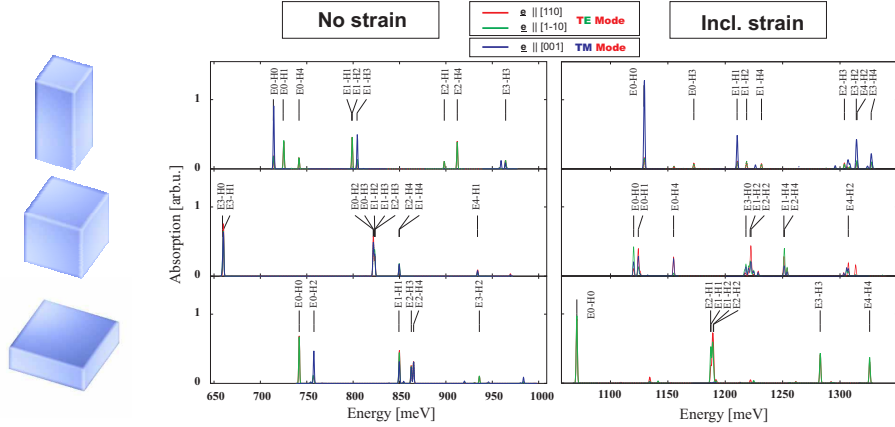


FIGURE 6.16. Excitonic absorption spectra shown for three cube like QDs in absence (left) and presence (right) of strain and piezoelectricity. The TM-mode absorption ($e \parallel [001]$) is shown as blue curve and the TE-mode absorption ($e \parallel [110]$ and $e \parallel [1\bar{1}0]$) as red or green curve. The TE/TM ratio of the absorption is balanced in both cases for the cube with identical side length. In the two other cases strain enhances the already dominant mode, and it shifts all energies ca. 400 to 500 meV to higher energies.

	Strain	Hole States				
		H1	H2	H3	H4	H5
	no	12/86 15/80	72/25 32/63	72/25 37/58	32/66 43/50	77/21 33/63
	yes	49/49 49/45	49/49 49/46	49/49 49/45	49/49 48/45	49/49 50/45
	no	88/10 91/7	53/46 80/15	27/70 78/15	47/63 70/24	52/46 72/22
	yes					

HH/LH ratio: blue: LH-dominant
red : HH-dominant

FIGURE 6.17. The HH/LH ratio of a hole state determines the ratio of the TE/TM absorption. The former ratio is shown for the first five hole states in absence and presence of strain.

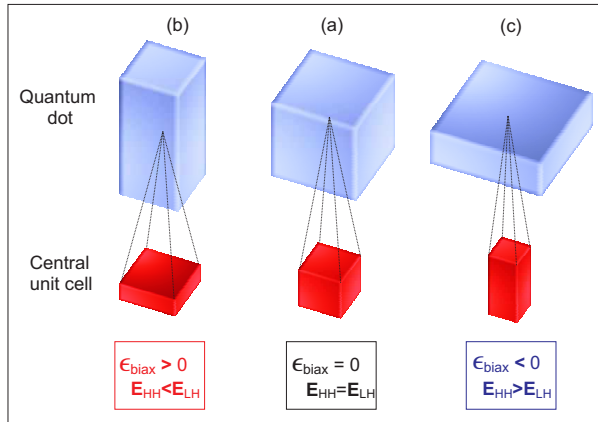


FIGURE 6.18. The relation between the box-shape, the shape of the central unit cell of the QD, the biaxial strain and the resulting position of the local HH- and LH bands inside the QD. This picture holds, if the QD lattice constant is larger than the one of the surrounding matrix. Otherwise the reverse situation for the strain and band position would be true.

In absence of strain, a balanced HH/LH ratio for all calculated hole states of the cube is found (see Fig. 6.17), and, as a result, the same polarization in vertical and horizontal direction for all optical transitions (left panel in Fig. 6.16). The application of strain and piezoelectricity slightly changes the ratio in favor to the HH-part. However, from inspection of the associated wavefunctions, we find the HH-parts of the orbitals pushed into the QD corners, where the piezoelectric field is most attractive. The LH-part, in contrast, remains in the center, therefore having a better overlap with the electron wavefunctions. As a result, we find the integrated intensity of TE- and TM-polarized light very similar for the ideal cube.

The role of strain can be best explained for structures (b) and (c), as is seen in Fig. 6.18: In case of a QD, elongated in vertical direction, a crystallographic unit cell, located in the QD center, receives more stress from the comparatively larger amount of InAs material located in vertical direction than from lateral directions. Hence, the unit cell shape is flat, as shown as red cubicles in the figure. The biaxial strain is negative and the bulk HH-band resides below the LH-band. As a result, we find all hole states having dominant LH-character. In case of the flat QD, the situation is reversed. The unit cell in the QD center is elongated in z-direction, the biaxial strain positive, and the HH-band energetically on top. Consequently, we find the HH-parts of the confined hole states dominant, and almost no TM-polarization of the QD absorption occurs (see Fig. 6.16).

Since the last case resembles very much the QDs one can produce by self-organized Stranski-Krastanow growth, there is little hope to obtain a balanced TE/TM-amplification ratio from a single sheet of state-of-the-art InAs/GaAs QDs.

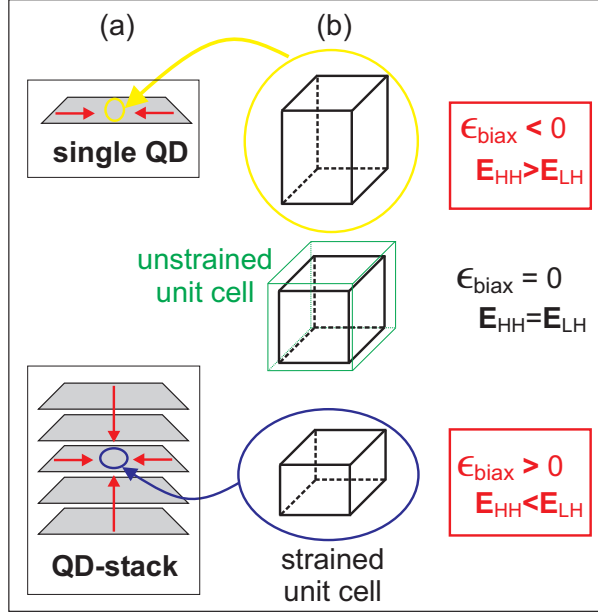


FIGURE 6.19. The shape of a central lying unit cell inside a flat single QD and a stack of QDs. The size and shape of the unstrained unit cell is shown as green box. The stress, coming from the InAs, deforms the cell depending on the InAs distribution: In the first case of a single QD more InAs is placed laterally than vertically. Therefore more stress applies to the unit cell from lateral directions, as indicated by red arrows. The situation changes, if the QDs are stacked. Then the vertical forces can exceed the lateral ones, leading to a reversal of the unit cells aspect ratio. As a result the biaxial strain changes its sign and the the HH and LH bands their energy position.

Two alternatives arise. The first one is to grow QDs with smaller lattice constant. Then the reasoning behind Fig. 6.18 would be reversed. By following this approach, however, it is questionable, whether the desired wavelength, required for telecommunication, can be met.

The second approach employs the strain modifications that result from the close stacking of QDs. The modification of the unit cell shape is schematically shown in Fig. 6.19 for a single QD and a stack of five closely stacked truncated pyramids. In the first case it resembles case (c) of Fig. 6.18 and the last case (b) of the same figure. The large stress, originating from the upper and lower QDs, that impacts on a unit cell in the central QD cannot be compensated any more by the larger (x,y)-extension of this flat QD. Hence, we encounter a flat unit cell with positive biaxial strain and the LH-band on top. The arising local bandstructure is shown in Fig. 6.20: At the position of the outer QDs, the HH-band is still above the LH-band. But already inside the second QD, the HH-band is degenerate with the LH-band finally crossing their position in the central QD. Even more interesting is the LH-band position in between the QDs: It is even deeper than inside the QD, hence, providing no confinement barrier anymore between the QDs for the LH-sub-system.

The electronic structure calculations for these large QD structures consume a lot of computational power. Therefore, we only show the spectrum for one of the structures in Fig. 6.21, showing triple excitonic absorption. For single excitonic absorption we found almost no contribution from the first hole states, being confined at the outermost QD, since their overlap with the strongly coupled electron states is far too small. If more excitons are confined, the Coulomb repulsion between the several hole states comes into play. The positive carriers start to avoid each other, thus, subsequently increasing their overlap with the electron states. The more holes the outermost QDs occupy, the more favorable becomes the stack center with its potential landscape, favoring the LH-dominant hole states. Their contribution to the absorption spectrum of Fig. 6.21 is much larger than the $e \rightarrow HH$ dominant peaks. This dominance finally leads a larger TM-groundstate mode, shown in Fig. 6.21. It should be noted, that in this calculation only first order

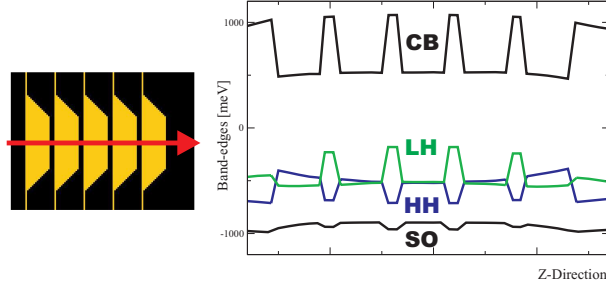


FIGURE 6.20. The position of the local band edges shown for a stack of five truncated pyramids.

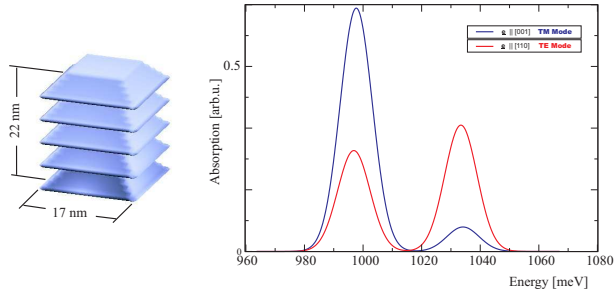


FIGURE 6.21. The tri-excitonic absorption spectrum for a stack of five QDs. The ground state transition achieves dominant TM-mode character.

piezoelectric fields are considered so far. Since these fields can become very large at the outermost QDs, it favors the development of HH-dominant states. By inclusion of second order terms, which are known to compensate the first order terms (see Fig. 6.3), the situation can change drastically and the results can fit more naturally with recent experimental results from Kita *et al.*[15, 132]

6.7. Conclusions

In this section we have investigated the electronic properties in stacks of identical and nonidentical InGaAs/GaAs QDs. We studied the decisive parameters, that determine the onset of electronic coupling: The relative QD size, the inter-QD distance, the symmetry of the overlapping single QD wavefunctions, strain and piezoelectricity. The most important findings are:

(i) For pairs of identical QDs, strain has an asymmetric impact on the individual QDs and renders their confinement inequivalent. Electrons form binding and anti-binding orbitals. Despite the arising splitting, the ground state energy is shifted to higher energies for intermediate dot-dot separation (>20 ML), compared to the respective single dot reference. The hole ground states do not form hybrid orbitals and are located at the lowest QD. Upon smaller inter-dot distance their energy decreases up to 35 meV, with respect to the single QD reference. The resulting larger band-gap is in accordance with experimental results.[117]

(ii) The effect of small size perturbations on the single particle energies and their coupling behavior is studied for pairs of pyramidal QDs. An electric field is applied to tune the resonance energies. A size perturbation of 10 % percent is sufficient to suppress the electron coupling significantly. Small electric field magnitudes (± 22 kV/cm), however, are sufficient to restore the formation of hybrid electron states. The hole ground states are located in the larger dot of the stack at zero field. Higher excited hole states can form coupled states provided their LH-percentage exceeds 28 %. The electric field changes the LH-percentage, e.g. for the p -state.

(iii) In pairs of very differently sized QDs, the s -state electron of the smaller one can be in resonance with the d -shell of the larger one. We investigated the role of symmetry for the interacting states by means of group character theory. If the resonant states belong to the same irreducible representation, they exhibit anti-crossing behavior and form hybrid orbitals, otherwise level crossing is observed.

(iv) We investigated the interrelation of QD-shape, strain, HH/LH ratio of hole states and the optical properties with respect to the TE/TM-mode. The balanced ratio of the latter is decisive for semiconductor optical amplifier. We found, that the biaxial strain changes its sign if the QDs aspect ratio becomes larger than one. As a result, the TM-mode absorption exceeds that of the TE-mode. The same holds for large stacks of closely spaced QDs. Our results are in agreement with measurements of Kita *et al.*[15] for such systems.

Part 3

Other Material Systems

CHAPTER 7

Electronic and optical properties of InAs/InP quantum dots on InP(100) and InP(311)B substrates

One of the biggest challenges for QD-laser-devices is to reach the $1.55\text{ }\mu\text{m}$ (0.8 eV) wavelength used for long-haul telecommunications. In the past the large efforts to push the InGaAs/GaAs system to this wavelength have been hampered by the large strain that accumulates in- and outside the QD- structure during the Stranski-Krastanow growth leading to large increase of the local InAs band gap. Therefore, the most recent developments aimed at the reduction of strain in the system, which can be achieved by introducing metamorphic buffers [21] and thus replacing GaAs by InGaAs as matrix material close to the QD or by turning to InP as a completely different host material, which is employed in our case. Both approaches reduce the lattice mismatch and limit the strain in the QD-system.[22] The smaller lattice mismatch, however, carries the danger of creating too large QDs during the epitaxy resulting in a small QD density and insufficient gain. This can be circumvented by using the (311)B substrate orientation,[23–25] resulting in high QDs densities and low size dispersion permitting the development of low-thresholds QD lasers.[26] The height of the investigated QDs (i.e. the wavelength emission) is well-controlled using the "double-cap procedure".[22] While the experimental impact of the substrate orientation on the QDs optical properties has been already studied by various groups,[133–136] still no complete theoretical study has been performed on these QDs grown on (N11) surfaces, matching the experimental data.[137–143]

In this chapter we theoretically investigate the impact of substrate orientation on the QDs optical properties, using the eight-band $\mathbf{k}\cdot\mathbf{p}$ model including strain and piezoelectric effects, and demonstrate that the use of the (311)B substrate breaks the initial symmetry of the (100) system, thus modifying the optical properties of the QDs. From Atomic Force Microscopy (AFM) measurements and Cross-sectional Scanning Tunneling Microscopy (X-STM), it is shown that a truncated cone shape can be assumed for capped QDs. Furthermore, as the 'double cap' (DC) technique is used to control the QD height and so the wavelength emission,[22] the QD height is used as an adjustable parameter both in experiment and simulation. The electronic and optical properties are thus deduced for InAs/InP QDs on (311)B and (100) substrate orientations. A comparison with experimental results confirms the accuracy of the model. The impact of substrate orientation on optical and electronic properties (ground and excited states transitions) is thus demonstrated. It is then interpreted in terms of different strain contributions to the transition energy for both substrates. The whole calculated optical spectra are then compared for (100) and (311)B substrate orientations, and the impact of the system symmetry (crystal and QD shape) on the anisotropy of the wavefunction in such a substrate, (311)B, is discussed.

7.1. Choice of model QDs

Recent growth developments have allowed to reach high quality InAs/InP QDs.[23–25] As these QDs are flat, their emission wavelength (on the ground state transition) is mainly related to their height, and can thus be controlled by the "double-cap" procedure.[22] From this procedure point of view, it becomes very important to understand the influence of the QD height on the optical transitions. However, the electronic structure of QDs states depends also on the QD shape and lateral extension. In this regard, detailed structural investigations are necessary to describe, in a realistic way, the QD electronic structure. Figure 7.1 (a) represents an Atomic Force Microscopy (AFM) picture of a typical InAs/InP dot on (311)B substrate. The average height for this kind of dots with an average cylindrical symmetry is about 8 nm, while the diameter

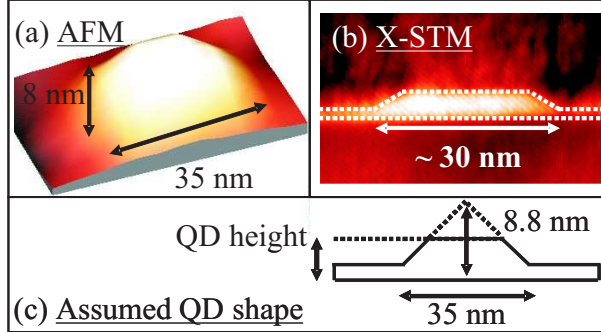


FIGURE 7.1. Structural investigations on InAs/InP QDs on (311)B oriented substrate.[144] From Atomic Force Microscopy (AFM) (a) where the bright areas represent the top of the QD, and from Cross-sectional Scanning Tunneling Microscopy (X-STM) (b) where the bright areas represents the rich-InAs area, a typical truncated cone-shaped QD geometry (c) can be assumed for calculations, where the QD height is a tunable parameter.

is about 35 nm. From this figure, it appears that the QD base resembles more a circle rather than a square. This property is likely to maintain during the capping procedure. Therefore, we used a model QD having a circular base rather than a square base. But from AFM pictures alone, no precise idea about the 3D-shape of the QD can be obtained, as we have to take the tip effect into account, and most importantly the fact that during this measurement, the QDs are uncapped. Thus, X-STM measurements have also been performed on the UHV-cleaved (01 $\overline{1}$) cross-sectional surface. In Fig. 7.1 (b), the X-STM picture of one InAs QD grown on InP (311)B substrate is shown. In this picture, the QD, deposited on InP surface, is simply-capped with quaternary alloy In_{0.8}Ga_{0.2}As_{0.435}P_{0.565}, in order to avoid any intermixing effects (due to As/P exchanges). This figure (2D-view) reveals a truncated, faceted profile of the QD. This figure also shows that the wetting layer has to be taken into account in the calculations as its height is not small compared to the one of the QD. These two structural considerations (combination of 2D-view and 3D-view) allow us to propose a typical geometry for QDs in the calculations, given in Fig. 7.1(c). In the calculations, we assume the QDs to have a truncated faceted profile (from 2D X-STM view) with a circular basis (from 3D AFM view), where the total height of the QD is equal to 8.8 nm (30 monolayers (ML), where 1 ML corresponds 0.29 nm on (100) substrate), the base length is equal to 35 nm. We do not consider any intermixing effects (As/P exchanges) that could occur as a result of the capping procedure. As we don't have any X-STM structural measurement of the in-plane structure of the QD, we assume a cylindrical symmetry (like the one observed by AFM for the uncapped QD), although it is well known that some anisotropy may be present on (311)B substrate and even more on (100) substrate.[145] This choice has been motivated by the sole comparison of the (100) and (311)B substrate effects. Indeed, if we take the [100] direction as a reference, the chosen QD geometry has the highest possible symmetry $C_{\infty v}$ on the (100) substrate. No splitting of excited p -states is predicted so far. When we take the lack of inversion symmetry of the zinc-blende lattice into account, which leads to piezoelectric charges, the symmetry is reduced to C_{2v} .[43] In this case, a weak splitting of excited p -states is expected. Note that the values given in ref. [43] are proposed for InAs/GaAs QDs, where the lattice mismatch is larger, so that the splitting in InAs/InP QDs should be weaker. On (311)B substrate orientation, the initial symmetry of the considered QD is also $C_{\infty v}$. When the atomistic symmetry is taken into account, this symmetry is broken and no degeneracy of the excited states is expected, whatever the QD shape is. The structure loses every rotational symmetry, as the initial $C_{\infty v}$ symmetry of the QD structure is not compatible with the crystal symmetry. This symmetry loss is expected to have drastic consequences on electronic and optical properties of QDs on (311)B substrate. In this context, calculations are performed for truncated cone-shaped InAs/InP QDs of various heights (8ML (1ML ~ 0.29 nm), 10 ML, 12 ML, 16 ML and 30 ML), and for two different wetting layer heights (2 ML and 4 ML).

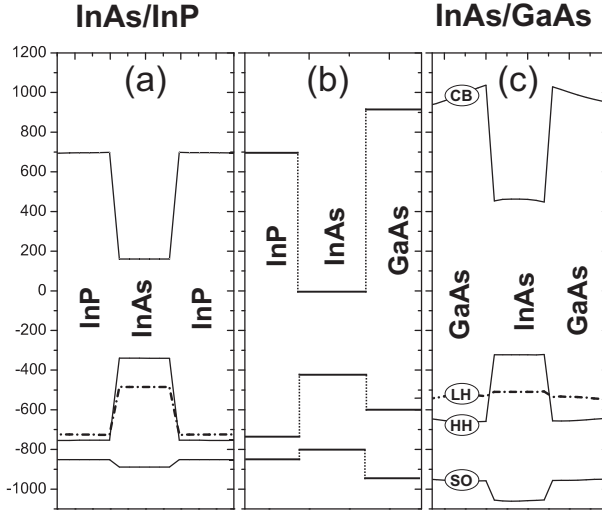


FIGURE 7.2. Vertical scan through the confinement potential for an InAs QD embedded in InP (a) and GaAs (c). In the center (b) the energetic positions of the unstrained band edges for InP and GaAs relative to InAs are given

7.2. Absorption spectra for InAs/InP QDs

7.2.1. Properties of the InAs/InP confinement potential. Deeper insight into the electronic properties can be gained by comparing the InAs/InP QDs considered here to the archetypal InAs/GaAs system. In Fig. 7.2, the confinement potential of the two systems are compared for a truncated pyramid grown on (100) substrate. In the central section (b) the positions of the unstrained band edges relative to InAs are shown. Although the band gap ratio of QDs and matrix material is very similar in both systems, the band offsets are different, reflecting the fact that InAs/GaAs share a common anion whereas InAs/InP share a common cation. In the presence of strain, the band edge energies are altered (see (a) for InAs/InP and (c) for InAs/GaAs) by hydrostatic strain ($\epsilon_H = \epsilon_{xx} + \epsilon_{yy} + \epsilon_{zz}$), mainly affecting the conduction band and by biaxial strain ($\epsilon_B = \epsilon_{xx} + \epsilon_{yy} - 2\epsilon_{zz}$) thus lifting the heavy/light hole degeneracy at the Γ -point. The quantitative effect is much bigger for InAs embedded in GaAs due to the larger lattice mismatch (6.6 % compared to only 3.1 % for InP) and the accompanying increase of hydrostatic strain. The most striking feature is the much smaller (strained) band gap of InAs in InP than in GaAs which opens the door to reach the $1.55 \mu\text{m}$ emission for confined carriers, which is hard to achieve for InAs/GaAs QDs. Since the depth of the electron confinement potential is similar in both systems, one can expect a comparable spectrum for confined electron states, provided the QDs share the same morphological properties. This does not hold for hole states, since the confinement potential for InAs/InP QDs is much deeper and the heavy/light hole splitting is smaller. The material parameters entering the $\mathbf{k}\cdot\mathbf{p}$ -analysis are taken from ref. [3] for InAs and from Ref. [73] for InP.

7.2.2. Predicted absorption spectra of truncated cone-shaped InAs/InP QDs. Excitonic properties are now calculated for self-organized QDs based on a three-dimensional implementation of the eight-band $\mathbf{k}\cdot\mathbf{p}$ model and a configuration interaction scheme thus accounting for the inhomogeneous strain distribution, the piezoelectric effect, inter- and intraband mixing and Coulomb interactions as outlined in chapter 2. Only first order piezoelectric effects are taken into account for two reasons: Compared to InAs/GaAs QDs, the strain encountered in this InAs/InP system here is much smaller due to the smaller lattice mismatch. Therefore, we do not expect second order effects to play a significant role in this system. Moreover, no values for the required additional piezoelectric constants are proposed in the literature so far.

The assumption on shape, size, and composition are guided by structural investigations (see the previous section ??: AFM, and X-STM measurements).

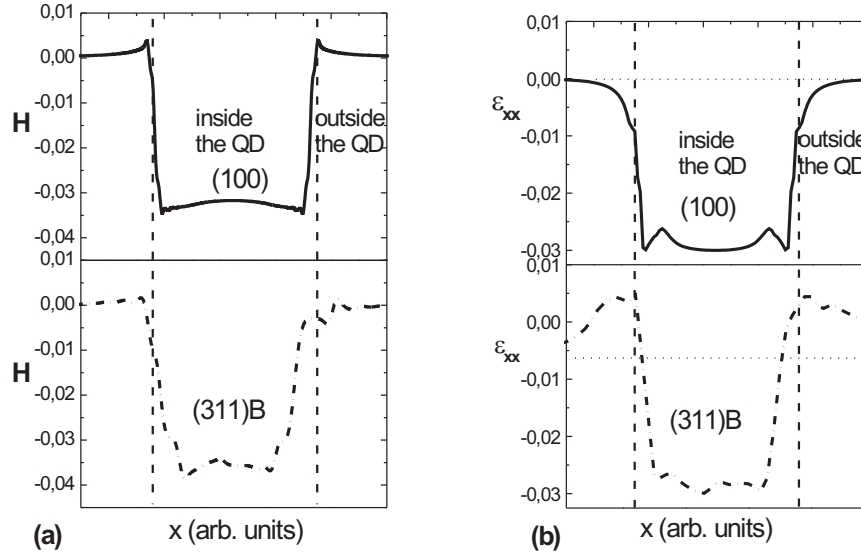


FIGURE 7.3. (a) Hydrostatic strain components (H), $\epsilon_H = \epsilon_{xx} + \epsilon_{yy} + \epsilon_{zz}$, for (100) and (311)B substrates represented in the direction [010] for a truncated cone QD with a 3.5 nm height. The spatial variation (b) of the deformation ϵ_{xx} cannot be compared directly, because of the basis choice. However, the different hydrostatic strain values in the center of the QD for (100) and (311)B substrates are expected to have consequence for the energy levels.

The hydrostatic strain component $\epsilon_H = \epsilon_{xx} + \epsilon_{yy} + \epsilon_{zz}$ is presented on Fig. 7.3 (a) for (100) and (311)B substrate, along the direction [010] for QD with a height of 3.5 nm. Even, if the spatial variation of the hydrostatic strain cannot be compared directly between (100) and (311)B substrates, the values of the hydrostatic strain in the center of the QD are -0.032 and -0.036 respectively for (100) and (311)B substrates. This implies that the hydrostatic strain contributions to the energy levels should be different for (100) and (311)B substrates. Fig. 7.3 (b) shows the ϵ_{xx} component of the deformation tensor, along the [010] direction. While the values of this component in the center of the QD are the same for both substrates orientations, it is clearly visible that a direct comparison of both strain components cannot be performed directly, as the (311)B structure is rotated in the calculation box. Indeed, the deformation tensor represented here in the $X = [010]$ and $Y = [001]$ basis should be represented into the $X' = [01\bar{1}]$ and $Y' = [\bar{2}33]$ in the case of the (311)B substrate. As a consequence, positive values of ϵ_{xx} are calculated at the edge of the QD for the (311)B substrate orientation on Fig. 7.3 (b). Although the strain calculation themselves are not central to this chapter, the strain contributions to the single-particle energies will be analyzed, as they can be compared directly without any rotation of the system.

By solving the Schrödinger equation the single-particle wavefunctions are obtained. The parameters entering this Hamiltonian are based on experimental values for the required bulk material Γ -point band structure parameters and taken from Ref. [73]. Free adjustable parameters are not present in our model. Figure 7.4 displays the first three electron and hole wavefunctions (70 % isosurface) for both, the (100) and the (311)B substrate, for illustration. The symbols E1 and H1 stands for 1Se and 1Sh states (i.e. with an in-plane "s-like" symmetry for electrons and holes). E2, E3, H2, H3 stands for 1Pe and 1Ph states (i.e. with an in-plane "p-like" symmetry for electrons and holes). The terms "s-like" and "p-like" are used here, in order to make the parallel with the usual notation of states in the cylindrical symmetry.[143]

By using the procedure, outlined in chapter 2, a good agreement between experiment and theory still needs to be demonstrated. In order to check the validity of the used model, the eight-band $k \cdot p$ ground transitions are to be compared to those determined by photoluminescence experiments performed on InAs/InP

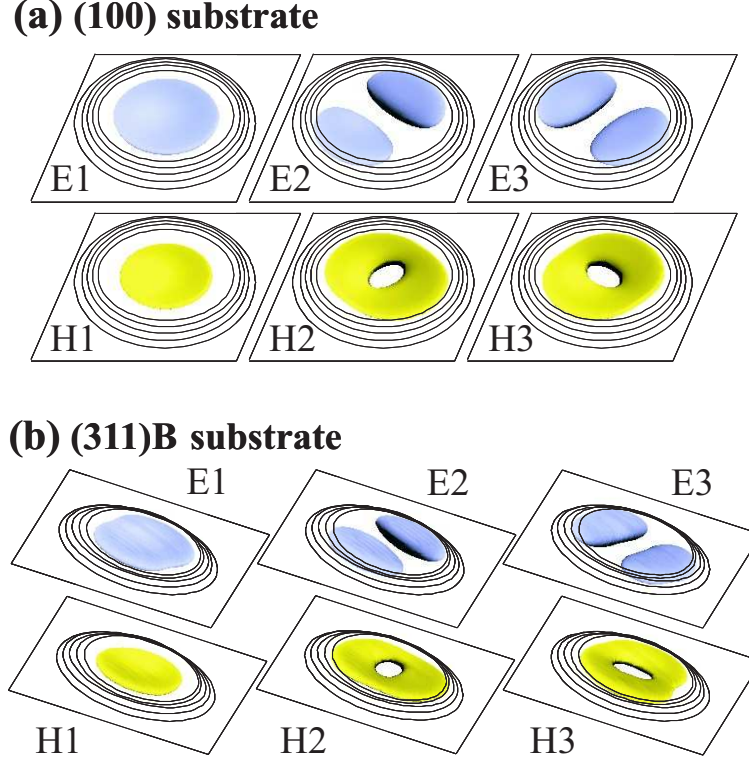


FIGURE 7.4. Wavefunctions representations for electrons and holes for the first QDs states on (100) substrate orientation (a) and on (311)B substrate orientation (b), with a QD height of 2.93 nm. E1, E2 and E3 stands for electronic states 1Se and 1Pe. H1, H2 and H3 stands for hole states 1Sh and 1Ph. The (311)B substrate induces an anisotropy of the wavefunction.

(311)B QDs (see [144]). Figure 7.5 represents the 1Se-1Sh ground transition energies measured (triangles), calculated by one-band $\mathbf{k}\cdot\mathbf{p}$ approximation in ref. [143] (dashed line), and calculated by the eight-band $\mathbf{k}\cdot\mathbf{p}$ method in this work (straight line) as a function of QD height. The photoluminescence experiments were carried out at 4.2 K in a He bath cryostat. The photoluminescence is excited using a cw Krypton laser (647 nm wavelength) at 1 mW, in order to avoid any state filling at high energy. The samples are designed to have different first capping layer heights, thus having different InAs/InP QDs heights (2 nm, 3 nm, 4 nm, 5 nm), using the double-cap procedure.[22] Hence, the comparison between experiment, and calculations can be performed using the ground state transition energy as criterion. While the experimental energies are determined with high accuracy, the height of our QDs, reported on the horizontal scale of Fig. 7.5, is an estimate of the real QD height. Indeed, in first approximation, the experimental QD height proposed in Fig. 7.5 is set equal to the deposited height of InP in the first step of the double cap procedure. However, from the analysis of the growth mechanisms when the DC procedure is used, it is commonly accepted that the deposited height of InP during the first cap is a little bit larger (2ML) than the effective height of the QD.[22] Therefore, the eight-band $\mathbf{k}\cdot\mathbf{p}$ calculations are in good agreement with experimental data, provided a simple translation of QD height along the horizontal scale can be performed (arrows on Fig. 7.5). Figure 7.5 also shows the limitation of a simple model like the one-band approximation especially for higher QDs,[143] and justifies the use of the eight-band $\mathbf{k}\cdot\mathbf{p}$ model. Figure 7.6 displays calculated exciton absorption spectra for QDs of different height on (100) substrate, as an illustration of the output of the calculations (the WL height in this case is taken equal to 4 ML). Calculated exciton absorption spectra are plotted with a polarization along the $[01\bar{1}]$ axis, as this axis is an QDs in-plane axis for both substrates. In this case, the exciton binding energy is on the average equal to 15.5 meV. The spectra show a blueshift of 135 meV for the ground state transition energy upon reducing the QD height from a pointed cone-shaped QD down to 8 ML truncated-one. It is also seen on Fig. 7.6 that excited states are energetically closer for flat quantum dots compared to the full cone.

This is explained by the different aspect ratio of considered QDs. Indeed, in the case of flat QDs, the weak lateral confinement has only few consequences on the p -state energy shift, while the strong vertical confinement has a large impact on the ground s -state energy increase. Ground and excited state transitions are thus energetically closer for flat QDs than for the full cone QD. The spectrum calculated with height-band $\mathbf{k} \cdot \mathbf{p}$ theory on Fig. 7.6 provides much more richness compared to those found with previous calculations.[143] In this regard, a comparison between (311)B QDs and (100) QDs absorption spectra is to be made.

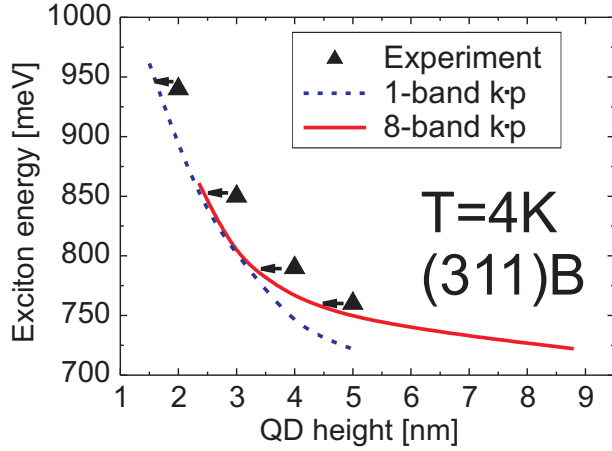


FIGURE 7.5. Predicted (solid line for eight-band $\mathbf{k} \cdot \mathbf{p}$, dashed line for one-band $\mathbf{k} \cdot \mathbf{p}$ [ref. [143]]) and observed (solid symbols) energies of the ground exciton transition in truncated cone-shaped InAs/InP (311)B QDs as a function of QD height. The eight-band $\mathbf{k} \cdot \mathbf{p}$ predicted transitions have a better agreement with the experimental data than the single-band $\mathbf{k} \cdot \mathbf{p}$ predicted transitions.

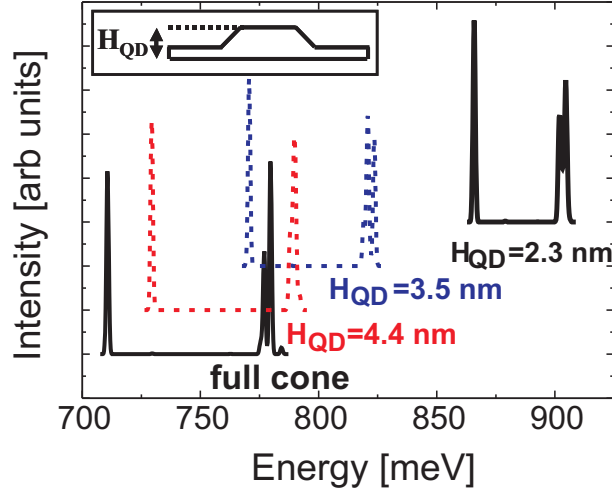


FIGURE 7.6. Excitonic absorption spectra calculated in an eight- band $\mathbf{k} \cdot \mathbf{p}$ model for InAs/InP (100) QDs, as a function of the QD height for a polarization along the $[01\bar{1}]$ direction. A truncated cone-shaped QD with a base length of 35 nm was assumed.

7.3. Impact of substrate orientation on the QDs optical properties

7.3.1. Ground state transition on (100) and (311)B substrates. In Fig. 7.7 the exciton ground state (X_0) transition energy is plotted versus the QD-height for the two different substrate orientations (100) and (311)B whereof we can derive two main results: (1) The smaller the QD height is, the larger becomes the

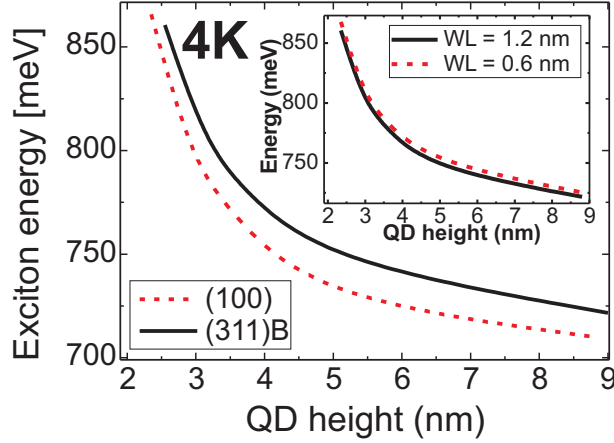


FIGURE 7.7. Comparison between calculated ground exciton transition energy in InAs/InP (311)B-QDs (solid line) and InAs/InP (100) QDs (dotted line), as a function of QD height. The difference between both curves is mainly related to hydrostatic strain. The inset shows the weak influence of the WL dimension (1.2 nm : solid line, 0.6 nm : dashed line) on ground exciton transitions in InAs/InP (311)B-QDs.

X_0 -transition energy, also known as the quantum-size effect [106]. (2) Whatever the QD height is, the X_0 -transition energy is always larger for (311)B grown QDs than for the (100) grown QDs. To understand this last point we have to analyze (a) the electron- and hole ground state energies and (b) the X_0 -binding energy.

(a) *The single particle energies.* The electron groundstate energy can be separated into the components

$$E = E_{\text{quant}} + E_{\text{conf}}^0 + E_{\text{hydro}}^{\text{strain}} + E_{\text{piezo}} + E_{\Delta} \quad ,$$

where E_{quant} represents the kinetic part of the Hamiltonian,

$$E_{\text{hydro}} = \langle \psi | a_c(\epsilon_{xx} + \epsilon_{yy} + \epsilon_{zz}) | \psi \rangle$$

is the energy shift, induced by hydrostatic strain with a_c being the conduction band deformation potential, $E_{\text{piezo}} = \langle \psi | V_{\text{piezo}} | \psi \rangle$ the energy shift induced by the internal piezoelectric field, and $E_{\text{conf}}^0 = \langle \psi | V_{\text{conf}} | \psi \rangle$ is the confinement energy related to the unstrained position of the local conduction band. This energy becomes minimal if the wavefunction is completely localized inside the QD and increases the more it spreads into the barrier material. Hence, it is a measure for the "spreading-out" of the wavefunction in question. E_{Δ} , not being quantified here, contains the energy contributions induced by the non-diagonal components of the Hamiltonian related to the strain tensor (tetragonal and shear deformation) and coupling to the valence band. For hole states an additional term $E_{\text{baxial}}^{\text{strain}} = \langle \psi | b(\epsilon_{xx} + \epsilon_{yy} - 2\epsilon_{zz}) | \psi \rangle$ appears reflecting the influence of the biaxial strain with b being the shear deformation potential. The fact that for all investigated QDs the transition energy is higher if the dots are placed on (311)B substrate than on (100) substrate is not surprising since the hydrostatic strain energy shift is larger for (311)B grown QDs, $(E_{\text{hydro}}(E_1))(311) > (E_{\text{hydro}}(E_1))(100)$, as it has already been demonstrated in Miska *et al.* [143]. The difference of this contribution in our calculations is found to be 10 meV for tall (30 ML) and 15 meV for flat (8 ML) QDs (see Fig. 7.8(c)). Resulting from the larger strain inside the (311)B-QDs, the conduction band offset becomes smaller and the wavefunction "spread-out" becomes larger. Therefore, the confinement energy related to the unstrained local CB $E_{\text{conf}}^0(e_0)$ increases and the quantization energy $E_{\text{quant}}(E_1)$ decreases for (311)B-QDs compared to their (100) grown counterparts as can be seen in Fig. 7.8(a) and (b). For the (311)B there are some minor contributions from the piezoelectric potential even for the electron ground state which are not present in the (100) case. We find an energy drop of 3.2 meV for the tallest and 0.4 meV for the flattest (311)B-QD. This is due to the fact that in this case the piezoelectric potential (see Fig. 7.9(b)) breaks any symmetry that might be present from the QD shape, thus pulling the electron states

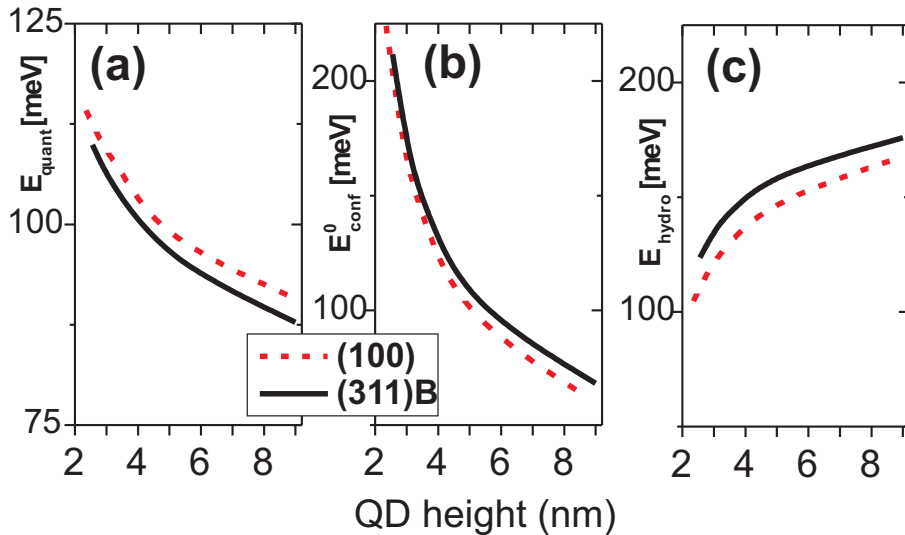


FIGURE 7.8. The electron groundstate energy for different QD heights decomposed into the quantization energy E_{quant} (a), confinement energy E_{conf}^0 (b) and the energy shift induced by hydrostatic strain E_{hydro} (c) the two substrate orientations (100) and (311)B. E_{piezo} is not shown since it is close to zero for the electron groundstate.

to one QD side and the hole states to the other. In the (100) system instead the carriers are getting distorted but their (x,y) component of the wave function barycenter still coincides with that of the QD-structure.

(b) *The exciton-binding energy.* The X_0 -binding energy is foremost a function of the extent of the electron and hole wave function and their mutual position. Therefore, since the electron groundstates of the (311)B-QDs exhibit a "spread-out", visible in the smaller quantization energy $E_{\text{quant}}(E_1)$, and as the barycenter of ψ_{E_1} and ψ_{H_1} are slightly drawn apart by the particular piezoelectric field, we find a smaller X_0 -binding energy for these (311)B-QDs. The difference $\Delta E_{X_0} = E_{X_0}(100) - E_{X_0}(311)$ to the (100)-QDs, however, is very small in the order of 2 meV, which is not enough to compensate the blue-shift caused by the larger hydrostatic strain of the (311)B-QD system. The exciton energy difference between both substrates given in Ref. [143] is larger than those calculated in this work. In this reference, however, the influence of E_{piezo} and possible variations of E_{quant} (due to effective mass variations) have not been taken into account. In this regard, the part of the Hamiltonian related to the strain tensor including hydrostatic and shear deformations plays the main role in explaining the difference between (311)B and (100) substrates for small QDs. As the difference between shear/tetragonal and hydrostatic deformations on (100) and (311)B has already been demonstrated,[146] and as the impact of these deformations on electronic properties has been already observed,[137] we propose to interpret the difference between (311)B and (100) for several QDs heights as a direct consequence of shear/tetragonal and hydrostatic deformations difference on these substrates. As an illustration, the energy shift induced by the piezoelectric field on (311)B has also been demonstrated experimentally on (311)B-QDs.[136] In summary, the difference observed for large QDs on (311)B and (100) substrate is mainly due to the hydrostatic strain.

The influence of the WL thickness on QD ground state is also studied in Fig. 7.7 (inset). In a previous work, it was shown that the WL thickness is expected to play a role for the electronic structure of QDs.[24] The QD ground state transition is plotted for two different structures with a WL thickness of 0.6 (2 ML) and 1.2 nm (4 ML), respectively. As expected, the QD groundstate transition energy for the largest WL thickness is smaller than for the smallest WL thickness. This is explained by the difference between ground state wavefunction penetration in the WL.[24]

The next results come from calculations made on structures with a WL thickness of 1.2 nm. This choice is motivated by the measured WL thickness by X-STM, which is around 1 nm.

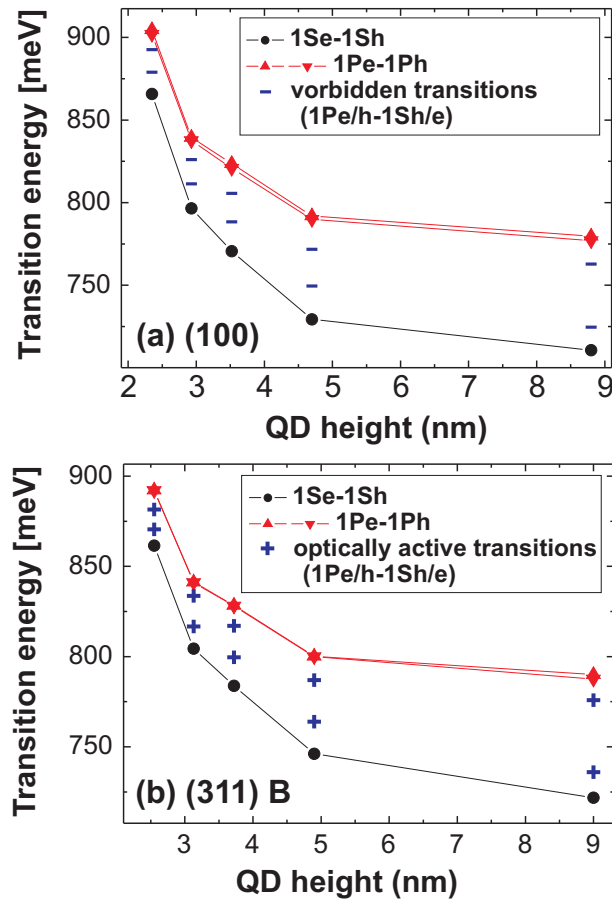


FIGURE 7.9. Comparison between calculated transitions in InAs/InP (100) QDs (a) and InAs/InP (311)B QDs (b), as a function of QD height. On (311) B substrate, second-order transitions (+) become optically active.

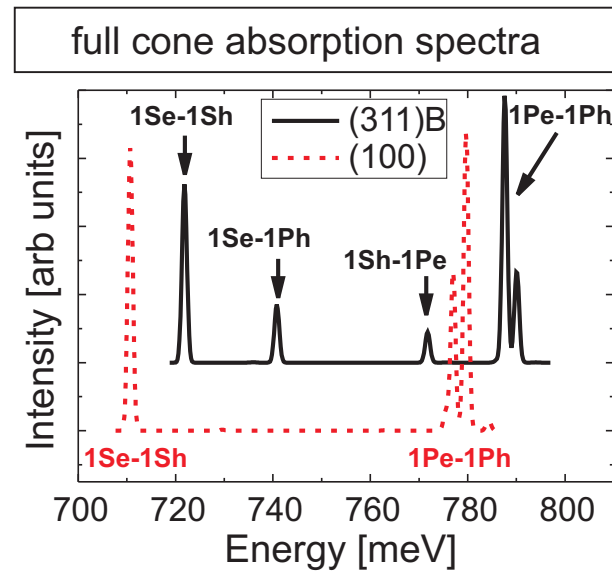


FIGURE 7.10. Comparison between full-cone (30 ML) QDs absorption spectra for the two substrates orientations (311)B and (100).

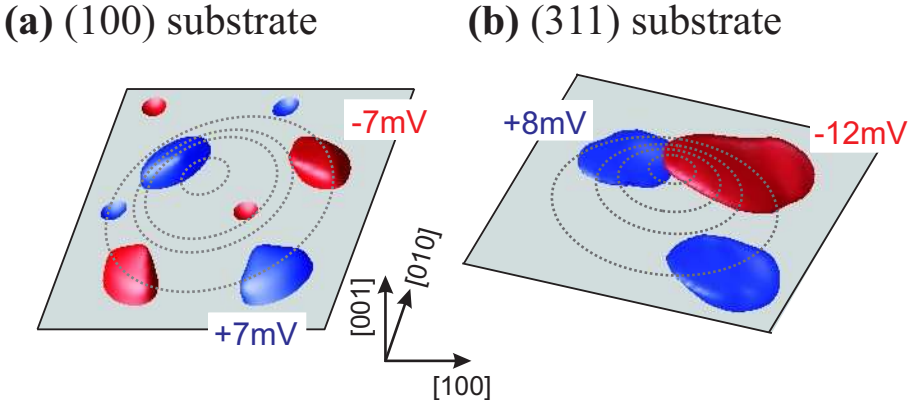


FIGURE 7.11. Orientation and appearance of the piezoelectric potential (isosurface plot) for QDs grown on (100) and on (311)*B* substrate.

7.3.2. QDs Absorption spectra on (100) and (311)*B* substrates. The complete analysis for the whole absorption spectrum can be performed on (100) and (311)*B* substrates. In Fig. 7.10 the full-cone (30 ML) absorption spectra for QDs grown on the two different substrates are compared. Fig. 7.9 (a) and (b) represent excitonic transition energies for both substrate orientations versus QD height. These transitions are derived from absorption spectra polarized along the $[01\bar{1}]$ direction (as the one of the Fig. 7.10), which is an in-QDs-plane direction for both substrates.

Despite the different substrate orientations, the energy and the splitting of the *p*-like states transitions foremost depend on the QD size and hardly on the orientation of the substrate. The splitting of these transitions, ΔE_p , is related to the presence of the piezoelectric field,[3] which lifts the degeneracy of the electron and hole *p*-states even in the presence of the structural $C_{\infty v}$ symmetry. Despite the fact that the magnitude of ΔE_p is very similar for both substrate orientations, the piezoelectric field itself is very different in its strength and symmetry as can be seen in Fig. 7.11: for the (100) QD the lobe of the positive and negative isosurface are congruent and can be transformed into each other just by a rotation of $\pi/2$, which is in striking contrast to the (311)*B*-QD. This one exhibits no apparent symmetry and, moreover, the maxima of the positive and the negative part of the potential are not even equal: for the QD shown in Fig. 7.11(b) the piezoelectric potential ranges from $\min(V_{\text{piezo}}) = -25.2$ mV to $\max(V_{\text{piezo}}) = 12.8$ mV in contrast to ± 8.5 mV for the (100)-QD in part (a) of the figure. In both cases the *p*-channel-splitting is also a function of QD size, and is related to the size dependence of the piezoelectric field in QDs. The latter effect is well known for (100)-QDs for a longer time,[3] and holds also for (311)*B*-QD as can be seen from the values listed in table 1. The much larger magnitude of the piezoelectric field in (311)*B*-QDs however is not reflected in the *p*-channel-splitting since the former is not symmetry adapted to the *p*-states as it is tilted against the substrate orientation. Another difference between the two substrates which is linked to the orientation of the piezoelectric field appears in Fig. 7.10. While on the (100) substrate [Fig. 7.9 (a)] the absorption spectra are mainly constituted of first order-transitions (1Se-1Sh, 1Pe-1Ph), the (311)*B* absorption spectra [Fig. 7.9 (b)] also reveal second order-transitions (1Se-1Ph, 1Pe-1Sh), as it is illustrated in Fig. 7.8 for the QD with a 30 ML height (full-cone). The (311)*B* substrate is thus expected to activate these second-order transitions, that are usually considered as "forbidden" transitions without excitonic effects in $C_{\infty v}$. For QDs having at least C_{2v} symmetry the optical matrix element between the electron *p*-state, ψ_{e2} , and the hole *s*-state, ψ_{h1} , $\langle \psi_{e1} | \mathbf{p} | \psi_{h0} \rangle$ (almost) disappear since the envelopes belong to different irreducible representations of the symmetry group. The term "almost" is related to the fact that even the hole groundstate carries some light hole character which can add new symmetry properties to the envelope rendering the whole wave function a reducible representation. For the (311)*B*-QD the barycenter of the hole groundstate is pulled to one QD-side and that of the electron *p*-state to the other side. Therefore, the matrix element $\langle \psi_{e1} | \mathbf{p} | \psi_{h0} \rangle$ cannot vanish for symmetry reasons and the transitions (1Se-1Ph, 1Pe-1Sh) are not forbidden anymore and become

QD height [nm]	Substrate orientation	Min(V_{piezo})[mV]	Max(V_{piezo})[mV]
2.3	(100)	-2.5	2.5
2.5	(311) B	-10.6	7.9
8.8	(100)	-8.5	8.5
9.0	(311) B	-25.2	12.8

TABLE 1. The strength of the (first order) piezoelectric potential as a function of QD size and substrate orientation.

activated. However, the flatter the QDs and, hence, the smaller piezoelectric field become, the weaker these transitions are.

In conclusion, all the observed differences between the two substrates can be linked to the lack of symmetry on the (311) B substrate, which results in larger shear strain becoming manifests through the piezoelectric field.

7.3.3. Discussion. Indeed, the optically activated "forbidden" transitions for the (311) B QDs raise the problem of symmetry in this system. The problem of the impact of symmetry on calculations and predicted optical properties in QDs have been already studied by Bester *et al.*[43] However, in this reference, QDs are considered only on the (100) substrate orientation. In our case, we have shown that taking into account the crystal symmetry leads to consider a C_{2v} symmetry for a QD grown on (100) substrate while for the (311) B substrate there are no symmetry elements present anymore. The main consequence of this loss of symmetry is the presence of a high value for shear strain and tetragonal deformation.[146] The wavefunction is then more sensible to the crystal orientation on (311) B than on (100) substrate, and especially for small QDs where the shear and tetragonal deformations play a very important role (the strain relaxation is less efficient). In this case, the wavefunction becomes clearly anisotropic, and depends a lot on the crystal orientation (whatever the QD shape is in this (311) system). This loss of symmetry thus has drastic consequences on the wavefunction symmetries. In case of the C_{2v} symmetry considered for the (100) substrate, Eigenstates calculated from the eight-band $\mathbf{k} \cdot \mathbf{p}$ Hamiltonian have nearly the 1S, and 1P symmetries. A very weak splitting of p -states is observed, as the C_{4v} to C_{2v} reduction of symmetry is small, and only has a few consequences on the calculation of energy levels. In this case, p -states are elongated along the [011] and [01 $\bar{1}$] directions, respectively. For the (311) B substrate, the orbitals do not show such a symmetry anymore. Thus, the ground state is not a pure s -state, and the excited states are not pure p -states anymore. They are then aligned along the [01 $\bar{1}$] and [$\bar{2}33$] directions, respectively, with a strong difference between both directions. The difference between the two directions is large, as we are far from the C_{4v} symmetry, unlike to the (100) substrate. Thus, the wavefunction in such a low-symmetrical configuration becomes much more sensible to the crystal symmetry, and less sensible to QD symmetry.

7.4. Conclusions

The impact of substrate orientation on the electronic and optical properties of QDs has been studied theoretically in this chapter. Based on AFM and X-STM measurements, it has been demonstrated that eight-band $\mathbf{k} \cdot \mathbf{p}$ calculations performed on truncated conical shape QDs show a good agreement with photoluminescence measurements performed on (311) B substrate, for various QDs heights. Next, it was found that QDs, grown on (311) B and (100) substrate, exhibit different excitonic optical signatures mainly for two reasons: First, the larger hydrostatic strain observed for the (311) B -QDs elevates the electron energies thus causing an overall increase of the excitonic transition energy. Second, the way the piezoelectric field acts on both substrates is fundamentally different in view of its strength and its orientation. This alters the symmetry properties of the confinement potential and induces the optical activation of second order transitions on the (311) B substrate. Therefore for this substrate orientation, the electronic and optical properties

are considered to be less sensible to the QD geometry, and more sensible to the crystal orientation, than on (100) substrate orientation.

CHAPTER 8

Inverted GaAs/Al_xGa_{1-x}As Quantum Dots

Recently, unstrained GaAs/Al_xGa_{1-x}As QDs were fabricated through an ingenious multistep approach based on a combination of hierarchical self-assembly and *in situ* etching.[27] Photoluminescence (PL) of an ensemble of such QDs revealed an appreciably smaller inhomogeneous broadening, in the range between 8 to 15 meV depending on the growth conditions, indicating a good size homogeneity. The QDs have a typical lateral size of about 60 nm and a thickness of ca. 6 nm.

Due to the nonexistence of strain and reduced uncertainties in the size and shape, such QDs represent an ideal test case for electronic structure models. In Ref. [27] an eight-band $\mathbf{k}\cdot\mathbf{p}$ model was successfully applied to describe the zero-field PL and single dot spectra. The zero-field PL measurements were subsequently extended to magnetic field up to 50 T by Schildermans *et al.* [31] and a single-band model, modified to include conduction band non-parabolicity,[147] was implemented to describe the magnetic field dependence.[32]

Based on eight-band $\mathbf{k}\cdot\mathbf{p}$ theory,[3] the previous theoretical studies are extended here, by taking into account magnetic field effects like the Zeeman splitting and the diamagnetic shift.[28] Single particle states, exciton binding energies and the diamagnetic shift are calculated for magnetic fields applied in growth direction, $\mathbf{B} \parallel [001]$, as well as in lateral direction, $\mathbf{B} \parallel [100]$. The calculations are based on a realistic confinement potential, which is derived from high resolution STM data taken from Ref. [27]. Recent cross section scanning tunneling microscopy (X-STM) experiments demonstrate, that the interfaces between GaAs and AlGaAs layers are not abrupt [29] as previously observed for quantum wells.[30] Since the size and shape of the dots are known, this previously not discussed effect [31, 32] of interface roughness on the electronic properties is investigated in detail.

This chapter is organized as follows. The theoretical approach is presented in Sec. 8.1. The influence of interface intermixing on the transition energy is discussed in Sec. 8.2. Sec. 8.3.1 contains an analysis of the electron, hole and exciton energies as a function of the magnetic field treating interface roughness as a variable. In Sec. 8.3.2 we compare our results with available experimental data. Finally, in Sec. 8.4 we discuss the role of conduction band non-parabolicity induced by higher conduction bands. The results and conclusions are summarized in Sec. 8.5.

8.1. Choice of the model QDs

The unique fabrication process used in Ref. [27] made it possible to extract the QD structure with great detail: Prior to the final step of QD deposition the surface profile (see Fig. 8.1 (a), red dotted line) has been scanned using STM while preserving the ultra high vacuum conditions during epitaxy. The shape of the resulting QD is determined by this pattern and taken as the origin of our primary model QD. Next, a series of model QDs is derived from the primary one based on a systematic variation of Fickian diffusion induced interface roughness (see Fig. 8.2). The parameter N describes the degree of intermixing (N=0: no intermixing; N=9: strong intermixing). The parameter N is actually the number of smoothing steps at the interface. One smoothing step at one point of the grid describing the structure is taken as average value of the material parameters of the structure on the neighboring points of the grid.

8.1.1. Method of calculation. The single particle energies of our model QDs are calculated using eight-band $\mathbf{k}\cdot\mathbf{p}$ theory,[3, 33] The magnetic field is incorporated through standard Peierls substitution [148] in the wave-vector and Zeeman energy term.[28] The parameters used for our structure are based on Γ -point band structure parameters and are given in Table 1.

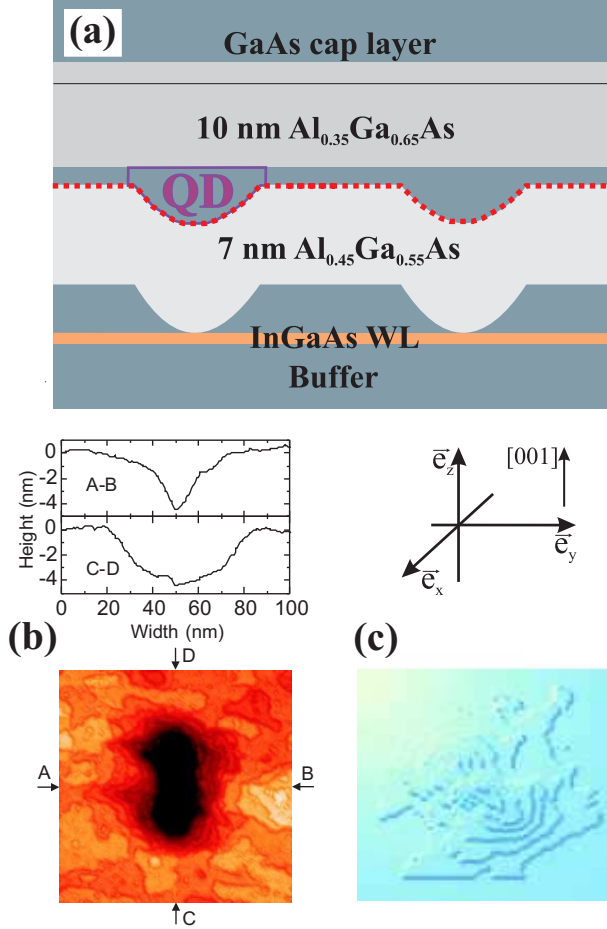


FIGURE 8.1. (a) Schematic sample structure of unstrained GaAs/AlGaAs quantum dots. The structure of the implemented model QD (c) is derived from STM measurements (b) taken from Ref. [27]. The red dotted line in (a) indicates the position where the STM picture is taken from.

The excitonic states are calculated using the configuration interaction method. The two particle exciton Hamiltonian is expanded into a basis of antisymmetrized products of single particle wavefunctions, thus accounting for direct Coulomb interaction and exchange. Correlation effects are accounted for by expanding the basis to include excited-state-configurations.[66] The Coulomb and exchange matrix elements needed for the CI calculation are computed numerically from 6 electron and 6 hole single particle orbitals and are screened using different dielectric constants for GaAs and AlGaAs. Absorption is calculated by Fermi's golden rule applied to CI states. It is important to stress that no adjustable parameters are present in this model.

8.1.2. Experimental reference. The experiments, which we are referring to throughout this chapter, were performed on an ensemble of QDs. When we compare our findings with the experimental results, we consider our model QD as representative for the ensemble of QDs. The latter is motivated by the unusual narrow photoluminescence broadening which points at an extremely homogeneous QD-ensemble.

8.2. Influence of interface intermixing on the optical properties

In a simplified picture, the carrier confinement in (unstrained) GaAs/Al_xGa_{1-x}As QDs is only a function of the dot size and shape, where the conduction and valence band offsets are taken from those of the bulk materials. However during the growth process Al-Ga intermixing at the interface is likely to occur leading to changes of the aluminium/gallium content at the heterojunctions. Recently obtained cross-section STM images of GaAs/Al_xGa_{1-x}As QDs support this assumption, suggesting that interfaces of GaAs and AlGaAs

TABLE 1. Material parameters used for the electronic structure calculations, taken from Ref. [73].

Quantity	Unit	GaAs	AlAs	$\text{Al}_x\text{Ga}_{1-x}\text{As}$
a	A	5.65	5.65	linear
E_0	meV	1518.0	3060.0	$1518 + 1542x + x(x-1)(689x - 18.5)$
E'_v	meV	-6920.0	-7377.0	$-6920 - 433x - 24x^2$
Δ_0	meV	340.0	280.0	$340 - 131x + 71x^2$
E_p	meV	25500.0	21100.0	$(1.132 + 0.758x) \frac{1-m_e}{m_e} \frac{3E_0(E_0+\Delta_0)}{3E_0+2\Delta_0}$
m_e	m_0	0.067	0.22	linear
γ_1		7.1	4.04	$1/[(1-x)/7.1 + x/4.04]$
γ_2		2.4	0.78	$1/[(1-x)/2.4 + x/0.78]$
γ_3		2.91	1.57	$1/[(1-x)/2.91 + x/1.57]$
ϵ_s		13.18	10.06	linear
κ		1.28	0.12	linear

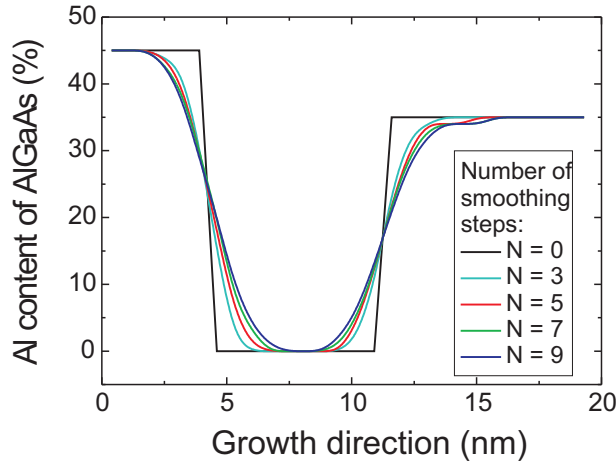


FIGURE 8.2. Vertical scan through the center of the model structures. The aluminium content is varied as a function of intermixing steps (N).

layers are not abrupt.[29, 30] Here, we investigate the consequences of such non-abrupt interfaces on the optical properties by treating the degree of interface intermixing as a variable.

In Fig. 8.2 a vertical scan through the center of the model structures is shown for different values of N, a quantity which parametrizes the degree of interface intermixing. The case N = 0 corresponds to the ideal case of abrupt interfaces and N = 9 to the case of strong interface intermixing. The corresponding local conduction and valence bands are shown in Fig. 8.3 (a) and (c).

8.2.1. Single-particle energies. The variation of the first three electron and hole energy levels with the number of intermixing steps is shown in Fig. 8.4. Two main results can be derived from this figure:

First, Al-Ga intermixing leads to an increase of electron and hole energies and, therefore, to larger interband transition energies. Second, the electron intraband energies are almost unaffected by the interface roughening. The situation is similar for the hole intraband energies, except for N larger than 7, where the hole intraband energies slightly differ from those for smaller N. This behavior can be attributed to the increased confinement, which leads to an enhanced valence band mixing. Fig. 8.3 (b) and (d) show the lateral and vertical extent of the electron and hole groundstate for the abrupt interface (N = 0) and for the largest considered degree of intermixing (N = 9): In both cases the wavefunctions are stronger localized for N = 9. Although the effective size of the quantum dot increases with increasing N, the decrease of the Al content with N is the dominant effect, which leads to the increased confinement for both, electron and hole states. This result is different from the one reported in Ref. [67] for small InAs/GaAs QDs, where it was

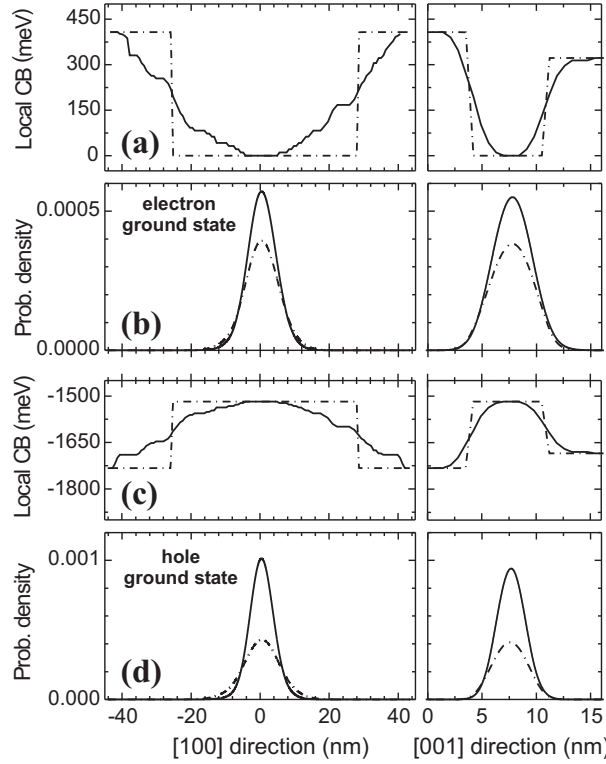


FIGURE 8.3. Lateral (left) and vertical (right) scan through the local conduction (a) and valence (c) band edges of the model QD for $N=0$ (nonintermixed dashed) and $N=9$ (strongly intermixed). The respective electron and hole wavefunctions are shown in (b) and (d), respectively. The lateral scans through the confinement potential and the probability density are taken at a vertical position 1 nm below the GaAs quantum well (average of the z-component of the wavefunctions barycenter). Since the potential width is determined at this upper z-position it appears large compared to the lateral wavefunction extent. The step-like lateral confinement potential after annealing (a and c) originates from a combination of the terrace like QD structure and the applied smoothing procedure.

found, that both carrier types tend to increase their wavefunction extent upon annealing. The main reason for such a different behavior of electron/hole wavefunction can be found in the ratio between average QD size and electron/hole Bohr radius, which is larger than one here and smaller than one in the case reported in Ref. [67].

8.2.2. Excitonic properties. As can be seen from Fig. 8.5 (a), a change in the sharpness of the interfaces sensitively affects the exciton energy. The larger N is, the larger is the exciton energy. We have already seen that the single particle energies increase (Fig. 8.4) for higher values of N . The increase of electron and hole localization for larger interface intermixing, shown in Figs. 8.3 (b) and (d), is also reflected by an increase of the exciton binding energy as illustrated in Fig. 8.5 (b). Therefore, the increase of exciton energy upon interface intermixing is a result of the increased single-particle energies resulting in a stronger wavefunction localization. Fig. 8.6 finally shows the calculated excitonic absorption spectra as a function of N .

A comparison to measured single-QD PL spectra [27] yields a very good agreement of for an intermixing value of $N=3$. Therefore the variation of the spectra with N in Fig. 8.6 can be understood as a guide to determine the degree of interface intermixing. With increasing N a blue shift of the whole spectrum occurs (37 meV between $N=0$ and $N=9$), whereas the distances between the peaks remain approximately the same.

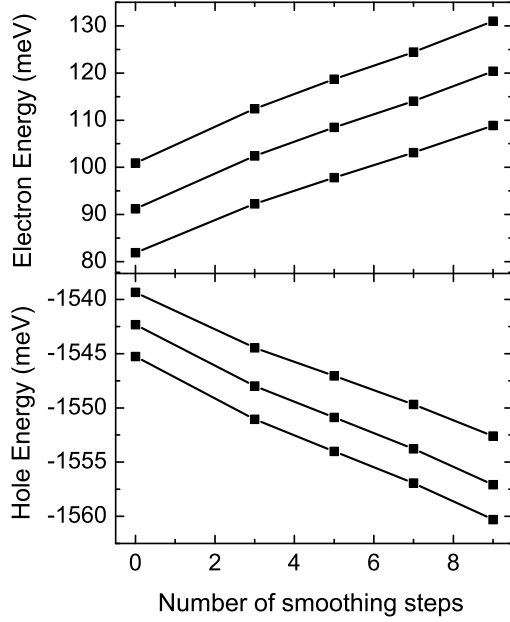


FIGURE 8.4. The variation of the first three electron and hole energy levels as a function of N .

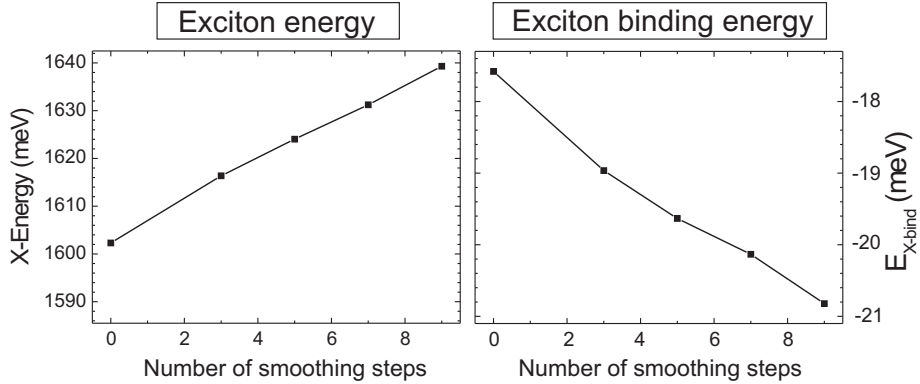


FIGURE 8.5. Exciton energy as a function of the number of smoothing steps. Inset shows the exciton binding energy as it varies with the number of smoothing steps.

8.2.3. Comparison to single-QD PLE results. In this paragraph the results for $N=9$ are compared in more detail to single-QD PL and PLE measurements, performed by A. Rastelli and S. Stufller [27]. In Fig. 8.7, the measured peaks are labeled by X, for the transition of the ground state exciton, and A-E for the excited state absorption lines. In panel (b) of the same figure, the calculated absorption spectra are shown and the leading single-particle contributions are indicated. We see that the position of the peaks X and A-E are well reproduced by the calculation. By comparing the measured and the calculated spectra, the corresponding peaks can be clearly assigned to each other. The corresponding wavefunctions are shown in panel (c); arrows mark the identified transitions.

This comparison marks a new level in the relation of QD-spectroscopy and theory, and it constitutes a true challenge to the employed model. So far, it was always possible to blame insufficient structural data for the lack of agreement, or the data have been adapted accordingly, or the models contain adjustable parameter that can be used to fit the experimental results. Here, the structure is almost unambiguously known from STM and X-STM data. The only employed 'fitting' parameter is N , the degree of interface roughening. To the authors knowledge, this is the first successful peak identification of single-QD PLE results. Our earlier

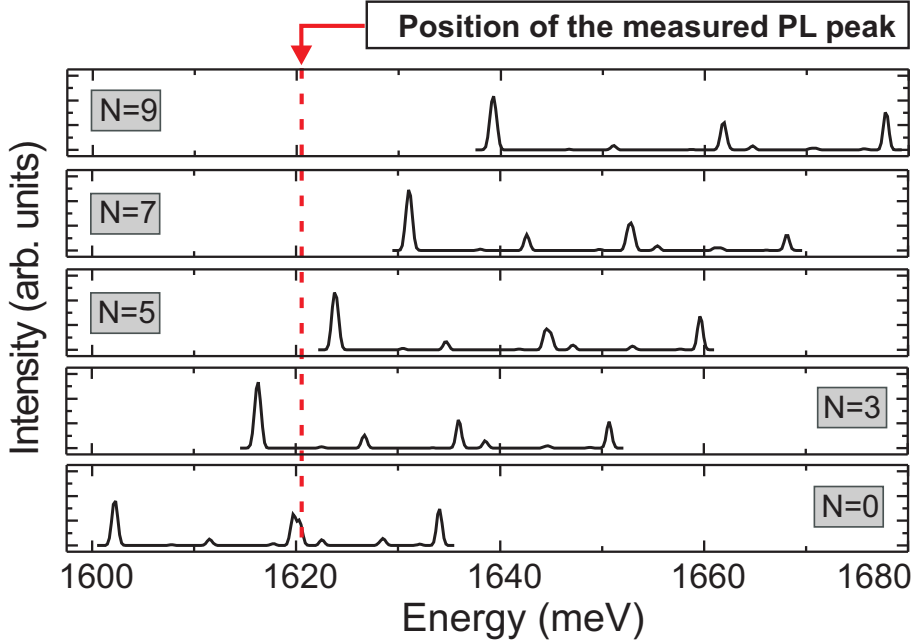


FIGURE 8.6. Exciton absorption spectra as a function of N . A blue shift in the transition energy with increasing interface intermixing is observed. The vertical red dotted line indicates the position of the measured PL peak.

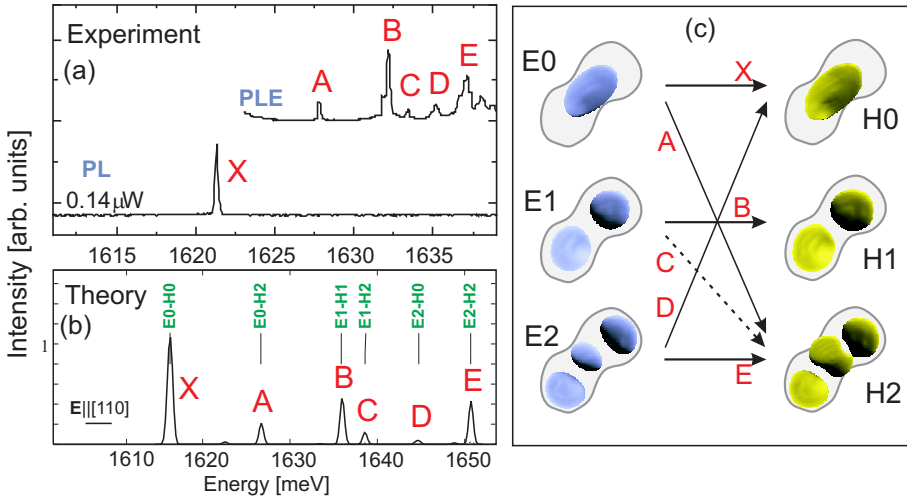


FIGURE 8.7. (a) PL ($E_{\text{exc}} = 1.96 \text{ eV}$) and PLE spectra of a single QD with $D = 7 \text{ nm}$ for different I_{exc} . The bottom graph is a calculated excitonic absorption spectrum for $N = 3$. (c) 3D representations of the first three electron and hole wavefunctions. The arrows indicate the main contributions for the red labeled transitions, shown in (a) and (b).

work [27] did not take the effect of interface roughening into account, and could not identify the peaks D and E.

This results put a clear headlight on our model - its strengths and deficiencies. The strengths are numerous, otherwise the peak identification had failed: First, when the STM raw-data were not yet available to us, we tested two interpenetrating inverted lens-shaped QDs, adjusted to the observed QD size. Although this structure turned out to be very similar to the true structure in the aftermath, the resulting spectra were very different from experiment. Earlier results, not taking into account Coulomb interaction, were completely

TABLE 2. The shift of the electron and hole energies as a function of N for two different magnetic field directions.

N	$\Delta E_e(40T)$ [meV]		$\Delta E_h(40T)$ [meV]	
	$\mathbf{B} \parallel \mathbf{e}_z$	$\mathbf{B} \parallel \mathbf{e}_x$	$\mathbf{B} \parallel \mathbf{e}_z$	$\mathbf{B} \parallel \mathbf{e}_x$
0	15.26	6.22	-1.45	-0.69
3	13.85	3.5	-0.14	-0.4
5	13.19	3.5	-0.14	-0.4
7	8.7	3.25	-0.99	-0.2
9	8.03	3.16	-0.96	-0.11

misguiding. Only the use of the full configuration scheme together with the STM measured QD-structure, finally, led to the successful agreement with experiment. A more careful inspection, however, reveals, that the energy of the calculated peaks are stronger dispersed. This is due to overestimated electron interband energies, also known as 'overconfinement'. The latter is related to insufficient non-parabolicity of the conduction band.

8.3. External magnetic fields

In this section we explore the behavior of electron, hole and exciton energies as a function of magnetic field. Both cases, a magnetic field applied parallel as well as perpendicular to the growth direction are considered. Excitonic absorption spectra are calculated for different values and orientations of \mathbf{B} and as a function of the degree of interface intermixing. Finally, we compare our theoretical findings for the exciton diamagnetic shift to experimental results from Ref. [31].

8.3.1. The role of the magnetic field direction.

Single-particle energies. An external magnetic field introduces an additional confinement in the plane perpendicular to the direction of the applied field and lifts the Kramer's degeneracy. Its impact on the electronic properties depends on the strength of the already existing QD-confinement. It is large for small confinement and small for large confinement. Since our QDs are very flat, the confinement is strong in growth direction (\mathbf{e}_z) and small in lateral direction. Therefore we expect a large effect if the B-field is applied parallel to \mathbf{e}_z and a smaller one if applied perpendicular to \mathbf{e}_z . The results of the corresponding calculations are shown in Fig. 8.8.

For the case of a lateral magnetic field, the strong QD-confinement in the growth direction limits the influence of the magnetic field. In contrast, for the case of a magnetic field applied in the growth direction, electron and hole energy levels are strongly influenced by the magnetic field and a magnetic field induced band mixing of the hole energy levels is observed. This is a direct consequence of the relatively smaller lateral confinement in the dot (e.g. magnetic length for $B = 10$ T is about 8 nm, while the base length of the dot is about 60 nm). Electron and hole wavefunctions for the two different magnetic field orientations are also shown in Fig. 8.8. One can clearly see the impact of the additional lateral confinement for $\mathbf{B} \parallel \mathbf{e}_z$ on the lateral electron and hole wavefunction extent, which does not occur for $\mathbf{B} \parallel \mathbf{e}_x$. An exchange of the character of the hole wavefunctions for magnetic field of $B=20$ T applied in the growth direction is clearly observed.

Role of the interface roughness. In Sec. 8.2 we demonstrated that the interface intermixing increases the localization of the electrons and holes. As a consequence, the impact of the magnetic field on the electron and hole states is reduced. Hence, the increase of the parameter N leads to an even smaller dependence of the electron and hole energies for a lateral magnetic field, while for a vertical magnetic field the variation of N does not lead to significant changes of the electron and hole energies. These conclusions are illustrated in table 2 for both directions of the applied magnetic field.

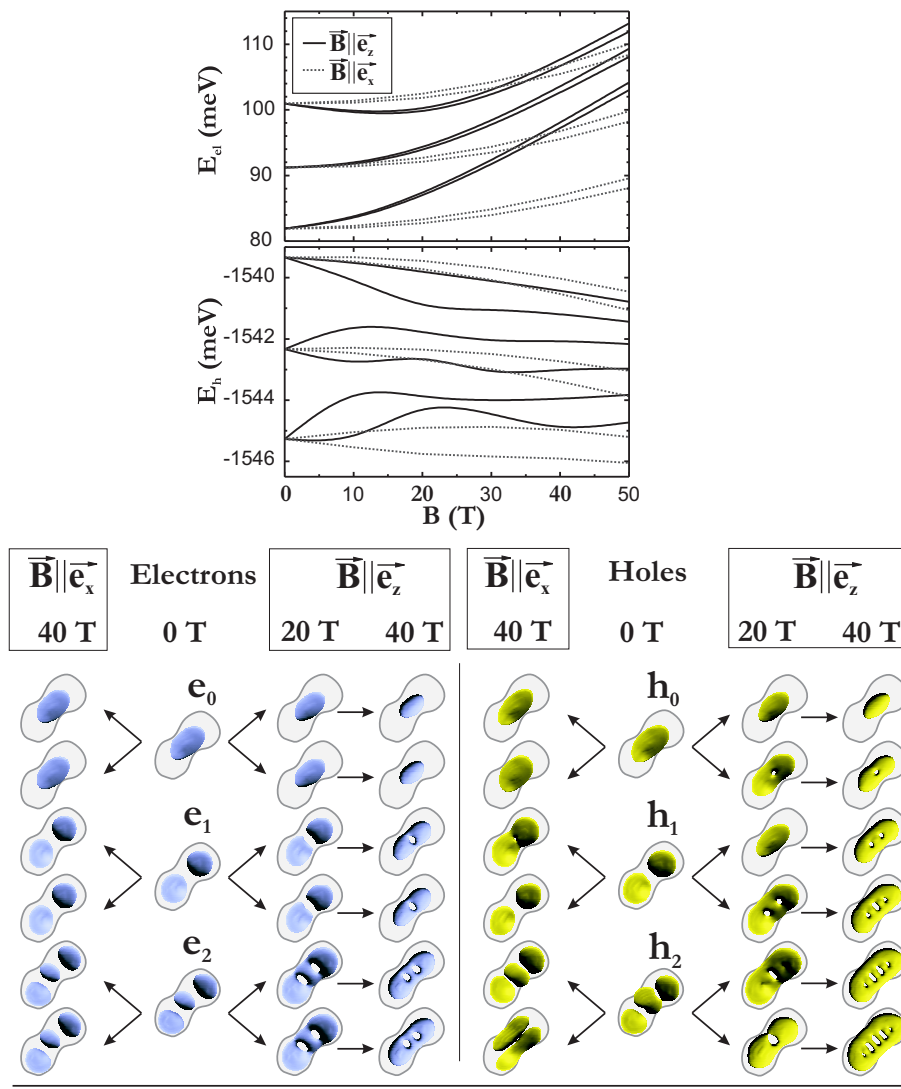


FIGURE 8.8. Electron and hole energy levels (with respect to the GaAs conduction band) as a function of the magnetic field parallel to the growth direction (black lines) and perpendicular to the growth direction (light gray lines). The case of an ideal sharp interface ($N=0$) is shown. The wavefunction isosurfaces are plotted for 65 % probability density.

The exciton-binding energy. The magnetic field dependence of the exciton-binding energy is analyzed by considering the quantity $\Delta E_{X\text{-bind}}$, defined as

$$\Delta E_{X\text{-bind}} = E_{X\text{-bind}}(B) - E_{X\text{-bind}}(B = 0) .$$

with $E_{X\text{-bind}}(B)$ being the exciton binding energy at magnetic field B . In Fig. 8.9, $\Delta E_{X\text{-bind}}$ is shown as a function of the B-field and its orientation and the degree of interface intermixing. Since the magnetic field further enhances the wavefunction localization it is of no surprise that the exciton binding energies $E_{X\text{-bind}}$ increase upon an increase of the magnetic field [see Fig. 8.9(a)]. This effect is much larger for $\mathbf{B} \parallel \mathbf{e}_x$ than for $\mathbf{B} \parallel \mathbf{e}_z$ since in the former case the increase of the wavefunction localization is much stronger than in the latter. As the interface smoothing leads to an additional carrier localization in our case, $\Delta E_{X\text{-bind}}$ becomes smaller as a function of N [see Fig. 8.9 (b)].

The effect of smoothing of the interface on the excitonic absorption spectra for $B = 10$ T for magnetic field applied in the growth direction and in plane are shown in Figs. 8.10 (a) and 8.10 (b) respectively.

The exciton absorption spectra are richer for the case of magnetic field applied in the growth direction. The reason for this can be found in the larger spin splitting and the arising additional transitions in a magnetic

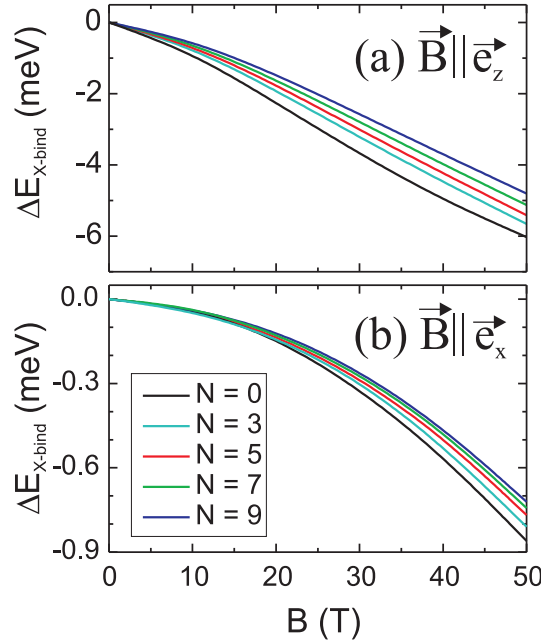


FIGURE 8.9. Exciton-binding energies as a function of magnetic field applied in the growth direction (a) and in the direction perpendicular to the growth direction (b) for different interface intermixing. ΔE_{Xbind} defined as $\Delta E_{Xbind} = E_{Xbind}(B) - E_{Xbind}(B = 0)$, where $E_{Xbind}(B)$ is exciton-binding energy for value of magnetic field B , and $E_{Xbind}(B = 0)$ is exciton binding energy in the absence of a magnetic field.

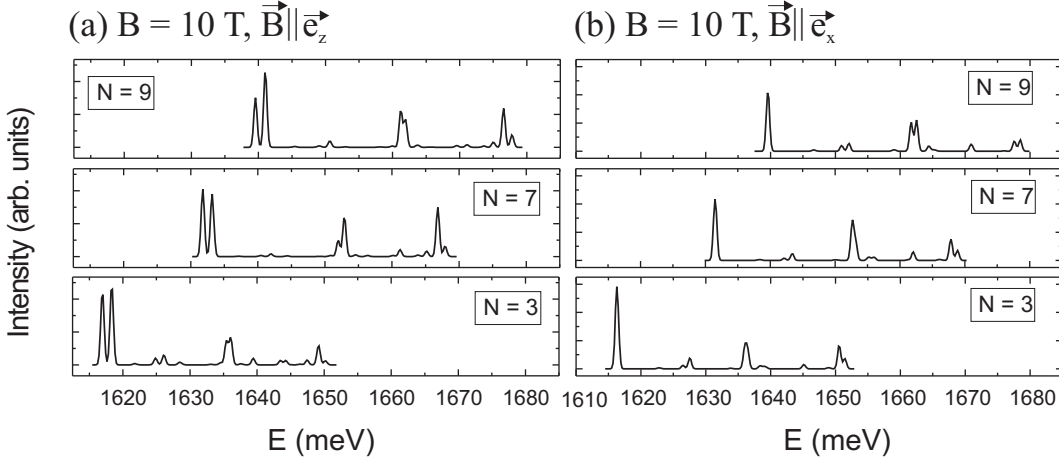


FIGURE 8.10. Exciton absorption spectra for $B = 10$ T applied in the growth direction for three values of $N = 3, 7, 9$.

field whose effect on the electronic structure is much larger than in the case of magnetic field applied in plane.

8.3.2. Comparison with experiment. The exciton absorption spectrum of our model QD for $N = 3$ has already shown an excellent agreement with the measured single QD PL and PLE spectra [27] in the absence of an external magnetic field. In Ref. [31] the same samples have been used to perform low and high excitation PL-measurements using high magnetic fields parallel and perpendicular to the growth direction. In Figs. 8.11 and 8.12 we compare the excitonic absorption spectra to the high exciton PL-results for both field directions. Although the latter case corresponds to a multiexcitonic decay rather than excitonic absorption, we can link the p -channel absorption to the decay of 3- and 4-fold excitons and the d -channel absorption to

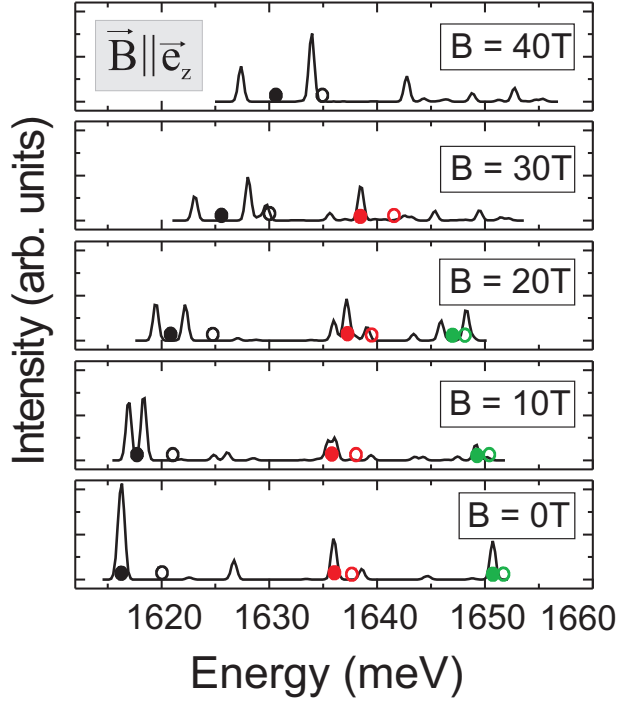


FIGURE 8.11. Comparison between calculated excitonic absorption spectra ($N=3$) and the measured peak positions in the high excitation PL-spectra (open symbols). The bold symbols are guide to the eye. The experimental values are taken from a QD-sample with a slightly thicker AlGaAs barrier leading to a shallower QD compared to our model QD.

that of the 5- to 6-fold exciton, provided the renormalization effects, being linked to the presence of more than one exciton, are small. The agreement however is quite remarkable: Our calculations reproduce the experimental results qualitatively and to a large degree also quantitatively.

The splitting of the s -channel peaks, caused by the Zeeman splitting of the single-particle orbitals is smaller than the experimental PL-broadening and therefore hidden in the experimental data. The smaller splitting of these peaks for lateral magnetic field is related to the smaller Zeeman splitting of electron and hole orbitals, which in turn is related to the large z-confinement. An explanation for such a behavior of the exciton absorption spectra as a function of the orientation of a magnetic field was given in Sec. 8.3.1.

The exciton diamagnetic shift. More information about the interplay between the Coulomb interaction and the QD-confinement in the direction perpendicular to the direction of the applied magnetic field can be obtained by considering the exciton diamagnetic shift defined as

$$\Delta E_{exc} = E_{exc}(B) - E_{exc}(B = 0T) .$$

The transition energy of two lowest optically active excitons are averaged since their Zeeman-splitting is smaller than the PL-broadening. The obtained data for the exciton diamagnetic shift are compared to the position of the PL peak taken from Ref. [31] for both orientations of the magnetic field and for different values N of the interface intermixing. The best agreement for the diamagnetic shift for both magnetic field directions is achieved for a value of N in between $N=0$ and $N=3$, whereas for the absolute values of E_X (see inset of Figs. 8.13 and 8.14) the agreement is best for N -values in between $N=3$ and $N=5$.

Furthermore, as can be seen from Fig. 8.9, a smoother interface does not significantly affect the change of the X-binding energy with magnetic field. The changes in the curvature of the exciton diamagnetic shift with the variation of N from $N=0$ to $N=3$ or from $N=3$ to $N=5$ are not significant when the magnetic field is applied in the growth direction (Fig. 8.13) and a good agreement with the experimental data is achieved for all these values of N ($N=0, 3, 5$). A significant discrepancy to the experimental data is only observed if N is larger than 5. For the lateral magnetic field case, one can see from Fig. 8.14 that the relative exciton

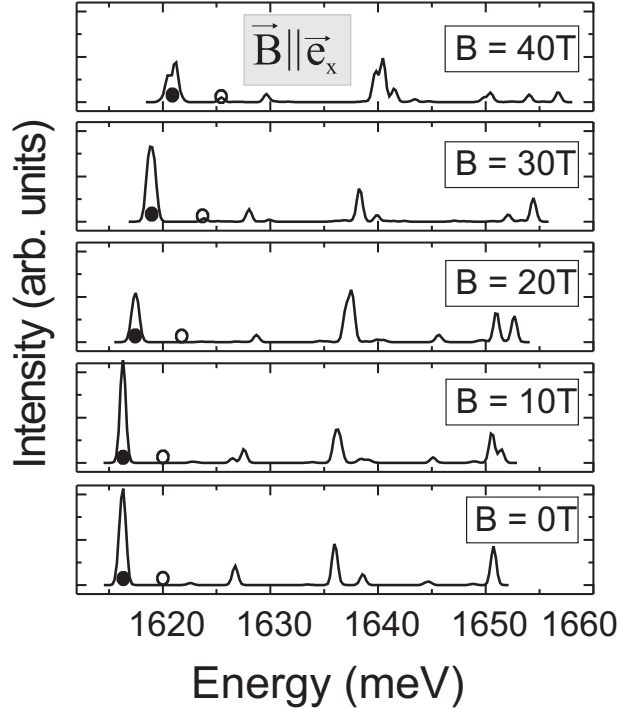


FIGURE 8.12. The same as Fig. 8.11 but now for magnetic field applied in the lateral direction. The available experimental data are shown by open symbols.

diamagnetic shift for $N=5$ is quite close to the one for $N=9$. This is related to the increased vertical QD-confinement for $N \geq 5$ which leads to a suppression of the magnetic field influence (magnetic length is larger than the height of the dot). The best overall agreement between our findings on the exciton energy and the exciton diamagnetic shift with the experimental data is obtained for our model QD with $N=3$. This result is in perfect agreement to the reported experimental results of Ref. [29] obtained from X-STM measurements on samples fabricated by using the same growth mode.

A similar comparison has been performed recently [32] using a single-band model with additional terms for the conduction band non-parabolicity. A good agreement for the relative exciton shift was obtained, whereas the absolute PL energies were not reproduced accurately. Note, that the electron effective mass dominates in the exciton effective mass, and therefore any changes in the electron effective mass would be directly reflected through the changes in the relative exciton shift. In Ref. [32] it was a priori assumed that the CB-non-parabolicity originates *only* from coupling to higher conduction bands. Here, it was shown, that the inherent coupling of valence- and conduction band in the eight-band $\mathbf{k}\cdot\mathbf{p}$ model is already sufficient to explain the effects observed in Ref. [31] without an additional non-parabolicity induced by coupling to higher lying conduction bands.

8.4. Discussion

First, the interdiffusion of aluminium at the heterojunction during the growth significantly influences the transition energies (see Sec. 8.2). The ground state transition energies for the ideal case of no intermixing ($N=0$ in Fig. 8.6) and the case of strong intermixing ($N=9$ in Fig. 8.6) differ by about 37 meV while intra subband transitions are not affected significantly. For example, for $N=0$ the distance between the transition 1 and transition 2 is 9.2 meV, while in the case of $N=9$ this distance is 11.8 meV. The observed blue shift between PLE data and calculated absorption spectrum extracted from eight-band $\mathbf{k}\cdot\mathbf{p}$ theory [27] can be explained by this intermixing. The effect of interface intermixing is far from being negligible and should be properly taken into account.

Second, the influence of an applied external magnetic field in the growth direction as well as in-plane on the electronic and optical properties was studied in Sec. 8.3. In general, since the dots are quite large in

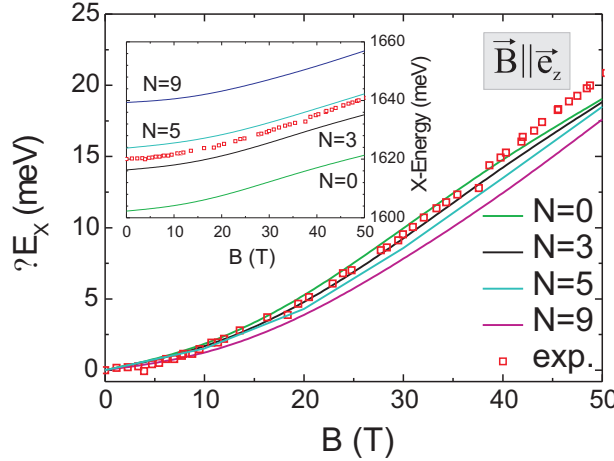


FIGURE 8.13. The exciton diamagnetic shift as the function of a magnetic field for the optical active exciton states compared to the experimental results (symbols). An external magnetic field is applied in the growth direction. The inset depicts the absolute values for the calculated exciton energy vs. magnetic field together with the experimental data.

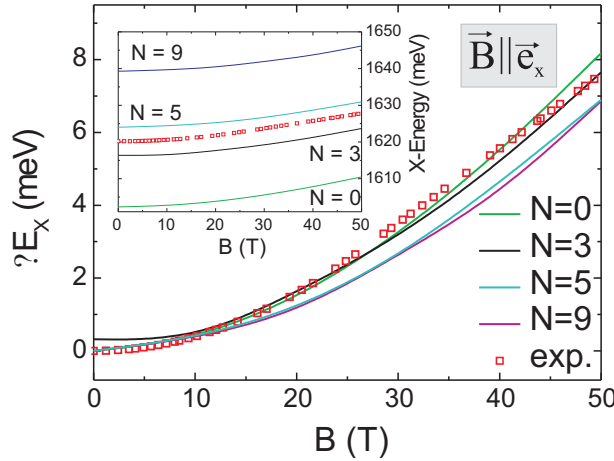


FIGURE 8.14. The same as Fig. 8.13 but now for magnetic field applied in the lateral direction.

the lateral direction the effect of a magnetic field applied in the growth direction are more pronounced than if the magnetic field is applied perpendicular to the growth direction. For example, complicated behavior of hole energy levels as a function of magnetic field applied in the growth direction with strong anti-crossing does not exist in the case of magnetic field applied perpendicular to the growth direction which is a direct consequence of the competition between the confinement and magnetic field.

Two questions were raised in Ref. [31] related to tunnelling and the degree of non-parabolicity of the conduction band and its influence on the excitonic properties. In our model we explicitly include the mixing of the lowest lying conduction band and the three top most valence bands. Next, in the modeling of the excitonic properties the direct Coulomb interaction, exchange and correlation were included. From Figs. 8.3 (b) and (d) it is clear that the penetration of the electron and hole wavefunctions into the barrier is small and that interface intermixing even increases the localization of the electrons and holes. Therefore, we conclude that the effect of tunnelling in these structures is negligible.

The non-parabolicity of the conduction band originates from the coupling to the valence band and to higher conduction bands. In our eight-band $k \cdot p$ model only the former is accounted for. The confinement and, hence, the localization of electron and hole states comes into play due to their resulting spread in k -space, and the accompanying contributions far from the Γ point. This confinement in our case comes

predominantly from the dot itself and is enhanced by the applied magnetic field. From Figs. 8.11, 8.12, 8.13 and 8.14, it becomes clear that our fit-parameter free results agree very well with the experimental data. We conclude that the inherent coupling of valence- and conduction band present in the eight-band $\mathbf{k} \cdot \mathbf{p}$ model is sufficient to explain the effects observed in Ref. [31] without additional non-parabolicity originating from coupling to higher conduction bands.

8.5. Summary and Conclusions

The electronic structure of unstrained GaAs/Al_xGa_{1-x}As QDs in the presence of an external magnetic field was studied. Interface roughness was observed to sensitively affect the transition energies, but hardly the intraband energies. For a magnetic field applied in the growth direction and in the direction perpendicular to the growth direction (with $B \leq 50$ T), we find good agreement between the exciton diamagnetic shift obtained from our calculations and the experimental data from Ref. [31]. We discussed the effect of tunneling and the degree of non-parabolicity and found that tunnelling was negligible in our model and that the inherent coupling of valence- and conduction band present in the eight-band $\mathbf{k} \cdot \mathbf{p}$ model is sufficient to explain the "non-parabolicity" effects reported in Ref. [31].

Further on, the results for $N = 3$ are compared to single-QD PL and PLE spectra, which marks a new level in the relation of QD-spectroscopy and theory and constitutes a true challenge to the employed model. Since the QD-structure was almost unambiguously known from STM and X-STM data, the only employed 'fitting' parameter was N , the degree of interface roughening. The measured ground- *and* excited state absorption peaks were successfully identified for the first time. The comparison further revealed marginal 'overconfinement' effects of the excited state electrons. In this case, the lack of coupling to higher conduction bands in the eight-band $\mathbf{k} \cdot \mathbf{p}$ model becomes apparent.

Summary and Outlook

In this work the correlation between structural QD properties like size, shape and composition and their electronic and optical properties has been investigated systematically. We compared the electronic properties of round and square based InAs/GaAs QDs with constant volume but varying aspect ratios. A large redistribution of strain from dominant hydrostatic for tall dots to pronounced biaxial for flat dots is observed, thus changing the single-particle hole energies and their HH-LH ratio.

The effect of annealing on a pyramidal QD has been simulated. The electron and hole groundstate energies are shifted by 50 and 70 meV to higher energies resulting in a blue-shift of the exciton groundstate absorption energy. The corresponding electron and hole wavefunctions are stronger localized.

The classical approach of calculating the piezoelectric field in QDs [2] has been extended to the one recently developed by Bester *et al.*[11, 42], which takes into account the second order piezoelectric field. We found the piezoelectric potential arising from the quadratic terms to be very sensitive to the base shape, the vertical aspect ratio, and the composition. Its orientation inside the QD is reverse compared to the first order potential and can surpass it resulting into a reversal of the electron *p*- and *d*-state ordering and a reorientation of the hole wavefunctions, as observed for InAs pyramidal QDs. In this case the quadratic terms exceeds the linear contributions inside the QD. Upon gradual annealing of this QD, thus introducing an isotropic composition gradient, the second order field decreases dramatically, leaving the first order contribution as the dominant part. As a result, the electron *p*- and *d*-state order and the hole wavefunction orientations change.

We calculated the excitonic absorption spectra and the CB-intraband transitions. The former are very sensitive to almost all applied structural changes and to the piezoelectric field, leading to strong modification of the *p*- and *d*-channel transitions. Upon changing the model for the piezoelectric field calculations, a peak reordering within these absorption channels can occur and the polarization anisotropy between $e \parallel [110]$ and $e \parallel [1\bar{1}0]$ can change. CB-intraband-transition spectra are strongly polarized either along [110] or [1 $\bar{1}$ 0] and very sensitive to changes of the piezoelectric field or any other anisotropy.

The relationship between the structural properties and the energies of a selected set of few-particle states (X, XX, X^\pm), which can be easily traced in experiment, has been investigated in detail. The resulting binding energies turn out to be very sensitive to the various morphological peculiarities. We analyzed in detail the relationship between the QD geometry, the resulting shape and position of electron and hole wavefunctions, the direct Coulomb energies and changes introduced by correlation effects. The correlation effects are larger for biexciton and positive trion, which is attributed to the larger spectral density of the hole subsystem. This in turn is a result of the larger hole effective mass. In addition, we found the correlation to be very sensitive to the relative size and position of the electron and hole ground state orbitals, which influences equally the direct Coulomb energies $J_{00}^{(e\bar{h})}, J_{00}^{(ee)} \text{ and } J_{00}^{(hh)}$. Large correlation energies $\delta_{\text{Corr}}(XX)$ and $\delta_{\text{Corr}}(X^+)$ are observed in those cases, where the absolute value of the attractive Coulomb term $J_{00}^{(e\bar{h})}$ falls below the values of the repulsive terms $J_{00}^{(ee)}$ and $J_{00}^{(hh)}$.

The electronic properties in stacks of identical and nonidentical InGaAs/GaAs QDs were investigated. We studied the decisive parameters, that determine the onset of electronic coupling: The relative QD size, the inter-QD distance, the symmetry of the overlapping single QD wavefunctions, strain and piezoelectricity.

For pairs of identical QDs, strain has an asymmetric impact on the individual QDs and renders their confinement inequivalent. Electrons form binding and anti-binding orbitals. Despite the arising splitting, the ground state energy is shifted to higher energies for intermediate dot-dot separation (>20 ML), compared

to the respective single dot reference. The hole ground states do not form hybrid orbitals and are located at the lowest QD. Upon smaller inter-dot distance their energy decreases up to 35 meV, with respect to the single QD reference. The resulting larger band gap is in accordance with experimental results.[117]

Further on, we investigated the role of symmetry for the interacting states by means of group character theory. If the resonant states belong to the same irreducible representation they exhibit anti-crossing behavior and form hybrid orbitals, otherwise we observe level crossing.

The interrelation of QD-shape, strain, HH/LH ratio of hole states and the optical properties with respect to the TE/TM-mode has been studied. The balanced ratio of the latter is decisive for semiconductor optical amplifier. We found, that the biaxial strain changes its sign if the QDs aspect ratio becomes larger than one. As a result, the TM-mode absorption exceeds that of the TE-mode. The same holds for large stacks of closely spaced QDs. The results are in agreement with measurements of Kita *et al.*[15] for such systems.

The role of substrate orientation on the electronic and optical properties of QDs has been studied theoretically in this work. Based on AFM and X-STM measurements, it has been demonstrated that eight-band $\mathbf{k} \cdot \mathbf{p}$ calculations, performed on truncated conical shape QDs, show a good agreement with photoluminescence measurements performed on (311)B substrate, for various QDs heights. Next, we found that QDs grown on (311)B and (100) substrate exhibit different excitonic optical signatures mainly for two reasons: First, the larger hydrostatic strain observed for the (311)B-QDs elevates the electron energies thus causing an overall increase of the excitonic transition energy. Second, the way the piezoelectric field acts on both substrates is fundamentally different in view of its strength and its orientation. This alters the symmetry properties of the confinement potential and induces the optical activation of second order transitions on the (311)B substrate.

The electronic structure of unstrained GaAs/Al_xGa_{1-x}As QDs in the presence of an external magnetic field was studied. Interface roughness was observed to sensitively affect the transition energies. For a magnetic field applied in the growth direction and in the direction perpendicular to the growth direction (where $B \leq 50\text{T}$), good agreement between the exciton diamagnetic shift, obtained from our calculations, and the experimental data from Ref. [31] is achieved. The inherent coupling of valence- and conduction band present in the eight-band $\mathbf{k} \cdot \mathbf{p}$ model is sufficient to explain the "nonparabolicity" effects reported in Ref. [31].

Further on, the results are compared to single-QD PL and PLE spectra, which marks a new level in the relation of QD-spectroscopy and theory and constitutes a true challenge to the employed model. Since the QD-structure was almost unambiguously known from STM and X-STM data, the only employed 'fitting' parameter was N, the degree of interface roughening. The measured ground- *and* excited state absorption peaks were successfully identified for the first time.

Outlook

In our recent work,[4] we investigated the fine-structure splitting in InAs/GaAs QDs. Although, we were able to reproduce the observed trends qualitatively, no quantitative agreement was achieved. In collaboration with R. Zimmermann, the dipol-dipol interaction terms of the exchange interaction have been implemented, but not sufficiently tested so far. Preliminary results indicate vast improvements over the present results.

The validity of the eight-band $\mathbf{k} \cdot \mathbf{p}$ model is restricted to direct band gap semiconductors. The implementation of our model, however, is not restricted to account for eight bands only. Fourteen- and thirty-band models have been used for bulk and quantum wells and we do not see principal handicaps that would hamper a similar implementation for QDs. The major challenge would be to obtain the necessary additional deformation potential parameter.

So far, piezoelectricity is the only implemented source, that introduces C_{2v} -confinement for otherwise fourfold symmetric QDs. However, it should be investigated, whether additional effects related to the lack of inversion symmetry of the underlying zinc-blende lattice, can be implemented.

Coulomb interaction effects are expected to play a major role in stacked QDs as well. In the case of weakly coupled dots, the Coulomb coupling could lead to a renormalization effects and possibly prevent

the formation of binding and anti-binding states. This effect can not be captured by using the hybrid single particle states to built up the CI -basis. Rather, it is recommendable to use the single dot states as basis. Since the latter are non-orthogonal in adjacent QDs, major software enhancements are necessary. These modifications, however, can also be beneficial for other systems, like nitride-based QDs, by using those orbitals as basis functions, that result from the Hartree method. In doing so, the limitations by the small basis of bound orbitals might be overcome, and exchange and correlation effects better accounted for.

Acknowledgements

I am grateful to Prof. Dr. Dieter Bimberg who gave me the opportunity to learn and work in his group during the last years, and who persistently stimulated and supported the progress of my work, and who refereed this thesis.

Prof. Dr. Marius Grundmann and Prof. Dr. Eckehard Schöll are cordially acknowledged for refereeing this thesis.

My sincere gratitude is due to my colleague Momme Winkelkemper, who shared my office, wrote a lot of important software, took care of my computer system, and who followed my scientific efforts with sympathy.

During the largest part of my way leading to this thesis I was accompanied by Dr. Sven Rodt who provided any, whatsoever support, for instance, assistance in all computer concerns.

Robert Seguin together with Sven Rodt, produced unmanageable heaps of exciting data on single QDs. He is my everlasting ideal when it comes to quick and sound paper-writing.

Oliver Stier and Volker Türck laid the basis of this work. The former by writing exceptionally good software for finding interior Eigenvalues of very large matrices. The other, for attracting me to this group and guiding me the first steps into the world of nanostructures.

The unforgettable Robert Heitz, who is not among us anymore, laid the seed for so many of the projects in our group. Unfortunately he cannot see them flourish.

Doreen Nitzsche and Ines Rudolph, as present and former SFB 296 secretary, made it possible for me to focus on this work, rather than on organizational issues.

All the other former and present members of our group are cordially acknowledged for cake and candy, many hours in front of the silver screen etc. Special thanks go to our secretary, Ulrike Grupe.

Armando Rastelli, Charles Cornet, and Vladan Mlinar are acknowledged for the collaboration and many insightful discussions.

I thank my mother, Margarete Schliwa-Deneke, who encouraged me all the time. She always wanted me to study some natural science and succeeded finally. My father, Harald Schliwa, taught me to follow my own way. Unfortunately, he cannot witness the completion of this thesis anymore. Jürgen Deneke, for all the support and gifts.

I am grateful to Anja Natalie Brostowski, who gave birth to our daughter Maja Enola, for so many things and to her family, Sandra, Petra, and Michael, who give us invaluable support in all matters.

Bibliography

- [1] D. Bimberg, M. Grundmann, and N. N. Ledentsov, *Quantum Dot Heterostructures* (John Wiley & Sons, 1999).
- [2] M. Grundmann, O. Stier, and D. Bimberg, Phys. Rev. B **52**, 11969 (1995).
- [3] O. Stier, M. Grundmann, and D. Bimberg, Phys. Rev. B **59**, 5688 (1999).
- [4] R. Seguin, A. Schliwa, S. Rodt, K. Pötschke, U. W. Pohl, and D. Bimberg, Phys. Rev. Lett. **95**, 257402 (2005).
- [5] N. Kirstaedter, N. Ledentsov, M. Grundmann, D. Bimberg, V. Ustinov, S. Ruvimov, M. Maximov, P. Kop'ev, Z. Alferov, U. Richter, et al., Electron. Lett. **30**, 1416 (1994).
- [6] N. Ledentsov, M. Grundmann, F. Heinrichsdorff, D. Bimberg, V. Ustinov, A. Zhukov, M. Maximov, Z. Alferov, and J. Lott, Selected Topics in Quantum Electronics, IEEE Journal of **6**, 439 (2000).
- [7] D. Bimberg, G. Fiol, M. Kuntz, C. Meuer, M. Lämmelin, N. N. Ledentsov, and A. R. Kovsh, phys. stat. sol. (a) **14**, 3523 (2006).
- [8] O. Stier and D. Bimberg, Phys. Rev. B **55**, 7726 (1997).
- [9] H. Eisele, O. Flebbe, T. Kalka, C. Preinesberger, F. Heinrichsdorff, A. Krost, D. Bimberg, and M. Dähne Prietsch, Appl. Phys. Lett. **75**, 106 (1999).
- [10] J. Marquez, L. Geelhaar, and K. Jacobi, Appl. Phys. Lett. **78**, 2309 (2001).
- [11] G. Bester, X. Wu, D. Vanderbilt, and A. Zunger, Phys. Rev. Lett. **96**, 187602 (2006).
- [12] N. N. Ledentsov, V. A. Shchukin, M. Grundmann, N. Kirstaedter, J. Böhrer, O. Schmidt, D. Bimberg, V. M. Ustinov, A. Y. Egorov, A. E. Zhukov, et al., Phys. Rev. B **54**, 8743 (1996).
- [13] G. Bester, J. Shumway, and A. Zunger, Phys. Rev. Lett. **93**, 047401 (pages 4) (2004).
- [14] E. Biolatti, R. C. Iotti, P. Zanardi, and F. Rossi, Phys. Rev. Lett. **85**, 5647 (2000).
- [15] T. Kita, O. Wada, H. Ebe, Y. Nakata, and M. Sugawara, Jpn. J. Appl. Phys. **41**, 1143 (2002).
- [16] D. Bimberg, M. Kuntz, and M. Lämmelin, Microelectronics Journal **36**, 175 (2005).
- [17] M. Lämmelin, G. Fiol, C. Meuer, M. Kuntz, F. Hopfer, A. R. Kovsh, N. N. Ledentsov, and D. Bimberg, Electronics Letters **42**, 697 (2006).
- [18] A. V. Uskov, E. P. O'Reilly, M. Lämmelin, N. N. Ledentsov, and D. Bimberg, Optics Communications **248**, 211 (2005).
- [19] N. S. Wingreen and C. A. Stafford, IEEE J. of Quant. Elec. **33**, 1170 (1997).
- [20] N. Vukmirovic, Z. Ikonic, V. D. Jovanovic, D. Indjin, and P. Harrison, IEEE J. of Quant. Elec. **41**, 1361 (2005).
- [21] L. Y. Karachinsky, T. Kettler, N. Y. Gordeev, I. I. Novikov, M. V. Maximov, Y. M. Shernyakov, N. V. Kryzhanoskaya, A. E. Zhukov, E. S. Semenova, A. P. Vasilev, et al., Electron. Lett. **41**, 1209 (2005).
- [22] C. Paranthoen, N. Bertru, O. Dehaese, A. L. Corre, S. Loualiche, B. Lambert, and G. Patriarche, Appl. Phys. Lett. **78**, 1751 (2001).
- [23] P. Caroff, N. Bertru, A. L. Corre, T. Rohel, I. Alghoraibi, H. Folliot, and S. Loualiche, Jpn. J. Appl. Phys. **44**, L1069 (2005).
- [24] C. Cornet, C. Platz, P. Caroff, J. Even, C. Labb  , H. Folliot, A. L. Corre, and S. Loualiche, Phys. Rev. B **72**, 035342 (2005).
- [25] H. Saito, K. Nishi, and S. Sugou, Appl. Phys. Lett. **78**, 267 (2001).
- [26] P. Caroff, C. Paranthoen, C. Platz, O. Dehaese, H. Folliot, N. Bertru, C. Labb  , R. Piron, E. Homeyer, A. L. Corre, et al., Appl. Phys. Lett. **87**, 243107 (2005).

- [27] A. Rastelli, S. Stufler, A. Schliwa, R. Songmuang, C. Manzano, G. Costantini, K. Kern, A. Zrenner, D. Bimberg, and O. G. Schmidt, *Appl. Phys. Lett.* **92**, 166104 (2004).
- [28] V. Mlinar, M. Tadić, B. Partoens, and F. M. Peeters, *Phys. Rev. B* **71**, 205305 (2005).
- [29] A. Lenz, R. Timm, H. Eisele, L. Ivanova, D. Martin, V. Vosseburger, A. Rastelli, O. G. Schmidt, and Dähne, *phys. stat. sol. (b)* **243**, 3976 (2006).
- [30] M. Hermann, D. Bimberg, and J. Christen, *J. Appl. Phys.* **70**, R1 (1991).
- [31] N. Schildermans, M. Hayne, V. V. Moshchalkov, A. Rastelli, and O. G. Schmidt, *Phys. Rev. B* **72**, 115312 (2005).
- [32] Y. Sidor, B. Partoens, F. M. Peeters, N. Schildermans, M. Hayne, V. V. Moshchalkov, A. Rastelli, and O. G. Schmidt, *Phys. Rev. B* **73**, 155334 (2006).
- [33] O. Stier, *Electronic and Optical Properties of Quantum Dots and Wires*, Berlin Studies in Solid State Physics 7 (Wissenschaft und Technik Verlag, 2001).
- [34] C. Pryor, J. Kim, L. W. Wang, A. J. Williamson, and A. Zunger, *J. Appl. Phys.* **83**, 2548 (1998).
- [35] A. J. Williamson, L. W. Wang, and A. Zunger, *Phys. Rev. B* **62**, 12 963 (2000).
- [36] E. O. Kane, *Phys. Rev. B* **31**, 7865 (1985).
- [37] O. L. Lazarenkova, P. von Allmen, F. Oyafuso, S. Lee, and G. Klimeck, *Appl. Phys. Lett.* **85**, 4193 (2004).
- [38] T. Hammerschmidt and P. Kratzer, in *AIP Conf. Proc. 772: Physics of Semiconductors*, edited by J. Menéndez and C. G. van de Walle (2005), pp. 601–602.
- [39] M. A. Migliorato, A. G. Cullis, M. Fearn, and J. H. Jefferson, *Phys. Rev. B* **65**, 115316 (2002).
- [40] J. Tersoff, *Phys. Rev. B* **39**, 5566 (1989).
- [41] W. F. Cady, *Piezoelectricity* (McGraw-Hill, 1946).
- [42] G. Bester, A. Zunger, X. Wu, and D. Vanderbilt, *Phys. Rev. B* **74**, 081305 (2006).
- [43] G. Bester and A. Zunger, *Phys. Rev. B* **71**, 045318 (2005).
- [44] P. Enders, A. Bärwolf, and M. W. D. Suisky, *Phys. Rev. B* **51**, 16695 (1995).
- [45] E. O. Kane, in *Band Theory and Transport Properties*, edited by W. Paul (North-Holland, 1982), vol. 1 of *Handbook on Semiconductors*, p. 194.
- [46] F. H. Pollak, *Semicond. Semimet.* **32**, 17 (1990).
- [47] P. Enders, *phys. stat. sol. (b)* **187**, 541 (1995).
- [48] D. Gershoni, C. H. Henry, and G. A. Baraff, *IEEE J. of Quant. Elec.* **29**, 2433 (1993).
- [49] H. Jiang and J. Singh, *Phys. Rev. B* **56**, 4696 (1997).
- [50] C. Pryor, *Phys. Rev. B* **57**, 7190 (1998).
- [51] J. A. Majewski, S. Birner, A. Trellakis, M. Sabathil, and P. Vogl, *phys. stat. sol. (c)* **8**, 2003 (2004).
- [52] T. B. Bahder, *Phys. Rev. B* **41**, 11992 (1990).
- [53] A. S. Saada, *Elasticity: Theorie and applications* (Robert E. Krieger Publishing Co., 1989).
- [54] C. G. Van de Walle, *Phys. Rev. B* **39**, 1871 (1989).
- [55] J. Kim, L. W. Wang, and A. Zunger, *Phys. Rev. B* **57**, R9408 (1998).
- [56] H. Fu, L.-W. Wang, and A. Zunger, *Phys. Rev. B* **57**, 9971 (1998).
- [57] R. Santoprete, B. Koiller, B. Capaz, P. Kratzer, Q. K. K. Liu, and M. Scheffler, *Phys. Rev. B* **68**, 235311 (2003).
- [58] S. Lee, F. Oyafuso, P. von Allmen, and G. Klimeck, *Phys. Rev. B* **69**, 045316 (2004).
- [59] S. L. Chuang, *Physics of Optoelectronic Devices* (Wiley, New York, 1995).
- [60] J. Shumway, A. Franceschetti, and A. Zunger, *Phys. Rev. B* **63**, 155316 (2001).
- [61] F. Bras, P. Boucaud, S. Sauvage, G. Fishman, and J.-M. Gerard, *Applied Physics Letters* **80**, 4620 (2002).
- [62] P. Boucaud and S. Sauvage, *C. R. Physique* **4**, 1133 (2003).
- [63] T. Maltezopoulos, A. Bolz, C. Meyer, C. Heyn, W. Hansen, M. Morgenstern, and R. Wiesendanger, *Phys. Rev. Lett.* **91**, 196804 (2003).

- [64] A. Lenz, R. Timm, H. Eisele, Ch. Hennig, S. K. Becker, R. L. Sellin, U. W. Pohl, D. Bimberg, and M. Dähne, *Appl. Phys. Lett.* **81**, 5150 (2002).
- [65] S. Ruvimov, P. Werner, K. Scheerschmidt, U. Gösele, J. Heydenreich, U. R. N. N. Ledentsov, M. Grundmann, D. Bimberg, V. M. Ustinov, A. Y. Egorov, et al., *Phys. Rev. B* **51**, 14766 (1995).
- [66] S. Rodt, A. Schliwa, K. Pötschke, F. Guffarth, and D. Bimberg, *Phys. Rev. B* **71**, 155325 (2005).
- [67] R. Seguin, A. Schliwa, T. Germann, T. Hammerschmidt, S. Rodt, K. Pötschke, A. Strittmatter, M. Winkelkemper, U. Pohl, P. Kratzer, et al., *Appl. Phys. Lett.* **89**, 263109 (2006).
- [68] P. W. Fry, I. E. Itskevich, D. J. Mowbray, M. S. Skolnick, J. J. Finley, J. A. Barker, E. P. O'Reilly, L. R. Wilson, I. A. Larkin, P. A. Maksym, et al., *Phys. Rev. Lett.* **84**, 733 (2000).
- [69] J. A. Barker and E. P. O'Reilly, *Phys. Rev. B* **61**, 13840 (2000).
- [70] M. Sabathil, S. Hackenbuchner, S. Birner, J. A. Majewski, P. Vogl, and J. J. Finley, *phys. stat. sol. (c)* **0**, 1181 (2003).
- [71] T. Walther, A. G. Cullis, D. J. Norris, and M. Hopkinson, *Phys. Rev. Lett.* **86**, 2381 (2001).
- [72] D. M. Bruls, J. W. A. M. Vugs, P. M. Koenraad, H. W. M. Salemink, J. H. Wolter, M. Hopkinson, M. S. Skolnick, F. Long, and S. P. A. Gill, *Applied Physics Letters* **81**, 1708 (2002).
- [73] I. Vurgaftman, J. R. Meyer, and L. R. Ram Mohan, *J. Appl. Phys.* **89**, 5815 (2001).
- [74] F. Heinrichsdorff, M. Grundmann, O. Stier, A. Krost, and D. Bimberg, *J. Cryst. Growth* **195**, 540 (1998).
- [75] M. Bayer, T. Gutbrod, A. Forchel, V. D. Kulakovskii, A. Gorbunov, M. Michel, R. Steffen, and K. H. Wang, *Phys. Rev. B* **58**, 4740 (1998).
- [76] S. Rodt, R. Heitz, A. Schliwa, R. L. Sellin, F. Guffarth, and D. Bimberg, *Phys. Rev. B* **68**, 035331 (2003).
- [77] L. Landin, M. S. Miller, M. Pistol, C. E. Pryor, and L. Samuelson, *Science* **280**, 282 (1998).
- [78] M. E. Ware, A. S. Bracker, E. Stinaff, D. Gammon, D. Gershoni, and V. L. Korenev, *Physica E* **13**, 55 (2005).
- [79] B. Urbaszek, R. J. Warburton, K. Karrai, B. D. Gerardot, P. Petroff, and J. Garcia, *Phys. Rev. Lett.* **90**, 247403 (2003).
- [80] G. A. Narvaez, G. Bester, and A. Zunger, *Phys. Rev. B* **72**, 245318 (2005).
- [81] I. A. Akimov, A. Hundt, T. Flissikowski, and F. Henneberger, *Appl. Phys. Lett.* **81**, 4730 (2002).
- [82] R. Seguin, S. Rodt, A. Schliwa, K. Pötschke, U. W. Pohl, and D. Bimberg, *phys. stat. sol. (b)* **243**, 3937 (2006).
- [83] M. Ediger, G. Bester, B. D. Gerardot, A. Badolato, P. M. Petroff, K. Karrai, A. Zunger, and R. J. Warburton, *Phys. Rev. Lett.* **98**, 036808 (2007).
- [84] R. Heitz, F. Guffarth, K. Pötschke, A. Schliwa, and D. Bimberg, *Phys. Rev. B* **71**, 045325 (2005).
- [85] A. Schliwa, M. Winkelkemper, and D. Bimberg, submitted to *Phys. Rev. B* (2007).
- [86] O. Stier, A. Schliwa, R. Heitz, M. Grundmann, and D. Bimberg, *phys. stat. sol. (b)* **224**, 115 (2001).
- [87] *Scanning Tunneling Microscopy*.
- [88] *Atomic Force Microscopy*.
- [89] *Cross Section STM*.
- [90] F. Guffarth, R. Heitz, A. Schliwa, K. Pötschke, and D. Bimberg, *Physica E* **21**, 326 (2004).
- [91] S. Rodt, A. Schliwa, R. Heitz, V. Türck, O. Stier, R. L. Sellin, M. Strassburg, U. W. Pohl, and D. Bimberg, *phys. stat. sol. (b)* **234**, 354 (2002).
- [92] D. V. Regelman, E. Dekel, D. Gershoni, E. Ehrenfreund, A. J. Williamson, J. Shumway, A. Zunger, W. V. Schoenfeld, and P. M. Petroff, *Phys. Rev. B* **64**, 165301 (2001).
- [93] J. Finley, P. Fry, A. Ashmore, A. Lemaître, A. Tartakovskii, R. Oulton, D. Mowbray, M. Skolnick, M. Hopkinson, P. Buckle, et al., *Phys. Rev. B* **63**, 161305 (2001).
- [94] F. Findeis, M. Baier, E. Beham, A. Zrenner, and G. Abstreiter, *Appl. Phys. Lett.* **78**, 2958 (2001).
- [95] F. Findeis, M. Baier, A. Zrenner, M. Bichler, G. Abstreiter, U. Hohenester, and E. Molinari, *Phys. Rev. B* **63**, 121309(R) (2001).

- [96] M. Baier, F. Findeis, A. Zrenner, M. Bichler, and G. Abstreiter, Phys. Rev. B **64**, 195326 (2001).
- [97] B. Urbaszek, R. J. Warburton, K. Karrai, B. D. Gerardot, P. Petroff, and J. Garcia, Phys. Rev. Lett. **90**, 247403 (2003).
- [98] E. S. Moskalenko, V. Donchev, K. F. Karlsson, P. O. Holtz, B. Monemar, W. V. Schoenfeld, J. M. Garcia, and P. M. Petroff, Phys. Rev. B **68**, 155317 (2003).
- [99] G. Bester and A. Zunger, Phys. Rev. B **68**, 073309 (2003).
- [100] X. Yang, M. J. Jurkovic, J. B. Heroux, and W. I. Wang, Appl. Phys. Lett. **75**, 178 (1999).
- [101] K. Pötschke, L. Müller Kirsch, R. Heitz, R. Sellin, U. Pohl, D. Bimberg, N. Zakharov, and P. Werner, Physica E **21**, 606 (2004).
- [102] U. W. Pohl, K. Pötschke, A. Schliwa, F. Guffarth, D. Bimberg, N. D. Zakharov, P. Werner, M. B. Lifshits, V. A. Shchukin, and D. E. Jesson, Phys. Rev. B **72**, 245332 (pages 7) (2005).
- [103] R. Heitz, T. R. Ramachandran, A. Kalburge, Q. Xie, I. Mukhametzhhanov, P. Chen, and A. Madhukar, Phys. Rev. Lett. **78**, 4071 (1997).
- [104] M.-I. Alonso, M. Ilg, and K. H. Ploog, Phys. Rev. B **50**, 1628 (1994).
- [105] J. Brübach, A. Y. Silov, J. E. M. Haverkort, W. v. d. Vleuten, and J. H. Wolter, Phys. Rev. B **59**, 10315 (1999).
- [106] R. Heitz, O. Stier, I. Mukhametzanow, A. Madhukar, and D. Bimberg, Phys. Rev. B **62**, 11017 (2000).
- [107] I. Mukhametzhhanov, Z. Wei, R. Heitz, and A. Madhukar, Appl. Phys. Lett. **75**, 85 (1999).
- [108] H. Saito, K. Nishi, and S. Sugou, Appl. Phys. Lett. **74**, 1224 (1999).
- [109] R. Heitz, A. Kalburge, Q. Xie, M. Grundmann, P. Chen, A. Hoffmann, A. Madhukar, and D. Bimberg, Phys. Rev. B **57**, 9050 (1998).
- [110] M. Grundmann, N. N. Ledentsov, O. Stier, J. Böhmer, D. Bimberg, V. M. Ustinov, P. S. Ustinov, P. S. Kop'ev, and Z. I. Alferov, Phys. Rev. B **53**, R10509 (1996).
- [111] L. G. Wang, P. Kratzer, N. Moll, and M. Scheffler, Phys. Rev. B **62**, 1897 (2000).
- [112] V. Türck, S. Rodt, O. Stier, R. Heitz, R. Engelhardt, U. Pohl, D. Bimberg, and R. Steingrüber, Phys. Rev. B **61**, 9944 (2000).
- [113] V. Kulakovskii, G. Bacher, R. Weigand, T. Kümmell, A. Forchel, E. Borovitskaya, K. Leonardi, and D. Hommel, Phys. Rev. Lett. **82**, 1780 (1999).
- [114] M. Grundmann and D. Bimberg, Phys. Rev. B **55**, 9740 (1997).
- [115] M. Combescot and M.-A. Dupertuis, European Physical Journal B **50**, 459 (2006).
- [116] S. Fafard, M. Spanner, J. P. McCaffrey, and Z. R. Wasilewski, Appl. Phys. Lett. **76**, 2268 (2000).
- [117] H. Heidemeyer, S. Kiravittaya, C. Müller, and N. Y. Jin Philipp, Appl. Phys. Lett. **80**, 1544 (2002).
- [118] S. Solomon, J. A. Trezza, A. F. Marshall, and J. S. Harris, Phys. Rev. Lett. **76**, 952 (1996).
- [119] I. Mukhametzhhanov, R. Heitz, J. Zeng, P. Chen, and A. Madhukar, Appl. Phys. Lett. **73**, 1841 (1998).
- [120] Q. Xie, A. Madhukar, P. Chen, and N. P. Kobayashi, Phys. Rev. Lett. **75**, 2542 (1995).
- [121] P. Barthold, F. Hohls, N. Maire, K. Pierz, and R. J. Haug, Phys. Rev. Lett. **96**, 246804 (pages 4) (2006).
- [122] G. Kiesslich, P. Samuelsson, A. Wacker, and E. Scholl, Phys. Rev. B **73**, 033312 (pages 4) (2006).
- [123] H. Sprekeler, G. Kiesslich, A. Wacker, and E. Scholl, Phys. Rev. B **69**, 125328 (pages 6) (2004).
- [124] G. Kießlich, A. Wacker, and E. Schöll, Phys. Rev. B **68**, 125320 (2003).
- [125] G. Kießlich, A. Wacker, and E. Schöll, Physica E **12**, 837 (2002).
- [126] K. Hinzer, M. Bayer, J. P. McCaffrey, P. Hawrylak, M. Korkusinski, O. Stern, Z. R. Wasilewski, S. Fafard, and A. Forchel, phys. stat. sol. (b) **224**, 385 (2001).
- [127] H. J. Krenner, M. Sabathil, E. C. Clark, A. Kress, D. Schuh, M. Bichler, G. Abstreiter, and J. J. Finley, Phys. Rev. Lett. **94**, 057402 (pages 4) (2005).
- [128] M. Bayer, O. Stern, A. Kuther, and A. Forchel, Phys. Rev. B **61**, 7273 (2000).
- [129] A. Endoh, Y. Nakata, Y. Sugiyama, M. Takatsu, and N. Yokoyama, Jpn. J. Appl. Phys. **38**, 1085 (1999).
- [130] R. Heitz, I. Mukhametzhhanov, P. Chen, and A. Madhukar, Phys. Rev. B **58**, R10151 (1998).

- [131] S. Bognar, Ph.D. thesis, Technische Universität Berlin (2005).
- [132] P. Jayavel, H. Tanaka, T. Kita, O. Wada, H. Ebe, M. Sugawara, J. Tatebayashi, Y. Arakawa, Yoshiaki Nakata, and T. Akiyama, *Jpn. J. Appl. Phys.* **43**, 1978 (2004).
- [133] Z. M. Wang, Y. I. Mazur, S. Seydmohamadi, G. J. Salamo, and H. Kissel, *Appl. Phys. Lett.* **87**, 213105 (2005).
- [134] S. Sanguinetti, M. Gurioli, E. Grilli, M. Guzzi, and M. Henini, *Appl. Phys. Lett.* **77**, 1982 (2000).
- [135] A. Patanè, A. Levin, A. Polimeni, F. Schindler, P. C. Main, L. Eaves, and M. Henini, *Appl. Phys. Lett.* **77**, 2979 (2000).
- [136] Y. Temko, T. Suzuki, P. Kratzer, and K. Jacobi, *Phys. Rev. B* **68**, 165310 (2003).
- [137] M. Povolotskyi, A. D. Carlo, P. Lugli, S. Birner, and P. Vogl, *IEEE transactions on nanotechnology* **3**, 124 (2004).
- [138] J. B. Xia, *Phys. Rev. B* **43**, 9856 (1990).
- [139] S. S. Li and J. B. Xia, *Phys. Rev. B* **50**, 8602 (1994).
- [140] T. B. Bahder, *Phys. Rev. B* **51**, 10892 (1995).
- [141] R. H. Henderson and E. Towe, *J. Appl. Phys.* **78**, 2447 (1995).
- [142] P. Tomasini, K. Arai, F. Lu, Z. Q. Zhu, T. Sekiguchi, M. Suezawa, T. Yao, M. Y. Shen, T. Goto, T. Yasuda, et al., *J. Appl. Phys.* **83**, 4272 (1998).
- [143] P. Miska, C. Paranthoen, J. Even, N. Bertru, A. L. Corre, and O. Dehaese, *J. Phys.: Condens. Matter* **14**, 12301 (2002).
- [144] C. Cornet, A. Schliwa, J. Even, F. Doré, C. Celebi, A. Létoublon, E. Macé, C. Paranthoën, A. Simon, P. M. Koenraad, et al., *Phys. Rev. B* **74**, 035312 (2006).
- [145] S. Fréchengues, V. Drouot, N. Bertru, B. Lambert, S. Loualiche, and A. L. Corre, *J. Cryst. Growth.* **201-202**, 1180 (1999).
- [146] L. D. Caro and L. Tapfer, *Phys. Rev. B* **48**, 2298 (1993).
- [147] U. Ekenberg, *Phys. Rev. B* **40**, 7714 (1989).
- [148] J. Luttinger, *Phys. Rev.* **102**, 1030 (1956).